

**REPORT DOCUMENTATION PAGE**Form Approved  
OMB No. 0704-0188

Public reporting burden for this collection of information is estimated to average 1 hour per response, including the time for reviewing instructions, searching data sources, gathering and maintaining the data needed, and completing and reviewing the collection of information. Send comments regarding this burden estimate or any other aspect of this collection of information, including suggestions for reducing this burden to Washington Headquarters Service, Directorate for Information Operations and Reports, 1215 Jefferson Davis Highway, Suite 1204, Arlington, VA 22202-4302, and to the Office of Management and Budget, Paperwork Reduction Project (0704-0188) Washington, DC 20503.

**PLEASE DO NOT RETURN YOUR FORM TO THE ABOVE ADDRESS.**

<b>1. REPORT DATE (DD-MM-YYYY)</b> 01-09-1997		<b>2. REPORT DATE</b> Final Technical		<b>3. DATES COVERED (From - To)</b> 15-05-1997 - 14-04-2001	
<b>4. TITLE AND SUBTITLE</b>  "Design and Control of a Nonlinearly Compliant Robotic Finger"  "A Compliant Robot Hand--ASSERT"				<b>5a. CONTRACT NUMBER</b> N00014-97-1-0698	
				<b>5b. GRANT NUMBER</b>	
				<b>5c. PROGRAM ELEMENT NUMBER</b>	
				<b>5d. PROJECT NUMBER</b>	
<b>6. AUTHOR(S)</b>  Salisbury, Kenneth, Jr.				<b>5e. TASK NUMBER</b>	
				<b>5f. WORK UNIT NUMBER</b>	
<b>7. PERFORMING ORGANIZATION NAME(S) AND ADDRESS(ES)</b> Massachusetts Institute of Technology 77 Massachusetts Avenue Cambridge, MA 02139				<b>8. PERFORMING ORGANIZATION REPORT NUMBER</b>	
<b>9. SPONSORING/MONITORING AGENCY NAME(S) AND ADDRESS(ES)</b> Office of Naval Research Program Officer: Theresa McMullen ONR 342 PS 800 North Quincy Street Arlington, MA 22217-5660				<b>10. SPONSOR/MONITOR'S ACRONYM(S)</b>	
				<b>11. SPONSORING/MONITORING AGENCY REPORT NUMBER</b>	
<b>12. DISTRIBUTION AVAILABILITY STATEMENT</b> Approved For Public Release					
<b>13. SUPPLEMENTARY NOTES</b>					
<b>14. ABSTRACT</b> This report describes an inexpensive, modular robot finger utilizing exponentially stiffening springs between the actuators and joints. Controlling the deflection of these springs is equivalent to controlling force, since the deflection is directly related to the applied force through the spring's force-deflection curve. Therefore, the use of compliance in the joints transforms the problem of force control into one of position control, thereby simplifying force control algorithms, improving performance and allowing the use of small, cheap, gear-reduced actuators. The exponential nature of the compliance allows a constant percentage resolution of forces that can be exerted and sensed. This constant percentage resolution leads to an extremely large dynamic range and excellent contact sensing ability. These traits are also present in humans, and have been identified as essential to the dexterity of human fingers. The fingers can be used in combination to form a hand capable of grasping and grasp gaits, or individually for palpation and perception.					
<b>15. SUBJECT TERMS</b>  Robotic Mechanisms, Hand and Fingers, Manipulation, Grasping, Dexterity.					
<b>16. SECURITY CLASSIFICATION OF:</b>			<b>17. LIMITATION OF ABSTRACT</b>  Same As Report	<b>18. NUMBER OF PAGES</b>  110	<b>19a. NAME OF RESPONSIBLE PERSON</b> Dr. J. Kenneth Salisbury Jr.
a. REPORT	b. ABSTRACT	c. THIS PAGE			<b>19b. TELEPHONE NUMBER (Include area code)</b> 650-723-3994

20030110 100

# **Design and Control of a Nonlinearly Compliant Robotic Finger**

by  
Vinay Kishore Shah

B.S., Mechanical Engineering  
University of California at Berkeley, 1994

Submitted to the Department of Mechanical Engineering  
in Partial Fulfillment of the Requirements for the  
Degree of

Master of Science in Mechanical Engineering

at the  
Massachusetts Institute of Technology

September 1997

©1997 Massachusetts Institute of Technology  
All rights reserved

Signature of Author: \_\_\_\_\_  
Department of Mechanical Engineering  
August 8, 1997

Certified by: \_\_\_\_\_  
Dr. J. Kenneth Salisbury Jr.  
Principal Research Scientist  
Thesis Supervisor

Accepted by: \_\_\_\_\_  
A. A. Sonin  
Professor of Mechanical Engineering  
Chairman, Committee for Graduate Students

# **Design and Control of a Nonlinearly Compliant Robotic Finger**

by

Vinay Kishore Shah

Submitted to the Department of Mechanical Engineering  
on August 8, 1997 in Partial Fulfillment of the  
Requirements for the Degree of Master of Science in  
Mechanical Engineering

## **ABSTRACT**

In this work an inexpensive, modular robot finger was designed and developed with exponentially stiffening springs between the actuators and joints. Controlling the deflection of these springs is equivalent to controlling force, since the deflection is directly related to the applied force through the spring's force-deflection curve. Therefore, the use of compliance in the joints transforms the problem of force control into one of position control, thereby simplifying force control algorithms, improving performance, and allowing the use of small, cheap, gear-reduced actuators. Furthermore, the exponential nature of the compliance allows a constant percentage resolution of forces that can be exerted and sensed. This constant percentage resolution leads to an extremely large dynamic range and excellent contact sensing ability. These traits are also present in humans, and have been identified as essential to the dexterity of human fingers.

The finger was designed with three degrees-of-freedom and kinematics similar to that of human fingers. The fingers can be used in combination to form a hand capable of grasping and grasp gait experiments, or individually for palpation and perception experiments. The modularity of the fingers permits variable hand configurations and allows manipulation of objects with a wide range of size and shape. Furthermore, modularity helps to reduce the cost of a complete hand, since fewer unique parts are required.

A control structure for precise application of torque through these exponential springs was devised, and the performance enhancements were quantified using a single-axis test stand that isolated one actuator and compliant element. The control algorithm consists of a high gain, high bandwidth inner motor position control loop, and a lower bandwidth outer torque loop. The torque resolution using this system remained constant at 5% regardless of the magnitude of the forces, and was exactly equal to the resolution of the spring deflection sensor. This resolution leads to a dynamic range of over 1000, a factor of 30 increase over the gear-reduced motor alone. However, the use of compliance limits the bandwidth of the actuator to about 10Hz. It is expected that this reduction in bandwidth will not have a significant effect in finger and hand applications, since grasping and grasp gait tasks require low bandwidth movements.

Three of these torque control blocks were combined, along with additional layers for simple path planning and desired joint torque calculation, to form the basis for the finger control algorithm. However, a high performance fingertip position and force control algorithm was not realized. But, it was shown that the basic torque control structure used successfully on the single-axis system can also be used in the multiple-axis case, despite the cross-axis coupling and changing load torque and inertia. Additional research is required to achieve fingertip force control performance equivalent to that achieved in controlling an isolated torque on the single-axis test stand.

Thesis Supervisor: Dr. J. Kenneth Salisbury Jr.  
Title: Principal Research Scientist

## Acknowledgements

This work would not have been possible without the support and guidance from my advisor, Dr. Ken Salisbury. Ken has been very helpful with his vast experience with robot hands and his unique insights. It has been a genuine pleasure working with him.

I would also like to thank the rest of Ken's research group, especially Akhil Madhani, Craig Latimer, Gunter Niemeyer, and Brian Anthony. They were always around and willing to help me with design and control issues, and to give me some fresh ideas and viewpoints.

Thanks also to all my friends at MIT who have made my stay here enjoyable and filled with so many fond memories. My two best friends, Loreli Cadapan and Craig Latimer, have been there for me through thick and thin. Loreli has been supportive and helpful from the beginning, and even helped put this report together. Craig was always willing to fly over the handlebars with me at Lynn Woods when the lab was just too unbearable.

And last but not least, I would like to thank my family who have always given me the most unconditional love and support anyone could ask for. My parents and sister have always believed in me. Their encouragement helped me get through the times when I thought I would never finish.

Finally, I would like to gratefully acknowledge the financial support of the Office of Naval Research, University Research Initiative Program, Grant N00014-92-J-1814, without which this project would never have gotten off the ground.

There are many others who are not named here but whose contributions to my thesis and my delightful experience at MIT will always be remembered.

# Contents

<i>List of Figures</i>	6
<b>1 INTRODUCTION</b>	7
<b>2 MOTIVATION FOR A NEW HAND</b>	8
2.1 Overview of Existing Hands	9
2.2 Limitations of Existing Hands	10
2.3 Performance of Human Hands	11
2.4 Goals of New Robot Finger	12
<b>3 METHOD OF PERFORMANCE ENHANCEMENT</b>	13
3.1 Traditional Stiff Transmission Design	14
3.2 Enhanced Performance Through Compliance	15
3.2.1 Benefits of Exponentially Stiffening Springs	16
3.3 Other Methods of Improving Performance	17
<b>4 COMPLIANT ELEMENT</b>	17
4.1 Mechanical Design	17
4.2 Instrumentation	20
<b>5 SINGLE-AXIS TEST STAND</b>	22
5.1 Mechanical Setup	22
5.2 Controller	24
5.2.1 Loop Stability	26
5.2.2 Filters	26
5.2.3 Selection of Time-Varying Gains	27
5.2.4 Controller Modifications	29
5.3 Performance	31
5.3.1 Trajectory Tracking	31
5.3.2 Performance Measures	35
5.3.3 Bandwidth	36
<b>6 FINGER DESIGN</b>	38
6.1 Kinematics	39
6.2 Link Lengths	40
6.2.1 Jacobian	40
6.2.2 Results of Calculations	41
6.2.3 Actual Link Lengths	41
6.3 Drive Assembly	42
6.4 Cable-Pulley System	44
6.5 Finger Links	45
6.6 Actuation	46
6.7 Instrumentation	47
<b>7 FINGER CONTROL AND PERFORMANCE</b>	47

7.1 Three-Axis Controller	47
7.2 Controller Performance	49
8 NEW FINGER DESIGN	53
8.1 The Drive Assembly	55
8.2 Cable/Pulley System	57
8.2.1 Cable rubbing	57
8.2.2 Cable Tensioning	58
8.3 Finger Links	59
8.4 Simplified Machining	60
9 SUMMARY	61
References	63
Appendix A: New Finger Components	66

## List of Figures

Figure 1: Salisbury Hand	9
Figure 2: Utah/MIT Dexterous Hand	10
Figure 3: Torque vs. Deflection Curve for the Compliant Element	19
Figure 4: Potentiometer Amplifier Circuit	20
Figure 5: Amplified Pot Output vs. Input Shaft Position	21
Figure 6: Single-Axis Test Stand	23
Figure 7: One-DOF, Fixed-End Model	23
Figure 8: Two-Inertia Model	24
Figure 9: Controller Schematic Diagram	25
Figure 10: 5 mNm Step Response w/o Integrator Windup Protection	30
Figure 11: 40 mNm Step Response w/o Integrator Windup Protection	30
Figure 12: 40 mNm Step Response With Integrator Windup Prevention	31
Figure 13: 150 mNm Step Response With Integrator Windup Prevention	31
Figure 14: Step Tracking Performance	32
Figure 15: Sinusoidal Tracking Performance	33
Figure 16: Rejection of Continuous Random Disturbances by Torque Controller	34
Figure 17: Rejection of Large Spike Disturbances by Torque Controller	35
Figure 18: Frequency Response of the Overall Torque Control System	37
Figure 19: Frequency Response of the Inner Loop PD Position Controller	38
Figure 20: Original Finger Design	39
Figure 21: Chosen Finger Kinematics	39
Figure 22: Locus of Isotropic Points	41
Figure 23: Drive Assembly	42
Figure 24: Compliant Element 1 Cable Transmission and Tensioning	43
Figure 25: Compliant Element 2 and 3 Cable Termination and Tensioning	44
Figure 26: "Alpha Loop" Around Idler Pulley	45
Figure 27: Link 1, the "knuckle"	45
Figure 28: Link 2 and Link 3, the "digits"	46
Figure 29: Schematic of Three-Axis Control System	48
Figure 30: Joint Torque Step Tracking w/Fixed Fingertip	51
Figure 31: Joint Torque Sinusoid Tracking w/Fixed Fingertip	52
Figure 32: Gravitational Torque Tracking While Finger is Manually Moved	53
Figure 33: New Finger Design	54
Figure 34: Front and Side Views of Lower Actuator in New Design	56
Figure 35: Cable Routing Over Double Idler Pulleys	57
Figure 36: Cable Loses Contact With First Pulley	58
Figure 37: Cable Tensioning in the New Finger Design	59
Figure 38: Old and New Versions of Link 2	60

# 1 INTRODUCTION

Since the inception of the field of robotics over fifty years ago, scientists and engineers have raced to build robots with ever-increasing capabilities. These robots evolved from simple devices designed for specific tasks, to more complex mechanisms with broad applicability. However, robotic end-effectors have not experienced the same level of development. On the contrary, modern industrial end-effectors are still highly specialized devices designed for very specific tasks, despite a significant effort in the robotics community to develop more general end-effectors, such as multi-fingered hands. Advances at the research level have not been adopted by industry, partially because of the enormous cost and complexity of the mechanisms and control strategies that were developed. These issues were addressed in this work by designing, constructing, and controlling a low cost, high performance robotic finger. This modular finger can be used as a baseline for the development of inexpensive, hand-like end-effectors capable of executing a wide range of dexterous manipulation tasks.

The earliest robots were master-slave mechanisms, where a master manipulator was manually operated by the user, while the mechanically coupled slave unit mimics every movement of the master. These robots were designed for very specific applications, since the requirement of mechanical linkages to connect the master and slave prevents generic system design. However, the mechanically linked slaves eventually gave way to independently actuated mechanisms and the master teleoperators were replaced by computer control, which opened the door for the development of multi-purpose robots. Today, many different six degree-of-freedom (DOF) robot arms exist, such as the Stanford Arm, Schilling Arm, and Whole Arm Manipulator (WAM). Although there are many fundamental differences among these robots, they are all capable of exerting large forces and moving and positioning in a precise manner within a large workspace, making them suitable for many different purposes.

End-effectors are typically mounted on the end of these multi-purpose manipulators, and are the interface between the arms and the environment. Although today's end-effectors can accomplish complex and delicate tasks such as assembly involving mating parts or integrated circuits, they are usually highly specialized devices and are limited to the particular task for which they were designed for several reasons. First, they lack the dexterity to manipulate a grasped object, so the orientation in which the object is presented to the end-effector must be precisely controlled. Second, the size and shape of graspable objects and the number of possible grasps on these objects are limited, so end-effectors must frequently be changed for different tasks. Finally, they lack the ability to accurately exert both large forces and small forces, which further limits their applicability.

In response to these issues, a significant effort by the robotics research community for many years has focused on the development and control of multi-fingered, articulated hands to be used as general purpose, dexterous end-effectors. Results of this research include the Salisbury Hand and the Utah/MIT Hand,



which are force-controllable, three- and four-fingered hands capable of extremely dexterous manipulation of a wide range of objects. However, the vast potential demonstrated by these devices has not been realized because of the enormous cost and complexity of the mechanisms, as well as the algorithms and computational resources required to control them.

In this work, an inexpensive, high performance robotic finger was developed to be the basis for a new dexterous hand. The finger uses exponentially stiffening springs between the motors and finger joints to achieve intrinsic mechanical compliance. This compliance allows the use of inexpensive actuators and sensors and a relatively simple control strategy to achieve performance characteristics identified as essential for dexterous manipulation, such as force controllability, dynamic range, and accurate contact sensing. Although a robotic hand composed of these fingers is by no means ready for industrial use, it is hoped that further work exploring its full capabilities will trigger a new wave of hand research, which, in turn, will eventually lead to the success of dexterous robot hands outside of the laboratory.

The remaining chapters of this paper will discuss in more detail existing dexterous end-effectors and the motivation for designing a new one. It will then describe how the use of intrinsic mechanical compliance can help to improve dexterity and performance, while decreasing costs and simplifying the mechanics and required control strategies. Chapter 4 will then describe the design of the compliant elements used to impart intrinsic flexibility to the mechanism. Next, a strategy for precisely controlling the torque output of this compliant element is presented, and the performance of this controller is quantified. The following two chapters discuss the design of a three-DOF finger that uses these compliant elements, and the implementation and evaluation of a torque controller for the finger joints. An improved finger design is then presented in Chapter 8 before finally summarizing the work presented here.

## **2 MOTIVATION FOR A NEW HAND**

Researchers and engineers worldwide have developed dozens of mechanical hands, ranging from prosthetic devices to multi-fingered robot hands for dexterous manipulation. The most famous of these are the Salisbury Hand and the Utah/MIT Hand. Despite their enormous potential, none of these mechanisms have achieved widespread success in industrial settings, nor have they become commonplace in the research community. Among the reasons for this are their costs of production and operation and their complexity of control. Furthermore, the capabilities of existing robot hands pale in comparison to human hands. Current mechanical hands cannot robustly perform many basic tasks that humans can do, such as grasp gaits, which are large scale re-orientations of objects while maintaining a stable grasp. A need exists for a robotic hand that can begin to approach the performance of human hands, while maintaining low cost, simplicity of control, and ease of operation. The modular finger designed in this work is meant to be the basis for a new hand that fulfills this need.

## **2.1 Overview of Existing Hands**

The idea of mechanical hands is certainly not a new one; it has been in existence for hundreds of years. In fact, one of the earliest devices referenced in the literature was built in 1509 for a knight who had lost his hand in battle [Childress, 1972]. This hand and most of the other hand mechanisms developed before the 1960's were intended for prosthetic applications [Murray, 1994], evolving from simple, cosmetic attachments to body-controlled mechanisms and, more recently, even externally-powered, myoelectrically controlled devices [Jacobsen, 1982].

However, in the last 30 years, the desire to manipulate objects in remote or hazardous environments and to automate assembly or manufacturing processes has driven the development of computer-controlled, dexterous, multifingered hands. These devices were intended to be teleoperated "slaves" or dexterous end-effectors for other robots. Some of the first of these mechanisms were designed by Skinner [Skinner, 1975], Crossley [Crossley, 1977], Hanafusa and Asada [Hanafusa, 1982], and Okada [Okada, 1982]. Most of these hands were limited in functionality to simple grasping maneuvers, although the Okada hand, a three-fingered, cable-driven device, was able to perform slightly more complex tasks such as screwing a nut onto a bolt.

The most capable and most famous robotic hands were the Salisbury Hand [Salisbury, 1984], shown in Figure 1, and the Utah/MIT Dexterous Hand [Jacobsen, 1984], shown in Figure 2. The Salisbury Hand consisted of three cable-driven fingers, each with three degrees-of-freedom (DOF) actuated by electric DC motors. The fingers were placed in a human-like configuration such that one finger (the "thumb") opposed the other two, which were placed adjacent to each other. The Utah/MIT Hand was even more anthropomorphically inspired, and consisted of three fingers and a thumb with 4 DOF each. The fingers and thumb closely resemble their human counterparts in appearance, kinematics, range of motion, and location on the palm, which also was designed to look similar to a human palm. Each finger joint was driven by cable tendons, as with the Salisbury Hand, but the Utah/MIT Hand was actuated by pneumatic pistons. These hands were able to grasp a huge range of objects and perform many complex manipulation tasks.

**Figure 1: Salisbury Hand**

**Figure 2: Utah/MIT Dexterous Hand**

The introduction of these two hands triggered a flurry of research activity in the area of dexterous manipulation. Some of the products of this research are newer robotic hands like the five-fingered Anthrobot-2 [Ali, 1993] and the Four-Fingered JPL Hand [Jau, 1992]. Both of these new hands are extremely human-like in form. In fact, the primary design goal for the Anthrobot-2 was to create a hand that is identical to human hands in number of fingers, number of joints per finger, placement and motion of the thumb, proportions of the link lengths, and shape of the palm.

The Four-Fingered JPL Hand goes a step further by including an anthropomorphic wrist and part of a forearm. Interestingly, the JPL Hand has five active compliance adjusters for independent modulation of the stiffness of each of the four complete fingers and the wrist. An exoskeletal glove controller is used for teleoperation of the hand.

## ***2.2 Limitations of Existing Hands***

Despite their tremendous dexterity and versatility compared to most industrial robotic end-effectors, robot hands have not been widely used for industrial purposes. Instead, highly specialized devices are designed for individual applications. These devices lack the adaptability to meet the needs of changing environments and task requirements, so new robots or end-effectors are required whenever manufacturing lines change. Nevertheless, they are the standard of industrial automation, because current robot hands require more complex control strategies, are extremely expensive, and are more difficult to operate.

Hand programmers have been able to perform marvelous tasks with current robot hands, such as executing basic grasp gaits [Fearing, 1986], but only with monumental control effort. Not only are the path and grasp planning algorithms complex, but also the underlying structure for control of the fingertip contact forces.

Recognizing that compliance can improve force control performance, some researchers even attempt to mimic variable compliance with software algorithms [Hogan, 1985]. However, this active approach to force and compliance control is limited in bandwidth and resolution, and requires extensive computational resources.

Another problem is that current hand mechanisms are just too expensive to be used in an industrial setting. The Salisbury and Utah/MIT Hands ranged in price from around \$40,000 to \$100,000, although these numbers would probably be significantly lower if demand were enough to justify larger production volumes. In contrast, most industrial end-effectors can be produced for just a fraction of that price because of their simplicity of design, fewer actuated degrees-of-freedom, and reduced sensor and actuator requirements.

An additional reason why these hands have not gained widespread popularity is that they are not particularly convenient to use. The Utah/MIT Hand requires a small room to house all the air compressors, pressure regulators, and other components that drive the pneumatic pistons. And, the Salisbury Hand has a separate, 12 pound, drive package consisting of the motors, gear reductions, and cable tension sensors. Although much more compact than the Utah/MIT Hand's compressors, this drive package represents a significant load when mounted to the end of an arm, limiting the arm's capability to perform useful work.

### **2.3 Performance of Human Hands**

Human hands are unequalled by their mechanical counterparts in dexterity, sensitivity, and adaptability. Humans can achieve stable grasps on a huge range of objects varying in size, shape, weight, surface texture, etc. The grasps can be extremely stiff or extremely flexible, and can have large contact forces or small contact forces. The contacts can be with the fingertips, the walls of the finger, the palm, or any combination of the three. Moreover, humans can reorient the grasped object while maintaining a stable grasp, a process known as finger or grasp gaiting. The performance characteristics of human hands that allow these great capabilities has been a subject of research for many years. Some results of this research point to characteristics such as an extreme range of forces that can be exerted and sensed, excellent resolution of forces within that range, the ability to accurately detect contact with the grasped object, and the capacity to modulate the grasp and finger stiffness [Leveroni, 1997].

It appears that one of the key traits that give human hands their incredible dexterity is dynamic range, defined as the ratio of the largest to smallest force that can be exerted or sensed. The human fingertip can exert both extremely large forces and minutely small ones, giving a dynamic range on the order of 10000:1 [Srinivasan, 1993]. In contrast, very good multi-DOF robots are usually limited to a dynamic range of only about 100:1 [Morrell, 1995].

In addition to large dynamic range, the percentage resolution of forces that can be exerted and sensed remains nearly constant throughout that entire range. This resolution is the smallest percentage change in force that can be distinguished (Just Noticeable Difference, JND) or exerted (Just Controllable Difference, JCD) by the human fingertip. By applying varying contact forces to the fingerpad of human subjects, researchers have determined that humans can perceive a percentage change in force that is independent of the magnitude of the force. This JND has been reported to be between 7% [Pang, 1991; Tan, 1992] and 10% [Clark, 1986; Jones, 1989]. Similar experiments have shown that humans can exert a constant JCD (with tactile feedback only) of between 11% and 15%, regardless of the size of the forces [Srinivasan, 1993]. Interestingly, Srinivasan noticed that when a visual display of the contact force and force error was provided, subjects could effect a constant absolute change in force, giving a percentage resolution that decreased with force magnitude.

A third important characteristic of human fingers that leads to dexterity is the ability to detect contact. In a very basic sense, manipulation can be thought of as a pattern of intermittent contact between the fingers and the manipulated object, so fingers that can accurately detect when and where these contacts occur are more effective at manipulation. Humans are exceptional at detecting these contacts because of their vast number of tactile receptors on the fingertip.

A fourth trait that human fingers have that aids in dexterous manipulation is the ability to modulate finger and grasp stiffness due to the variable compliance intrinsic to finger joints. Through co-activation of antagonistic muscles within a finger, humans can vary the stiffness of the finger itself, making it rigid or flexible without even making contact with the environment. Similarly, co-activation between fingers allows humans to modulate the stiffness of a grasp when multiple fingers are in contact with the same object. Some scientists believe that this ability to modulate stiffness by co-activation plays an important role in dexterous manipulation [Hogan, 1988].

## ***2.4 Goals of New Robot Finger***

The goals of this work were to design a modular robot finger that is intrinsically force controllable, has a large dynamic range, has a constant percentage force resolution, and is inexpensive and compact, and to devise a strategy for precise control of fingertip forces. Unlike many previous robot fingers and hands, this finger is not required to be aesthetically human-like. Instead, the goal is to mimic the performance and dexterity of human fingers to create a more capable robot.

These modular fingers can be used as the basis for a multi-fingered hand to be used for grasping and grasp gait experiments. Modularity allows the number and location of the fingers to be reconfigured for particular object sizes and shapes, yielding a huge range of objects that can be grasped and manipulated. Modularity also helps to minimize cost of a complete hand, since multiple finger copies means fewer unique parts and

higher production volumes. Furthermore, the finger can be used singly for palpation and perception experiments on the human haptic system.

Force controllability, dynamic range, and force resolution were achieved by adding mechanical compliance to each joint of the finger in the form of exponentially stiffening springs. This flexibility, similar to the natural compliance found in human finger joints, improves force control performance because position control algorithms can be used to control force. The exponential nature of the compliance provides large dynamic range and constant percentage resolution of exerted and sensed forces. A more detailed explanation of performance benefits of exponential compliance is given in Chapter 3.2.

In addition, these springs help to reduce the cost of the finger by allowing the use of small, off-the-shelf, gear-reduced motors to actuate the joints without compromising force control performance. The small, gear-reduced motors can be used because the springs return to the actuator many qualities that are initially lost when gearheads are introduced, as described in Chapter 3.2. Furthermore, the spring also functions as a torque sensor when equipped with a potentiometer or optical encoder to measure its deflection, so additional force sensing devices are not required.

The use of these small motors and integrated torque sensors also helps to make possible small finger linkages, drive mechanisms, and actuator packages. This yields a simple and compact device that can more easily be appended to an arm without overloading the supporting robot.

Finally, antagonistic actuators were considered, but *not* incorporated in the final design, although they are believed to be important in human dexterity. The use of antagonistic actuators would allow modulation of finger stiffness, but it also doubles the number of required actuators and sensors, increases the complexity of the mechanical and control systems, and reduces the compactness of the device. However, even without antagonistic actuators, modulation of grasp stiffness by co-activation *between* fingers is still possible, and is the basis for the planned improvements in the ability to grasp and manipulate objects. Should it be deemed necessary, additional actuators can be added in the future by slightly modifying the drive mechanism.

### 3 METHOD OF PERFORMANCE ENHANCEMENT

Robotic manipulators have traditionally been designed with transmissions that are as stiff as possible to maximize bandwidth. These systems are excellent for position control, but are not well suited for force control due to low dynamic range and sometimes also low force resolution. Recently, researchers have used linearly compliant transmissions to improve dynamic range and force control, at the cost of decreased bandwidth. In this work, an exponentially compliant transmission was developed to further enhance

performance. Although the work presented here focuses on implementing compliance in a robotic finger, the basic design and control methodology can be applied to create other types of dexterous manipulators.

### **3.1 Traditional Stiff Transmission Design**

Traditionally, engineers and designers have attempted to maximize the performance of their systems by making the transmission between actuator and load as stiff as possible [Townsend, 1988; Eppinger, 1989; Readman, 1994]. This type of mechanism is excellent for fine position control and rapid trajectory tracking since stiffness accommodates fast, high bandwidth controllers. Furthermore, systems with stiff transmissions can even tolerate high controller gains when the sensors are located at the load, without the usual instability problems associated with non-collocated control [Canon, 1984]. Many high performance robots have been built using this philosophy, including the WAM [Salisbury, 1989] and the PHANTOM™ [Massie, 1994].

However, there exist several drawbacks to the use of stiff transmissions for force control. First, in direct-drive systems, the dynamic range is usually restricted to around 100:1 due to limitations of electric motors [Morrell, 1995]. Therefore, motors that can accurately exert small forces cannot provide large forces that are necessary for stable grasping, while larger motors that can exert large forces cannot accurately provide the small forces that are necessary for fine manipulation.

Second, stiff transmission designs introduce performance and reliability issues when gear reductions are used. Motors with gearheads are commonly required when cost and size are design factors, since small, cheap, geared motors can produce the same peak torque as a large motor at a fraction of the price. Furthermore, gearheads are often required to support heavy loads even when large motors are used, because many electric can only produce high power at high speed [Hunter, 1991]. These gearheads add friction, torque ripple, and backlash to the system, and can easily be damaged or even cause damage to objects in the workspace. Friction lowers the dynamic range even further, torque ripple adds errors to the output torque, and the backlash produces uncertainty in the endpoint position and also induces limit cycling in non-collocated systems. Damage to the gearhead often results from shock loads caused by collisions with the environment, because the high reflected inertia ( $N^2$  increase in reflected inertia for an  $N:1$  gearhead) produces enormous forces on the gear teeth. Sometimes these collisions can even result in damage to the environment, due to the high backdrive friction and reflected inertia of geartrains [Pratt, 1995].

Finally, force control of a stiff mechanism with gear-reduced actuators usually requires complex force control strategies and high data rates between the computer and the motors and sensors. Some control methods even attempt to mimic variable mechanical compliance through active impedance control [Hogan, 1985], but only at the cost of a very large control effort.

### 3.2 Enhanced Performance Through Compliance

Improving dynamic range and force control performance by adding mechanical flexibility to a mechanism is a relatively new technique in robot design and control. However, aerospace and structural engineers have developed control strategies for flexible systems, such as those found on satellites and other space structures for decades [Balas, 1977]. Other researchers have added flexible coverings to end-effectors to stabilize force control during intermittent contact with hard surfaces by creating compliance in the interface between the robot and the environment [Hogan, 1989; Whitney, 1987]. But, until recently, engineers have not intentionally added compliance to the transmission between actuator and robot as a means of *improving* performance.

One key benefit of compliant transmissions is that force control is transformed into the easier problem of position control. Since the output force is directly related to the deflection across the transmission, controlling this deflection is equivalent to controlling the force. Furthermore, position can be accurately controlled through a gearhead, resulting in precise force control and virtually eliminating the harmful effects of gearhead friction and torque ripple.

Also, the compliance in the transmission has a low-pass filter effect on loads applied to the robot by the environment. Therefore, peak forces on the gear teeth due to shock loads on the robot are drastically reduced, lowering the likelihood of damage to the gearhead or the environment. However, this low-pass filter also acts on forces transmitted from the actuator to the robot, so the bandwidth of the system is reduced as well. But, dexterous manipulation tasks do not require high bandwidth movements, since human fingers have a bandwidth of only around 7-20 Hz [Srinivasan, 1994; Brooks, 1990]. Therefore, it is expected that this decrease in bandwidth will not drastically affect the grasping and manipulation performance of the compliant finger developed here.

Other researchers have used both passive and actively controlled springs to improve force control performance of manipulators. Pratt and Williamson [Pratt, 1995] developed a series elastic actuator using passive linear springs between the motor and load, developed a simple, effective, and stable force control architecture, and successfully implemented it in the MIT humanoid robot Cog [Brooks, 1994]. Sugano [Sugano, 1992; Morita, 1995] controlled contact forces on a one-DOF robot finger and arm that incorporated actuator-controlled spring stiffness and damping. Tasch [Tasch, 1996] controlled fingertip position and compliance of a two-DOF finger that also used actively-controlled spring stiffness. The work involving actively controlled springs is most similar to human fingers, since it simulates antagonistic muscles which can modulate joint stiffness independently of joint position or contact force. However, these systems require several additional actuators and increased controller complexity, which is not compatible with many goals of this design.



### 3.2.1 Benefits of Exponentially Stiffening Springs

Our work compliments and extends the work of the above researchers by using passive, exponentially stiffening springs to impart nonlinear compliance to the transmission. Exponentially stiffening compliance was chosen because it produces a constant percentage force resolution for control and sensing over an extremely large dynamic range, a desirable trait that is also found in the human haptic system, in addition to the other benefits of compliance described above.

Applying torque with a DC motor through an exponentially compliant transmission produces a constant percentage torque resolution because of the manner in which torque is produced and measured. Torque is produced by positioning the motor to create a deflection of the exponential spring, and the magnitude of the torque can be computed by measuring this deflection. But, motor positioning and spring deflection measuring are accomplished with fixed-resolution sensors (such as encoders or potentiometers), while the torque per unit deflection increases as the torque level increases due to the stiffening nature of the spring. Therefore, at low torque levels, the spring exhibits low stiffness, so a unit change in spring deflection produces a very small change in output torque, yielding a fine absolute torque resolution. At high torque levels, the spring is stiff, so the same unit change in spring deflection produces a much higher change in torque, yielding a coarse absolute resolution. However, the percent change in torque and percent resolution is exactly the same in both cases, as can be seen in the following derivation that compares resolution with linear springs and exponential springs:

<u>Linear Spring</u>	<u>Exponential Spring</u>
$F = k\theta$	force-deflection relationship of the spring
$F_o = k\theta_o$	$F = Ae^{B\theta}$
	a nominal spring deflection produces a nominal torque
$F_o + \Delta F = k(\theta_o + \Delta\theta)$	$F_o = Ae^{B\theta_o}$
	an additional unit deflection produces a change in force
$\frac{\Delta F}{F_o} = \frac{\Delta\theta}{\theta_o}$	$F_o + \Delta F = Ae^{B(\theta_o + \Delta\theta)}$
	the percentage resolution in force
percentage force resolution is dependent on original deflection	$\frac{\Delta F}{F_o} = e^{B\Delta\theta} - 1$
	percentage force resolution is independent of original deflection and is constant for a given $\Delta\theta$

This constant percentage resolution is desirable because it provides adequate force resolution for different types of tasks over an extremely large dynamic range. Extremely fine resolution at low forces aids in performing delicate manipulation tasks, which requires small, precise forces. Lower resolution at high forces is sufficient for coarse manipulation tasks, such as lifting rugged objects. In contrast, a linearly compliant system that provides fine small-force resolution could not achieve a large dynamic range (without huge spring deflections), and a system that can exert large forces could not give adequate resolution at low forces.

### **3.3 Other Methods of Improving Performance**

Another method of increasing dynamic range and force control performance is the micro-macro approach. In this technique, a large (macro) motor provides the main component of output torque, while a much smaller (micro) motor superimposes an additional component of torque. In this system, the large motor is responsible for coarse torque control, while the small motor handles fine control.

A micro-macro actuator system can be used to achieve precise force control and large dynamic range, without the bandwidth limitations present in flexible systems or the backlash, friction, and reflected inertia found in gear-reduced systems [Sharon, 1993]. Morrell [Morrell, 1995] constructed a micro-macro actuator that achieved a dynamic range of about 800 and a bandwidth of nearly 60 Hz.

However, this type of system doubles the required number of actuators, requires larger motors, and increases the complexity of the mechanical system and control algorithms. For these reasons, this method is not compatible with the goal of developing an inexpensive, compact, and easily controllable dexterous end-effector.

## **4 COMPLIANT ELEMENT**

Custom designed compliant elements were inserted between the motor output shafts and finger joints to provide intrinsic mechanical flexibility to the joints and to function as a joint torque sensor. Each compliant element is a compact, self-contained, instrumented package containing an exponentially stiffening, torsional spring, a threaded capstan for wrapping the drive cables that actuate the joints, and a potentiometer to measure the angular deflection of the spring. The applied torque can be computed from the deflection measurement using the torque-deflection relationship of the spring, which was empirically determined.

### **4.1 Mechanical Design**

The compliant element is a clutch-like mechanism consisting of two parallel aluminum disks with alternating radial walls extending from each disk. The front disk includes a clamping mechanism with which it is rigidly attached to the drive shaft. The back disk includes a threaded capstan for routing cables

to the joints, and rotates about the shaft on a ball bearing. The radial walls create pie-shaped pockets on each disk, which are filled with 3/16" diameter rubber balls, through which torque is transmitted from one disk to the other. However, as the balls are compressed, they exert axial reaction forces that tend to push the two plates apart, so it is important to use a retaining ring behind the back plate to hold it in position. This design is cheap and extremely reliable, since there is only one moving part, only two parts require machining, and all components are made of durable and inexpensive aluminum and rubber.

The compliant element functions as a non-linear, exponentially stiffening spring and torque sensor. Any relative motion between the two disks causes the balls to be squeezed between the radial walls, creating the elasticity. Initially, the contact area between the walls and balls is extremely small (approaching point contact), so the stress is high for even small contact forces, yielding a low effective stiffness. As the contact forces increase, the ball deforms further, causing the contact area to increase. Because of this increase in contact area, the stress on the ball ( $Stress = \frac{Force}{Area}$ ) doesn't increase in proportion to the contact forces, thereby increasing the effective stiffness of the ball. As the ball continues to deform, it eventually fills the pocket completely. Any further rotation of the disks compresses the ball into itself and increases its bulk modulus, causing the stiffness to increase even faster, yielding the highly nonlinear stiffening characteristic.

The actual spring torque vs. deflection curve was determined by locking one of the disks in place and attaching a 6" aluminum rod to the other disk. Weights were incrementally hung from the aluminum rod and the resulting deflection was measured with an HP HEDM-5500-J04 (1000 LPR) optical encoder. Figure 3 shows a graph of this data and the best-fitting exponential curve. The relationship and its derivative, which is the spring stiffness, are explicitly expressed in Equation 1.

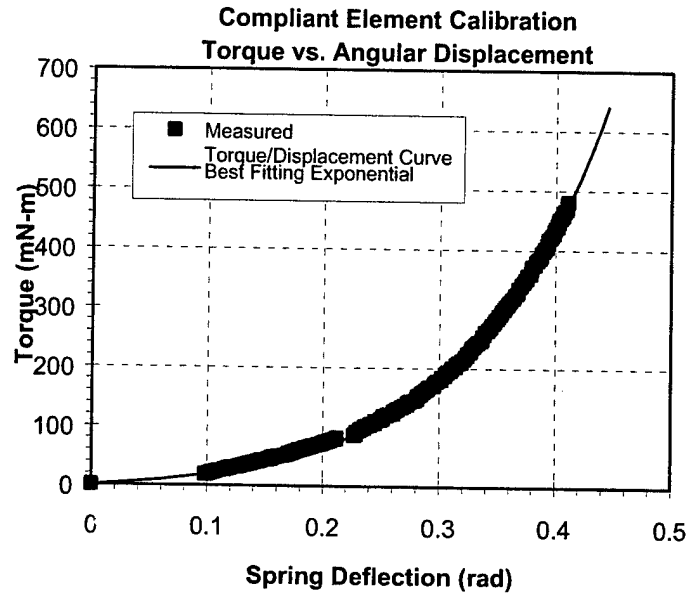


**Figure 3: Torque vs. Deflection Curve for the Compliant Element**

$$\tau = A(e^{B\theta} - 1)$$

$$k = \frac{\partial \tau}{\partial \theta} = AB e^{B\theta}, \text{ where } A = 14.0 \text{ and } B = 8.6$$

**Equation 1: Spring Torque and Stiffness as a Function of Deflection**

The six balls are made of acrylonitrile butadiene, a synthetic rubber also called Buna-N, NBR, or nitrile. This material was chosen for its excellent rebound characteristics, low compression set, and low friction. The composition, number or shape of these elastomers could easily be changed to tune the spring curve to any desired shape.

The pie-shaped pockets between the disks were designed so that the balls would be slightly preloaded in the neutral position (about .006" of compression). Because this preload effectively decreases the small-torque resolution, the amount of preload was made as small as practical to ensure zero backlash. Preload decreases resolution by shifting the torque-displacement relationship, which moves the origin to a steeper point on the curve.

## 4.2 Instrumentation

A Midori America Corporation model CP2U-TX magneto-resistive, panel-mount style, potentiometer was used to measure the angular deflection of the spring. This potentiometer functions by passing a magnet over a material whose resistance changes when exposed to a magnetic field. The non-contact nature of the potentiometer, combined with its bearing-supported input shaft, provides an extremely smooth, differentiable output signal. This output signal is linear with angular position over a  $\pm 45^\circ$  range of motion, although the mechanical rotation is unlimited.

The output signal from the pot is amplified to maximize the signal to noise ratio and resolution. The raw signal varies between 1.5V and 3.5V; it is  $\frac{1}{2}$  of the +5V supply at the pot's neutral position, and varies linearly throughout the electrical range of motion by about  $\pm 20\%$  of the supply voltage. However, this signal is susceptible to noise since it has a small voltage range and does not use the full input range of the A/D board (-5 to 5V or 0 to 10V). Therefore, the circuit shown in Figure 4 was used to shift the neutral position voltage to 0V and amplify the signal 8X, so that about  $\pm 40^\circ$  of mechanical motion uses the entire  $\pm 5V$  range of the board. The output of the circuit vs. potentiometer shaft position is shown in Figure 5, and the slope of the curve is .148 rad/volt. The  $3\sigma$  uncertainty in the pot measurements was computed to be  $\pm 0.25^\circ$  from the observed noise and the deviation from the straight line fit.

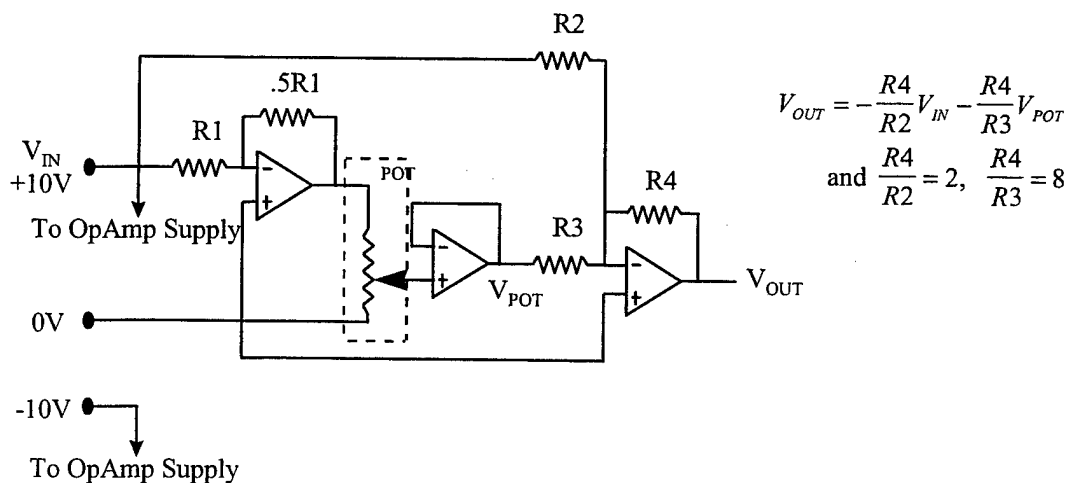
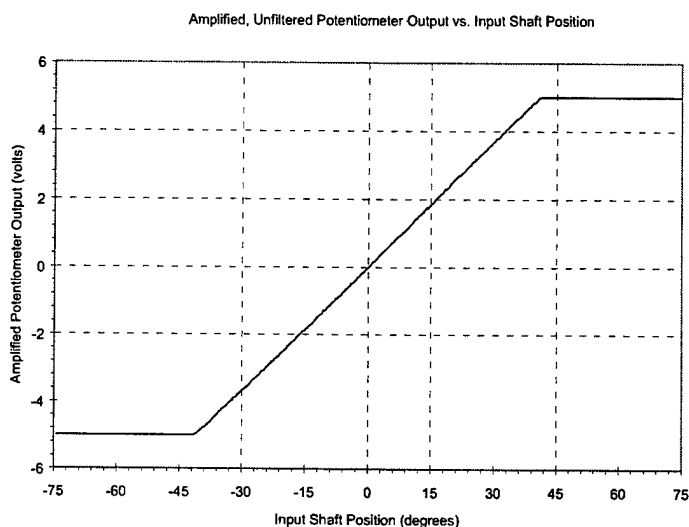


Figure 4: Potentiometer Amplifier Circuit



**Figure 5: Amplified Pot Output vs. Input Shaft Position**

These potentiometers are intended to directly measure the deflection of the compliant element, and not the overall motion of the joint. In the latter case, the pot would be easier to install, but the deflection would be the difference of the total joint motion and the motor motion. This subtraction of two sensor signals would be corrupted by noise and may even be unusable. Instead, the pot is mounted so that the drive shaft, which is rigidly attached to the front side of the compliant element, attaches to the pot's input shaft, while the threaded portion of the compliant element (i.e. the back side) attaches to the pot's housing. In this configuration, the pot directly measures the relative motion between the two halves of the compliant element, and is not influenced by overall motion of the joint.

In the original design, JDK Controls Corporation potentiometer kits were initially used, but required replacement by the Midori pots. These JDK kits contained the innards of a conventional pot (element, wiper, and redundant contacts) without the bulky housing. The assembled pot kit measured only .70" in diameter and .25" thick and accepted a through shaft, allowing better integration of the pot and compliant element body. However, the output signal was not clean enough to differentiate, and so it could not be used without limiting the capabilities of the controller.

In the future, the Midori potentiometer should be replaced by an encoder kit to further increase sensor performance. The encoder would be even less susceptible to sensor noise, and would have a derivative that is smoother still. However, currently available encoders that provide at least 500 LPR do not allow through shafts and are much too large to be used on these compliant elements. Instead, an encoder kit, consisting of a code wheel and an optical array without the housing, could be mounted in a manner similar to the JDK

Controls pot kit. Precise spacing and alignment of the code wheel with the optical array would be required, as well as shielding of the whole encoder assembly from dust.

## **5 SINGLE-AXIS TEST STAND**

A single-axis test apparatus was constructed to aid in designing a torque control algorithm for the motor/spring system, and to measure the performance enhancements that the exponential compliance provides. The apparatus consisted of a single, gear-reduced DC motor with an optical encoder at the back to measure motor position and an instrumented compliant element at the front. The output side of the compliant element was locked in place in some tests and was free to rotate in others. These tests helped to assess the effectiveness of various control strategies, and to suggest modifications or additions to the control algorithm.

The final controller that resulted from these tests consisted of two distinct segments: a high bandwidth, inner position control loop and a lower bandwidth outer torque loop. The outer loop uses the torque error to compute a commanded motor position, which can accurately be tracked by the fast inner loop. The performance of this controller was assessed by tracking step and sinusoidal torque commands, by determining the torque resolution and dynamic range, and by measuring the frequency response of the system.

### **5.1 Mechanical Setup**

The test apparatus, shown in Figure 6, is similar to the actuator mechanism on the actual finger, since exactly the same components were used. The instrumented compliant element is mounted to a drive shaft powered by a Maxon RE016-039 DC motor with an HP HEDM-5500 512 LPR optical encoder to measure motor position and a Maxon 84.3:1 planetary gear reduction. The gearhead's output shaft was connected to the drive shaft with a Helical Products flexible coupling. The compliant element was locked to one of the drive shaft supports in some experiments to simulate the finger in contact with a fixed object. In other experiments, the element was allowed to rotate while random disturbances were manually applied, simulating a finger movement.

**Figure 6: Single-Axis Test Stand**

This test stand is a simplified representation of the actual finger drive mechanism, as intended. The real finger contains three of these functional groups, and all three are coupled together by a cable transmission so that the motion of one axis can affect the other two. Furthermore, the inertial load driven by each axis of the finger is much larger and constantly changes with the link positions. However, in developing a control strategy with the simplified test apparatus, one can more easily discern the advantages and drawbacks of each algorithm, perceive the effects of controller modifications, and observe the dynamics of the system. It is expected that the controller gains used in the test stand will require modification for use in the actual finger, but the controller's structure will remain the same.

Very basic mathematical models of the test apparatus were developed to provide an even more simplified baseline for controller development. In the models, the apparatus was considered to be a rotating inertia connected to one end of a torsional spring through a thin, massless rod. The other end of the spring was rigidly connected either to ground in one model, or to another rotating inertia in the other model. A schematic diagram and the governing dynamic equations of each are shown in Figure 7 and Figure 8. These basic models completely neglect backlash in the gearhead, friction in the motor and the gearhead, damping in the spring, and flexibility of the drive shaft, but they are sufficient for aiding in controller design. The models were used with MATLAB™ to quickly test various controller changes, and also to observe parameters and system states that cannot be measured with the actual system.

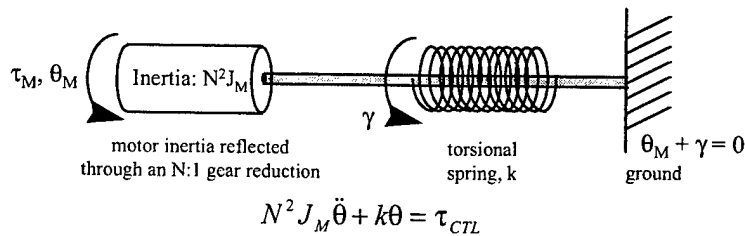


**Figure 7: One-DOF, Fixed-End Model**



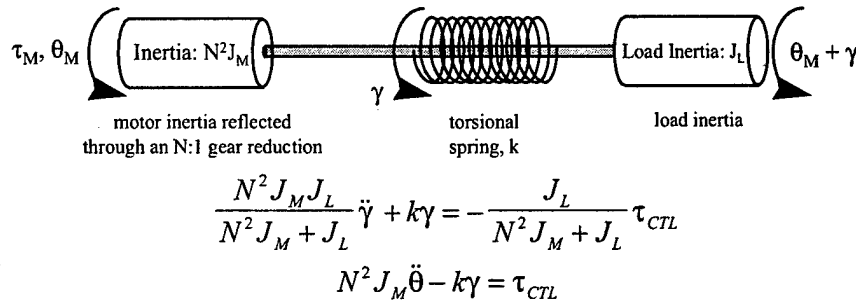


**Figure 8: Two-Inertia Model**

It was intended that controller analysis and design would first be performed with the one-DOF grounded model since it is much simpler to manipulate, and then additional fine tuning would be performed with the aid of the more realistic two-inertia model. However, the controller and gains derived with the simpler model performed quite well on the actual test stand even when the spring was free to rotate, so the two-inertia model was not used. But, if the need arises in the future, the analysis presented here can be repeated with the two-inertia model to perhaps build an even better control system.

## 5.2 Controller

The control structure shown in Figure 9 was applied to the test system to implement force control of the single joint. This type of algorithm, inspired by Salisbury [Salisbury, 1984], combines a stable, high gain, high bandwidth motor position control loop with a low gain, low bandwidth torque feedback loop. The inner position loop can achieve high bandwidth because there are no dynamics between the collocated encoder and actuator, and because the encoder has an extremely clean output and derivative. In contrast, the torque feedback loop does not have a collocated sensor and actuator pair. In fact, all of the dynamics of this flexible system lie between the potentiometer and the motor. Furthermore, the potentiometer signal has a noisy derivative, which further limits the magnitude of the derivative gain.

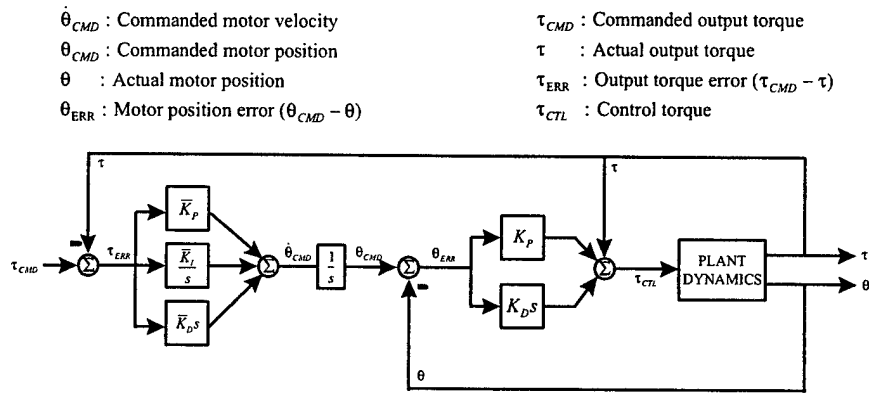


Figure 9: Controller Schematic Diagram

The branch of the feedback loop that adds the current output torque to the control torque is an attempt to remove some nonlinearity from the system. This can be seen by considering the fixed-end system model discussed in Chapter 5.1:

$$\text{dynamic equation of motion: } N^2 J_M \ddot{\theta} + k\theta = \tau_{CTL}$$

$$\text{but, the control torque is: } \tau_{CTL} = k\theta + K_P(\theta_{CMD} - \theta) + K_D(\dot{\theta}_{CMD} - \dot{\theta})$$

$$\text{so that the nonlinear } k\theta \text{ terms cancel: } N^2 J_M \ddot{\theta} + k\theta = k\theta + K_P(\theta_{CMD} - \theta) + K_D(\dot{\theta}_{CMD} - \dot{\theta})$$

$$\text{leaving a seemingly linear equation } N^2 J_M \ddot{\theta}_{ERR} + K_D \dot{\theta}_{ERR} + K_P \theta_{ERR} = 0$$

It appears that the result is a linear equation with equilibrium at the current operating point of the spring, about which the spring is linear to leading order. But,  $\theta_{CMD}$  and  $\dot{\theta}_{CMD}$  are functions of the nonlinear stiffness, so the equation is still nonlinear, although some nonlinearity has been removed.

The transfer function from torque command to torque output, shown in Equation 2, was computed using the fixed-end model discussed in Chapter 5.1. It is important to note that the transfer function actually changes with the position of the spring, since the stiffness  $k$  is variable. However, Equation 2 is valid for small motions about a particular spring position, and is instantaneously valid when large motions are considered.

$$H(s) = \frac{\tau}{\tau_{CMD}} = \frac{k(K_D \bar{K}_P + K_P \bar{K}_D)s^2 + k(K_D \bar{K}_I + K_P \bar{K}_P)s + kK_P \bar{K}_I}{N^2 J_M s^4 + (K_D + kK_D \bar{K}_D)s^3 + (K_P + kK_D \bar{K}_P + kK_P \bar{K}_D)s^2 + k(K_D \bar{K}_I + K_P \bar{K}_P)s + kK_P \bar{K}_I}$$

Equation 2: Torque Command to Output Transfer Function

### 5.2.1 Loop Stability

Since no integrators are used on the inner position control loop, stability of that loop is guaranteed for any reasonable choice of PD gains. Strictly speaking, an ideal mass-spring-damper system with a PD controller is always stable regardless of controller gains since energy is always being removed from the system [Slotine, 1990]. However, the real system is not ideal. Rather, it is subject to actuator saturation limits and phase lag in computing the filtered sensor derivative, which can induce instability if the gains are made exceedingly high.

In the outer torque feedback loop, the use of integrators is unavoidable. In fact, two integrators are required, one to overcome steady-state errors caused by gearhead friction and the other to eliminate steady-state errors in response to ramp changes in the spring position. These integrators are a source of instability to the system and represent an additional limitation on the controller gains and bandwidth. The first integrator converts the commanded motor velocity to a commanded motor position and is needed because the substantial gearhead friction ( $\sim 20\text{mNm}$ ) can prevent the motor from moving when small velocities are commanded. If this were to occur, the motor position command and error would ramp, due to the integrator, until the PD control torque is larger than the break-out friction. This integrator could have been added to the inner loop instead, making it a PID velocity controller. However, this would adversely affect the stability and bandwidth of the inner loop.

The second integrator is part of the outer PID torque feedback loop and contributes a component of the commanded motor velocity based on the torque error. It is needed to create a controller of high enough order to be able to produce the required spring deflection when the output side of the spring is moving, which occurs in the three-axis system whenever finger motion is desired. When this happens, the motor must be able to track the output position of the spring just to keep the spring deflection constant. Additional motor motions must then be superimposed to modulate the spring deflection based on the commanded output torque. The integrator successfully removes the steady-state torque error that would normally result in response to a unit ramp movement (i.e. constant unit velocity) at the output side of the spring. Although the actual fingers will not be limited to constant velocity movements, the higher order controller is better suited for handling more complex motions.

### 5.2.2 Filters

Digital filters were implemented in software to reduce noise from the sensor output signals and their derivatives, which were computed in software by back-differencing. The fourth order low-pass filters were created by cascading two minimum phase, critically-damped second order systems, and implemented with a Direct Form II Transposed structure. The cutoff frequencies were selected by carefully balancing noise attenuation (low cutoff) with minimal time delay (high cutoff).

Adequate noise attenuation was achieved on all sensor signals except the potentiometer derivative. The encoder output signal was extremely clean and did not require any filtering other than that intrinsic to the encoder reading chips on the SensAble Technologies PC Interface Card. The encoder derivative and the potentiometer position signals needed only high bandwidth (1000 Hz and 400 Hz, respectively), low time delay filters which were easily implemented. But, the potentiometer derivative signal was extremely noisy and required a very low bandwidth filter that could not be implemented without introducing time delay instabilities to the control loop. Instead, a moderate bandwidth filter (150 Hz) was selected. This filter maintained stability while moderately reducing the noise, but the derivative gain of the outer control loop was severely limited.

The noise on the potentiometer derivative signal was mainly due to A/D board fluctuations of  $\pm 1$  bit in reading the pot output. This 1 bit fluctuation, which is the rated accuracy of the ComputerBoards CIO-DAS08 board, causes enormous noise when back-differencing to compute the derivative. Several failed attempts were made to solve this problem, including filtering with analog circuits, using a better A/D board, and ignoring the least significant bit (LSB) of the A/D conversion. Active analog differentiators and low-pass filters were created using op amps, resistors, and capacitors. However, the output of these circuits was contaminated by ambient 60 Hz noise, which could not be filtered without introducing excessive time delay. Furthermore, a higher performance A/D board (Data Translation DT31EZ) was tried, but the 1 bit fluctuation persisted and the signal quality did not improve. Finally, the LSB of the A/D conversion was dropped. But that too did not significantly improve signal quality, because a 1-bit fluctuation can affect more than just the LSB. For example, the difference between 3 (011) and 4 (100) is only 1 bit but changes all 3 bits. The best solution would be to replace the potentiometers with digital encoders so that A/D conversion is not necessary at all and the noise associated with analog signals is eliminated.

### 5.2.3 Selection of Time-Varying Gains

The selection of time-varying controller gains was performed by using the fixed-end dynamics model and the torque input/output transfer function (Equation 2) to choose a desired closed-loop bandwidth for both the inner and outer control loops. However, the transfer function is only instantaneously applicable because of the changing spring stiffness. For this reason, the controller gains selected in this way are also instantaneously applicable, and vary as a functions of the spring stiffness, so that the bandwidth remains fixed for any spring position. As discussed earlier, high bandwidth was chosen for the inner, collocated control loop, and lower bandwidth for the outer loop.

The denominator of the torque transfer function was manipulated and analyzed to determine the relationship between the gains and the bandwidth of the individual control loops, so that particular controller gains that achieve the desired bandwidth could be computed. The denominator is shown here:

$$N^2 J_M s^4 + (K_D + kK_D \bar{K}_D) s^3 + (K_P + kK_D \bar{K}_P + kK_P \bar{K}_D) s^2 + k(K_D \bar{K}_I + K_P \bar{K}_P) s + kK_P \bar{K}_I$$

This denominator was then written as the product of the following two terms:

$$N^2 J_M (s^2 + \frac{K_D}{N^2 J_M} s + \frac{K_P}{N^2 J_M}) (s^2 + \frac{kK_D \bar{K}_D s^3 + k(K_D \bar{K}_P + K_P \bar{K}_D) s^2 + k(K_D \bar{K}_I + K_P \bar{K}_P) s + kK_P \bar{K}_I}{N^2 J_M s^2 + K_D s + K_P})$$

The first term represents the inner velocity loop, and is a simple second order oscillator whose parameters can be chosen to yield a critically damped system with the desired bandwidth. Equation 3 explicitly states the relationship between the inner loop gains and the corresponding bandwidth.

$$K_P = N^2 J_M \omega_{C, INNER}^2$$

$$K_D = 2N \sqrt{J_M K_P}$$

### Equation 3: Inner Loop Controller Gains as a Function of Bandwidth

The second term represents the outer torque control loop, and was expanded via long division to be a second order system with two remainder terms:

$$s^2 + \frac{kK_D \bar{K}_D}{N^2 J_M} s + \frac{k}{N^2 J_M} (K_D \bar{K}_P + K_P \bar{K}_D - \frac{K_D^2 \bar{K}_D}{N^2 J_M}) + \frac{k(K_D \bar{K}_I + K_P \bar{K}_P - \frac{2K_D \bar{K}_D K_P}{N^2 J_M} - \frac{K_D^2 \bar{K}_P}{N^2 J_M} + \frac{K_D^3 \bar{K}_D}{N^4 J_M^2}) s}{N^2 J_M s^2 + K_D s + K_P} + \frac{k(K_P \bar{K}_I - \frac{K_P^2 \bar{K}_D}{N^2 J_M} - \frac{K_D \bar{K}_P K_P}{N^2 J_M} + \frac{K_P \bar{K}_D K_D^2}{N^4 J_M^2})}{N^2 J_M s^2 + K_D s + K_P}$$

By setting each of these terms to an appropriate value, the bandwidth can be arbitrarily set. However, that requires independent control of four terms with only three variable gains, which is an under-constrained problem and does not have an exact solution. Therefore, in this analysis, the first three terms were explicitly solved to achieve a target bandwidth that is BWF (Bandwidth Factor) times the bandwidth selected for the inner loop. The final term was viewed as a perturbation on the desired pole positions, and will shift the bandwidth slightly away from the target. Equation 4 shows the relationship between the outer loop gains and the target bandwidth.

$$\omega_{C, OUTER} = BWF \omega_{C, INNER}$$

$$\bar{K}_P = \frac{K_P BWF(BWF - 1)}{kK_D} + \frac{K_D BWF}{kN^2 J_M}$$

$$\bar{K}_I = \frac{K_P BWF (K_D^2 BWF - K_P N^2 J_M (BWF - 1))}{k K_D^2 J_M} \quad \bar{K}_D = \frac{BWF}{k}$$

**Equation 4: Outer Loop Controller Gains as a Function of Bandwidth**

When these gains are substituted into the equation, the denominator becomes:

$$N^2 J_M (s^2 + 2\omega_{C,INNER} s + \omega_{C,INNER}^2) (s^2 + 2BWF\omega_{C,INNER} s + BWF^2\omega_{C,INNER}^2) - \frac{K_P^3 BWF (BWF - 1)}{K_D^2 (N^2 J_M s^2 + K_D s + K_P)}$$

The final term in this equation is the perturbation that shifts the poles and the bandwidth that are specified by the gains in Equation 4. However, numerical tests showed that this perturbation is small and can be compensated for by slight tweaking of the gains.

A least squares minimization approach could have been used to compute the gains that come closest to achieving the target bandwidth (i.e. minimize the perturbation), but this additional mathematical complexity was deemed unnecessary because the perturbation in the approach described above is small.

Experiments with the inner velocity loop showed that stable controllers as fast as 150 Hz are possible, but these gains cause tremendous actuator saturation. Therefore, somewhat smaller inner loop gains were desired, and a bandwidth of 100 Hz was selected. The outer loop bandwidth was chosen to be significantly slower at 10 Hz, which is on the order of human finger force bandwidth, which has been measured at 7-20 Hz [Brooks, 1990; Tan, 1994].

To implement this time-varying controller, the spring stiffness is computed at each iteration of the servo loop using the spring deflection and Equation 1. This computed stiffness is then used to compute new controller gains that maintain the desired bandwidth for the current instantaneous spring position. The controller was tested using these gains on the single-axis stand, and slight modifications were made to optimize performance.

## 5.2.4 Controller Modifications

In implementing the controller shown in Figure 9, two main modifications were made that don't show up in a schematic diagram. First, the current delivered from the amplifiers to the motor was limited by the software, and second, an integrator windup prevention algorithm was added. The first modification is required because there is a limit to the amount of current that can pass through a DC motor without burning out the motor. A simple saturation level was implemented to prevent current greater than the rated maximum continuous current. However, additional methods exist that allow current and torque greater than

the maximum continuous levels, while still protecting the motors. Some of these methods involve limiting the duration for which these larger currents are applied instead of preventing them altogether. These methods would allow faster response and higher performance, but could possibly result in damage to the motor if not implemented perfectly, and so they are not used here.

Another side effect of actuator limits is instability caused by integrator windup, which is especially prevalent with this controller since two integrators are used. The integral gains need to be relatively large to quickly remove steady-state errors near the end of the motion, but those high gains lead to unexpected problems during the initial, large scale motions where actuator saturation is common. In particular, when the actuators saturate, the integrators continue to command larger and larger output torque which the actuators cannot deliver. Therefore, the integrators wind faster than the controller can remove the error, leading to extremely large overshoot and, sometimes, instability. This effect can be seen by comparing Figure 10 with Figure 11, which both show responses without windup prevention. The first plot shows a stable step response with almost zero overshoot for a step size of 5 mNm. In this response, very little motor saturation occurs, so the integrator instability is not seen. However, Figure 11 shows the response due to a larger step input of 40 mNm. This time, extensive actuator saturation occurs during the initial movement, and a 25% overshoot results.

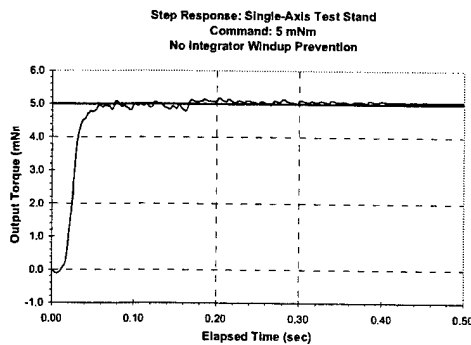


**Figure 10: 5 mNm Step Response w/o Integrator Windup Protection**

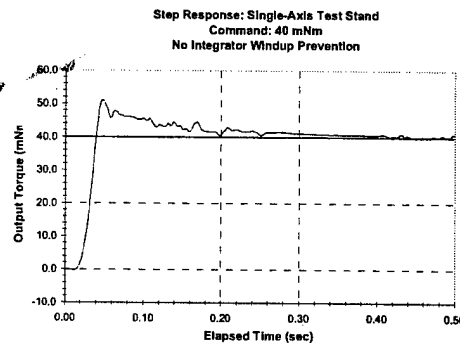


**Figure 11: 40 mNm Step Response w/o Integrator Windup Protection**

To combat this problem, the integrators are turned off in the software whenever the actuators are saturated, which prevents unchecked integrator windup. Figure 12 shows a stable step response after implementing this controller modification with exactly the same gains and 40 mNm step size that previously led to large overshoot. The overshoot has been completely eliminated by this change. Furthermore, Figure 13 shows a step response for a much larger step input of 150 mNm that results in even more extensive actuator saturation, but does not lead to instability or excessive oscillations, proving the effectiveness of the integrator windup prevention technique.

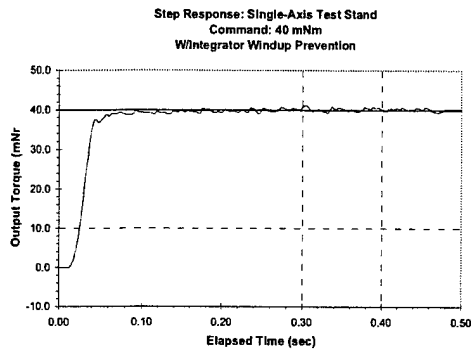


**Figure 12: 40 mNm Step Response With  
Integrator Windup Prevention**

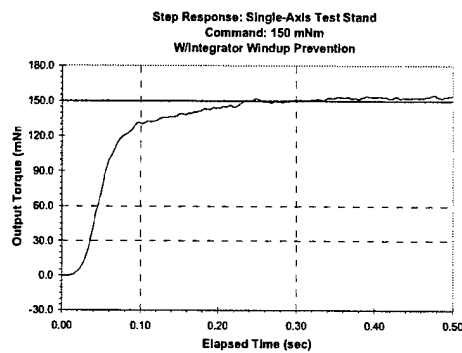


**Figure 13: 150mNm Step Response With  
Integrator Windup Prevention**

This method for preventing integrator windup works better than simply limiting the value of the integral. In the technique that is used here, the integrator only contributes to the overall control torque when it is needed, such as near the end of a movement when steady-state errors are more prominent and the proportional and derivative control components are small. The integrator is not usually needed at the beginning of a movement where the proportional term dominates. Simply capping the integral does not provide this type of selectivity, so it was not employed.

### 5.3 Performance

Torque controller performance was measured by the ability to track step and sinusoidal inputs and to reject disturbance torques applied to the endpoint. Furthermore, measurements were made to determine the resolution of torque control and sensing, which leads to an estimate of dynamic range and an assessment of contact sensing ability. Finally, frequency response measurements were made to determine the bandwidth of the controller.

#### 5.3.1 Trajectory Tracking

The first part of the controller performance tests involved tracking of step and sinusoidal torque commands with fixed output position of the compliant element. Step commands of varying amplitude were applied to the system, and performance was measured via settling time and RMS error after settling. Since overshoot was eliminated by gain choice and integrator windup prevention, maximum overshoot and rise time were not used to measure performance. The sinusoidal commands varied in both amplitude and frequency, and performance was measured by the RMS error after the transients have died away.

The following plots in Figure 14 show step responses of magnitude 10, 30, 75, and 150 mNm, as well as the tracking error after settling. In addition, settling time and RMS error are tabulated. These results show that



the fast response is achieved even for large step sizes, with the longest settling time of ¼ second for a step of 150 mNm. Also, the RMS tracking error, expressed as a percentage of the commanded torque was fairly constant at about 5% regardless of the magnitude of the torque, as desired.

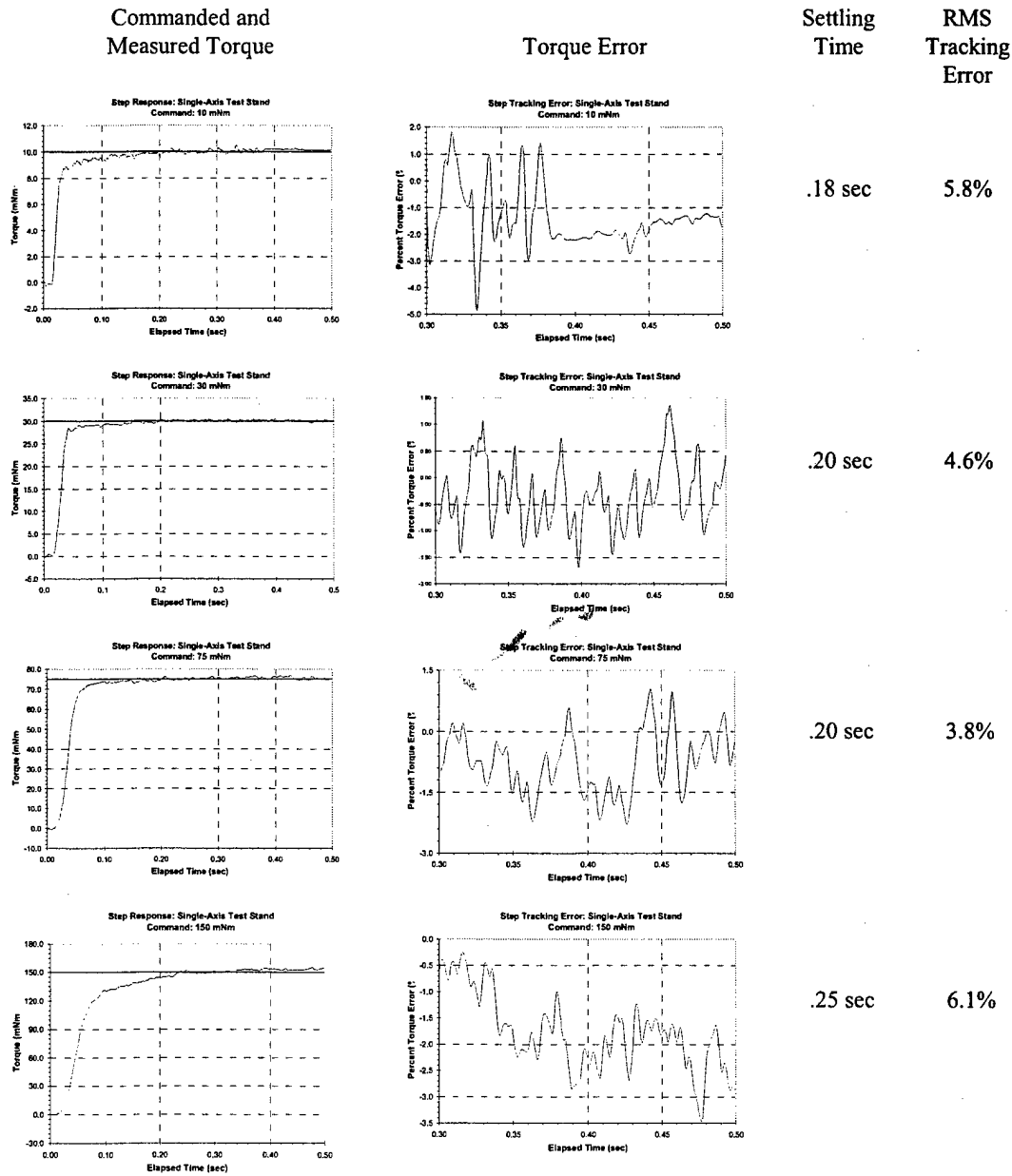


Figure 14: Step Tracking Performance

The following plots in Figure 15 show tests on sinusoidal tracking of various amplitude and frequency, ranging from 5 mNm to 100 mNm in amplitude and 0.25 Hz to 1.0 Hz in frequency. The controller tracks

these trajectories fairly well, except at the transitions where the velocity changes sign, i.e. at the peaks of the torque traces. At this point there is usually a spike in the torque error lasting about .10 seconds as an additional transient dies away. The size of this error spike varied for the different trials, so the overall RMS error was not consistent. However, if these spikes are disregarded, the RMS error would remain fairly constant for all the trials.

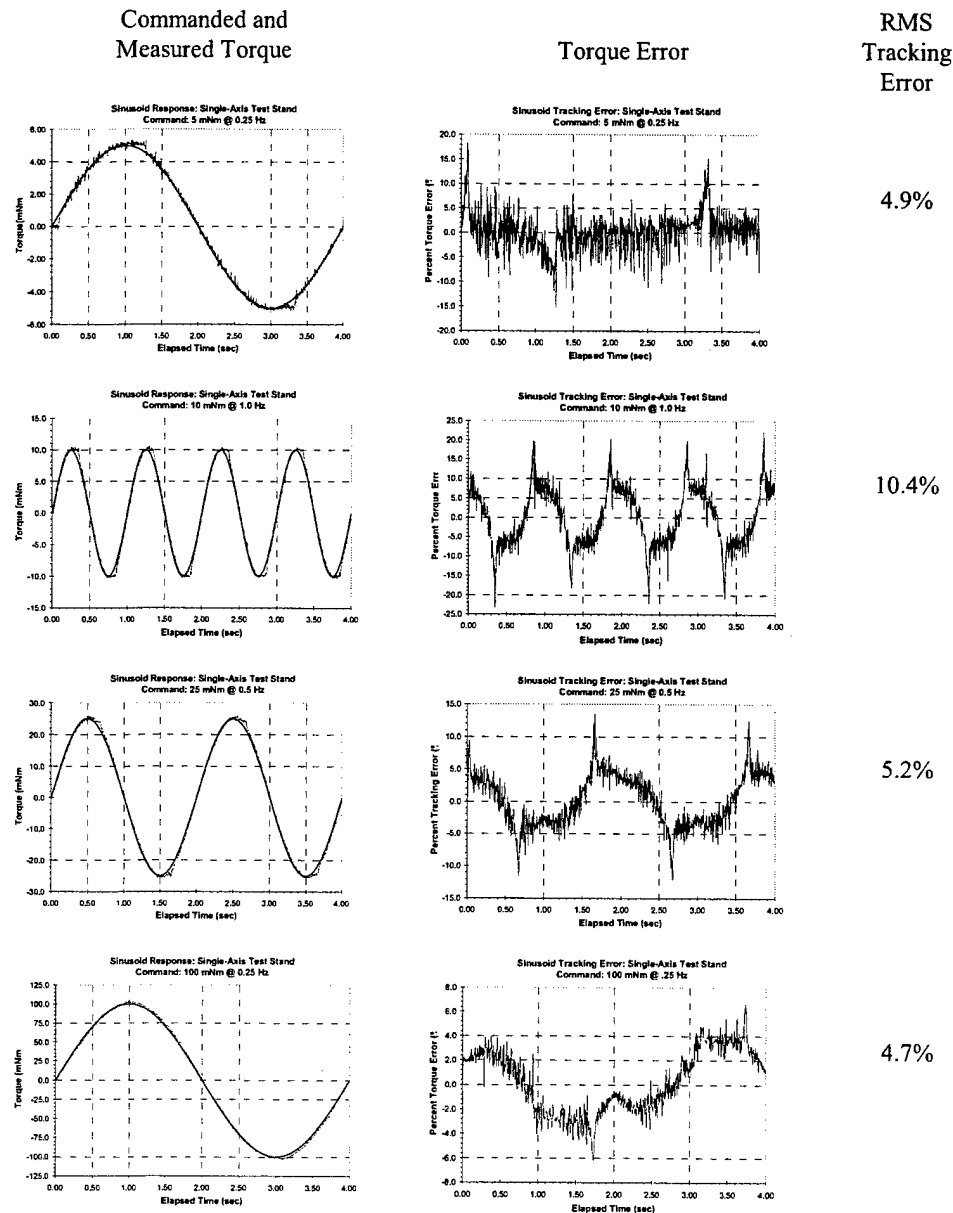
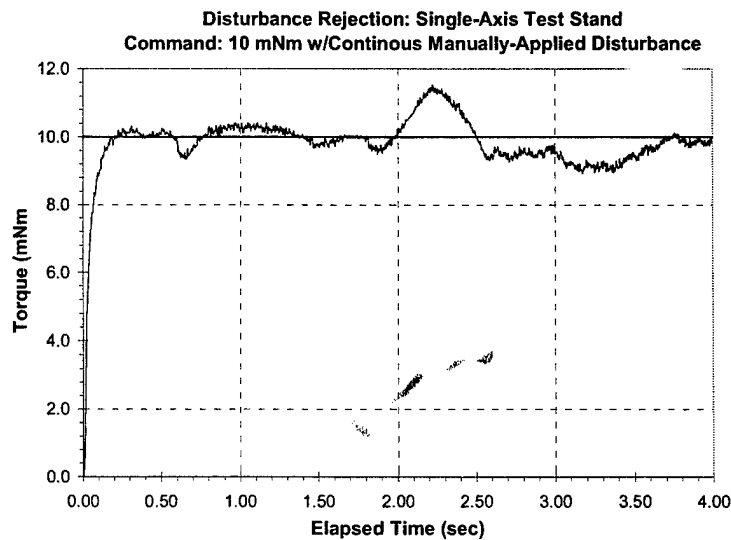


Figure 15: Sinusoidal Tracking Performance

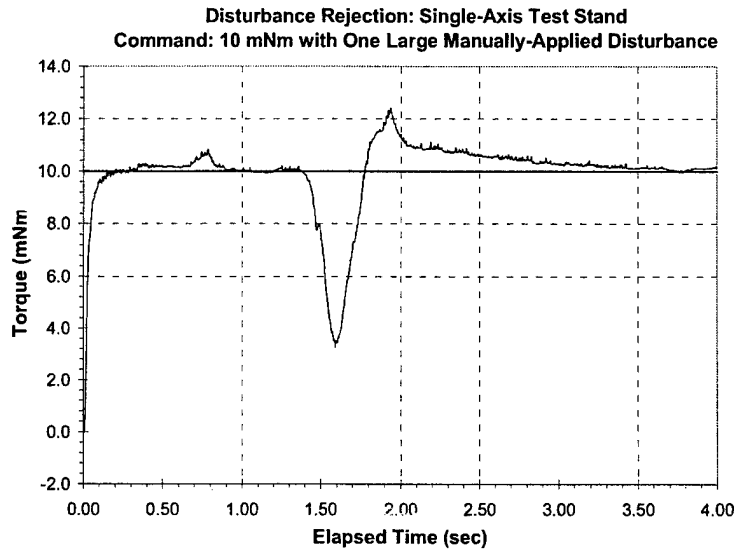
The second part of the performance evaluation involved torque control with the output side of the spring free to rotate while random disturbances are applied. These controller tests required tracking of a constant torque while random perturbations in torque and position were manually applied to the output side of the compliant element.

Figure 16 shows one such response. In this trial, a constant torque of 10 mNm was commanded while small disturbances were manually applied by holding the output side of the compliant element and slightly twisting back and forth. Because of the method by which these disturbances are applied, the magnitude of the disturbance is not known. However, by inspecting the plot, one can see that the disturbance does not excite oscillations or instabilities, and the commanded 10 mNm tracking is maintained.



**Figure 16: Rejection of Continuous Random Disturbances by Torque Controller**

A similar trial was performed with a single, large disturbance spike. This trial is intended to assess how quickly the controller can recover from such a disturbance, since it is of course not fast enough to track the commanded torque during the spike. Figure 17 shows this response profile. The plot shows that the controller responds quickly, but the rebound causes overshoot which is slowly eliminated by the integral gains.



**Figure 17: Rejection of Large Spike Disturbances by Torque Controller**

These tests were designed to assess the performance of the controller in the face of disturbances that will be present in the three-axis finger. Disturbance torques will exist due to coupling among the finger joints; that is, torque applied by a single motor can induce torque on all the joint axes and all the motors. Also, the need to control torque while changing the output position of the compliant element will exist whenever fingertip force is to be controlled during finger movements, as with grasp gaits.

### 5.3.2 Performance Measures

The overall measure used here to determine torque control performance is torque resolution, which is closely related to contact sensing ability and dynamic range. Torque resolution was shown in Figure 14 to be about 5% and is independent of the magnitude of the torque. Table 1 was created to show the amount of spring deflection that produces 5% resolution for each of the four torque levels shown in Figure 14. This spring deflection was computed through the inverse of the spring torque-deflection relationship given in Equation 1. Not surprisingly, the allowable spring deflection is about  $\pm 0.004$  rad (or  $\pm 0.25^\circ$ ) for each torque level, and is precisely equal to the resolution of the potentiometer used to measure the spring deflection (given in Chapter 4.2). Therefore, torque control resolution is governed by the resolution of the sensor used to measure the deflection of the compliant element.

Nominal Torque Level	Nominal Torque $\pm 5\%$	Allowable Change in Spring Position to Stay Within $\pm 5\%$ of Nominal Torque
----------------------	--------------------------	--

10	9.5 $\leftrightarrow$ 10.5	$\pm 0.0038$ rad
30	28.5 $\leftrightarrow$ 31.5	$\pm 0.0036$ rad
75	71.2 $\leftrightarrow$ 78.8	$\pm 0.0031$ rad
150	142.5 $\leftrightarrow$ 157.5	$\pm 0.0060$ rad

**Table 1: Allowable Change in Spring Position for a 5% Change in Applied Torque**

Using this result, the minimum controllable torque and the dynamic range can be determined. The minimum torque is the same as the torque resolution at the neutral position of the spring, and is computed using the spring torque-deflection equation to be .50 mNm. The largest torque that can be exerted is strictly governed by the allowable current to the motor. For the gear-reduced Maxon RE016 DC motors used in the test stand and fingers, the maximum continuous torque is 530 mNm, giving a dynamic range of about 1000.

This dynamic range represents a significant improvement over the same system without the compliant element, and over other methods of increasing dynamic range. Without the compliant element, the maximum torque that can be applied is still determined by the current limit of the motor, but the minimum torque is given by the gearhead friction which was measured to be 15 mNm. This gives a dynamic range of 35, a factor of 30 less than the new system. Furthermore, Morrell [Morrell, 1995] used a micro-macro actuator system to achieve an overall dynamic range of 800. This is still slightly lower than that achieved in the current non-linearly compliant system, but Morrell's actuator does not sacrifice bandwidth to accomplish this gain in dynamic range.

Contact is detected by observing jumps in the measured joint torques; therefore, contact sensing ability is directly related to the torque sensing resolution. The best resolution occurs at zero mean torque, so a .50 mNm torque on the joint is enough to determine that contact has been made. However, in the actual finger contact will not normally occur at zero mean torque since the weight of the finger links will deflect the compliant elements slightly. Instead, contact will usually occur at non-zero nominal spring deflection, resulting in poorer resolution.

### 5.3.3 Bandwidth

Adding mechanical flexibility to a stiff system automatically reduces the bandwidth of the system by lowering the natural frequency of vibration. Therefore, rapid, high acceleration movements will not be possible with the flexible system. However, researchers have shown that human fingers do not require high bandwidth to achieve dexterity, but rather high dynamic range. This helps to justify the tradeoff of bandwidth for dynamic range.

Figure 18 and Figure 19 show the bandwidth of the overall torque controller and the inner loop position controller, respectively. The controller gains were chosen to achieve approximately 10 Hz bandwidth of the overall system, and 100 Hz for the inner position loop, as discussed in Chapter 5.2.3. The experimentally obtained frequency response plots verify that this is indeed the bandwidth of the actual system, thereby validating the time-varying gain selection technique.

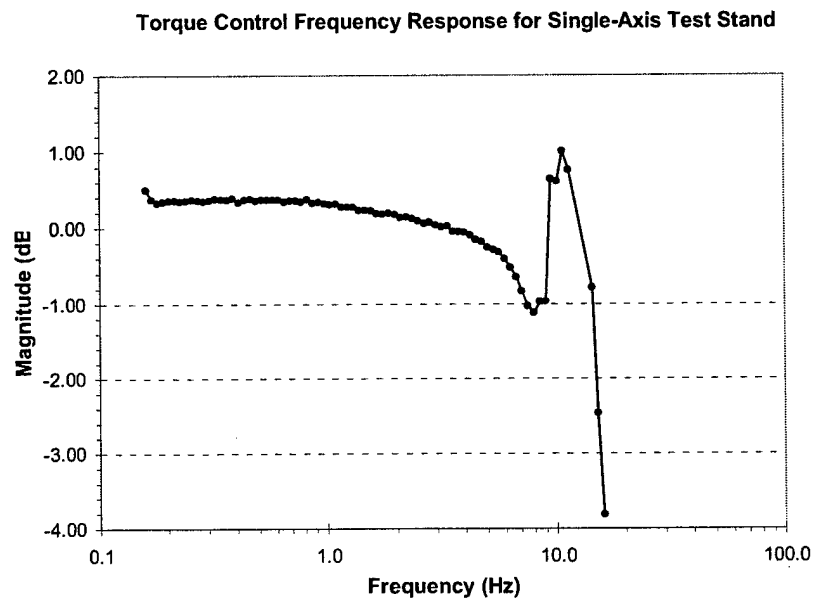


**Figure 18: Frequency Response of the Overall Torque Control System**

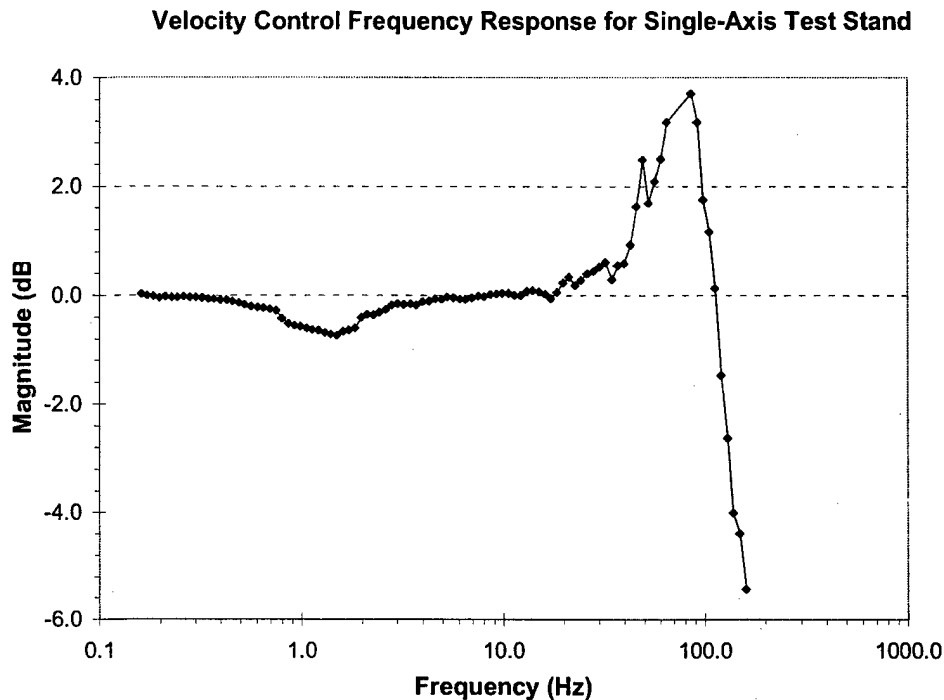


**Figure 19: Frequency Response of the Inner Loop PD Position Controller**

## 6 FINGER DESIGN

The robotic finger, shown in Figure 20, is a three-DOF design with kinematics similar to that of a human finger: nearly intersecting roll and pitch axes at the base “knuckle” and an additional pitch axis on the finger “digits”. The range of motion was designed to be much larger than human fingers with  $180^\circ$  on the two base axes and  $270^\circ$  on the distal axis. The range of motion gives each finger a large, hemispherical workspace, so that an array of fingers can more easily manipulate objects. Link lengths were chosen to ensure the existence of isotropic points in the workspace, and to make the fingers about twice the size of their human counterparts. The finger is actuated by three DC motors that are detached from the finger joints and located beneath the links. Torque is transmitted to the joints by a system of cables and pulleys. Optical encoders on the motors are used to sense position and velocity, while potentiometers attached to the compliant elements measure the spring deflection, from which the applied torque is inferred.

**Figure 20: Original Finger Design**

### **6.1 Kinematics**

In determining the kinematic form of the robotic finger, several possibilities were considered before finally adopting kinematics similar to that of human fingers. Some of these possibilities included kinematics similar to the PHANToM™, the WAM, and even several designs utilizing prismatic base joints. Simple, passive, “stick” models were made for many of the designs. These models were then used to qualitatively evaluate each design by manually moving the links to perform grasping operations. Using the results of these tests, the kinematics shown in Figure 21 was chosen.

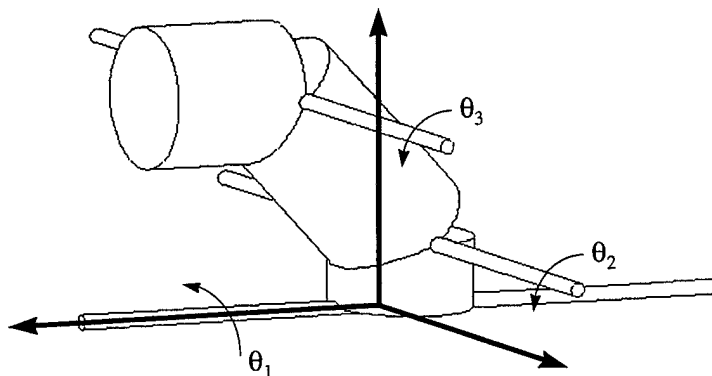


**Figure 21: Chosen Finger Kinematics**



The kinematics of this three-DOF design is similar to that of human fingers, with two main differences. Both have roll and pitch axes of motion at the base of the finger and a second pitch axis on a distal link. However, the two base axes intersect in the human finger, but do not in the selected model. Instead, the pitch axis is shifted slightly upward, which makes actuation easier, allows greater range of motion, and makes for a more compact drive system. The distance of the shift was consciously made as small as practical so that the finger behavior will be similar to that of human fingers.

The second difference is that human fingers have a third link near the fingertip with another pitch axis of motion, giving a total of four joints. However, it is believed that this additional joint is not vital for dexterous manipulation tasks, such as grasp gaits, that require fingertip contact with an object, but it is important for power grasps which involve wrapping the entire finger around an object and making contact with the finger walls as well as the tips. Furthermore, the additional joint is not a completely independent freedom; it's motion is strongly coupled to the motion of the preceding joint. In fact, it is very difficult and awkward for humans to move one of these final two joints without moving the other, and virtually impossible to move them both independently. Other robot finger designs, such as those on the Salisbury Hand, have also eliminated this joint. In another hand, the Anthrobot-2, the joint is included but is kinematically constrained to move with the preceding joints, so only 3 DOF are present.

## 6.2 Link Lengths

The lengths of each finger link were chosen such that a locus of isotropic points would exist in a desirable location within the workspace, as was done by Salisbury [Mason, 1985]. Isotropic points are locations where the fingertip will have the greatest dexterity because it can exert equal forces in all directions. Quantitatively, these positions are such that the condition number of the jacobian is 1.

### 6.2.1 Jacobian

The correct jacobian to be used in these calculations transforms motor torque to fingertip force. This is not the same as the traditional joint-to-tip jacobian since an additional transformation is required to convert motor torque to joint torque due to the coupling induced by the system of cables and pulleys that transmit torque from the motors to the joints. The relationship between motor torque and joint torque is represented by a constant, lower-triangular transformation matrix that is based on the pulley diameters in the cable transmission. This constant matrix multiplies the traditional jacobian to give the total jacobian matrix, as shown in Equation 5. This total motor-to-tip jacobian should be used to locate isotropic points, since the motors are the source of torque to the system.

$$\begin{bmatrix} 0 & L_2 C \theta_2 + L_3 C(\theta_2 + \theta_3) & L_3 C(\theta_2 + \theta_3) \\ -L_1 C \theta_1 - (L_2 C \theta_2 + L_3 C(\theta_2 + \theta_3)) C \theta_1 & (L_2 S \theta_2 + L_3 S(\theta_2 + \theta_3)) S \theta_1 & L_3 S \theta_1 S(\theta_2 + \theta_3) \\ -L_1 C \theta_1 - (L_2 C \theta_2 + L_3 C(\theta_2 + \theta_3)) S \theta_1 & (L_2 S \theta_2 + L_3 S(\theta_2 + \theta_3)) C \theta_1 & -L_3 C \theta_1 S(\theta_2 + \theta_3) \end{bmatrix} \begin{bmatrix} A & 0 & 0 \\ B & C & 0 \\ D & E & F \end{bmatrix} = \begin{bmatrix} TOTAL \\ JACOBIAN \\ TRANSFORMATION \end{bmatrix}$$

	Motor	
Joint - to - Tip Transformation	to	Total
	Joint	

#### Equation 5: Components of the Total Jacobian Matrix

However, setting the condition number of the total jacobian to 1 yields a set of nonlinear equations that cannot explicitly be solved for the link lengths and joint angles that produce isotropic points. Therefore, the traditional joint-to-tip transformation was used instead of the total jacobian, even though the results of this calculation are inexact. But, Salisbury [Salisbury, 1982] showed that the condition number changes very slowly as the distance from the isotropic point increases, so the calculation results should be close, although not precisely correct.

### 6.2.2 Results of Calculations

Calculations using the joint-to-tip jacobian directly follow the derivation in [Mason, 1985], and show that isotropic points exist when  $L_2 = \sqrt{2}L_3$ ,  $\theta_2 = 45^\circ$ ,  $\theta_3 = 135^\circ$ , and  $L_1$  and  $\theta_1$  are arbitrary. As  $\theta_1$  varies, these isotropic points form a circular locus of radius  $L_1$  centered about the roll axis, and whose plane is  $L_3$  away from the base, as shown in Figure 22.

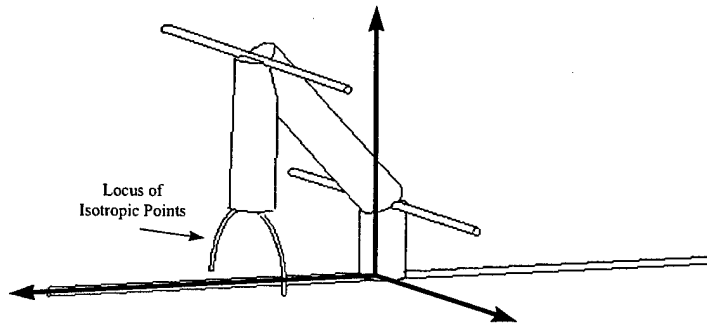


Figure 22: Locus of Isotropic Points

### 6.2.3 Actual Link Lengths

The actual link lengths were chosen to optimize the manipulation of a 3" diameter sphere by a circular array of three fingers, while maintaining the constraints required for isotropic points. The length of link 1 was

chosen to be small enough that the base axes are close together, but large enough that some of the isotropic points will fall on the sphere. The length of link 2 was chosen so that the overall finger size would be about twice that of a human finger. This size is big enough for cables and pulleys to fit inside the finger, but small enough to be able to easily manipulate objects about the size of the sphere. The length of link 3 is constrained by the isotropic point requirements. These lengths are tabulated in Table 2.

Link 1	Link 2	Link 3
1.38"	3.25"	2.30"

**Table 2: Finger Link Lengths**

### **6.3 Drive Assembly**

The drive assembly (shown in Figure 23) is located beneath the finger links and contains the three actuators, sensors, and compliant elements. The motors are not located directly on the finger links because their size and weight cannot possibly be added to the links without dramatically deteriorating performance. Because the motors are removed from the finger joints, a cable and pulley system was used to transmit power to the joints. This system is discussed in Chapter 6.4.

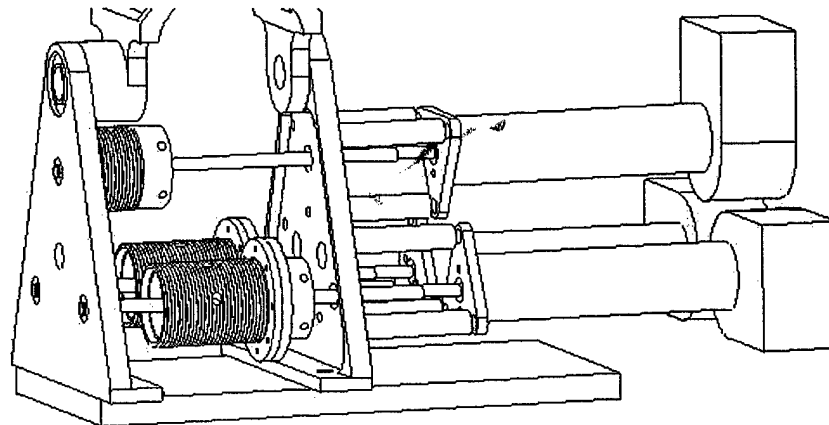


**Figure 23: Drive Assembly**

The three actuators in the drive mechanism are attached to long drive shafts with Helical Products flexible couplings, which increase the allowable shaft alignment tolerances. The compliant elements are clamped to the drive shaft, and cables that transmit power to the links are attached to the compliant elements.

Since link 1 is at the base of the finger and its axis of motion is inertially fixed, a motor can be placed immediately below the link and the cable transmission shown in Figure 24 can be used. This type of cable drive has cylindrical capstans that are tangent to one another, which minimizes friction because bearing loads are small and idler pulleys are unneeded. The cable begins on the inside of the driven capstan, and

travels through a small hole to the outside of the capstan. It then passes tangentially to the threaded drive capstan where several complete wraps are made to prevent slippage. Next, the cable passes tangentially back to the driven capstan, and again travels through a small hole to the inside of the capstan. Tensioning is accomplished by terminating the cable at the head of a hollow screw that is threaded into the mouth of the driven capstan. The screw is turned counterclockwise until the desired tension is reached. However, the maximum amount of cable that can be pulled by this mechanism is slightly less than the length of the screw (about  $\frac{1}{2}$ "); therefore, excess cable should be virtually eliminated when terminating the cable.

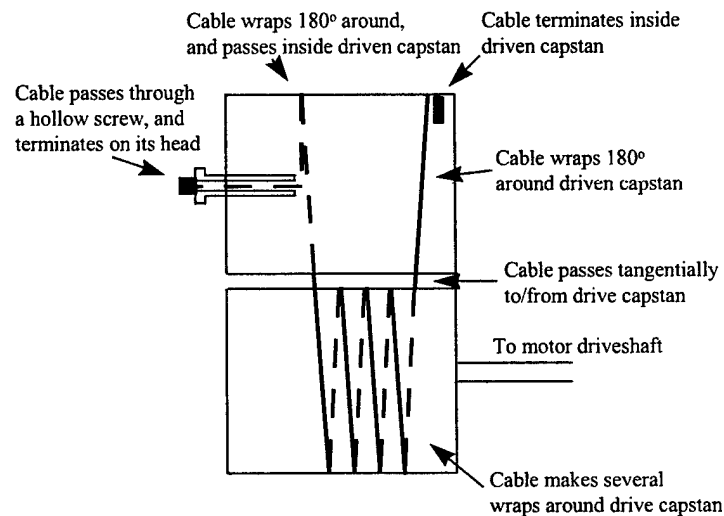


**Figure 24: Compliant Element 1 Cable Transmission and Tensioning**

This drive mechanism cannot be used for the remaining two joints since they are further away from the base and their axes of motion rotate about the previous axes. Instead, cables are simply routed from the compliant elements, to idler pulleys, and finally to the distal links. Therefore, the motor locations are arbitrary, as long as the compliant elements are aligned with the cable routing pulleys. In this design, the two motors are placed below the first, creating a triangular drive assembly. Two cables are routed in opposite directions from each compliant element to each link. Two cables were used instead of just one to eliminate the possibility of cable slippage, since each of the two cables terminates on both the compliant element and the link. The cable is tensioned at the compliant element. This end of the cable wraps around the threaded portion of the compliant element, passes through its center, and finally terminates on the head of a screw that threads into the compliant element. The direction in which the cable wraps around the capstan should be carefully chosen to avoid rubbing of the cable as the capstan rotates. The cable tensioning mechanism is similar to that used on the first axis; however, since two cables must be tensioned on each drive capstan, the hollow screws thread into the sides of the capstan instead of into the mouth, as shown in Figure 25.

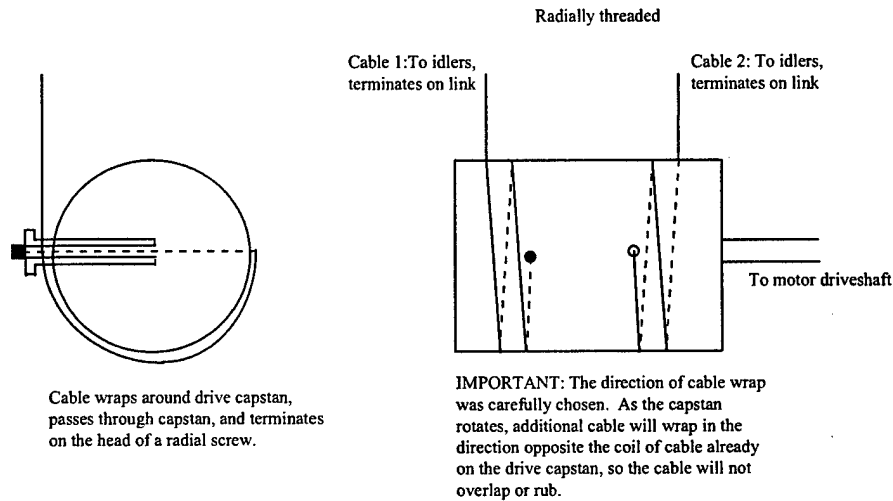
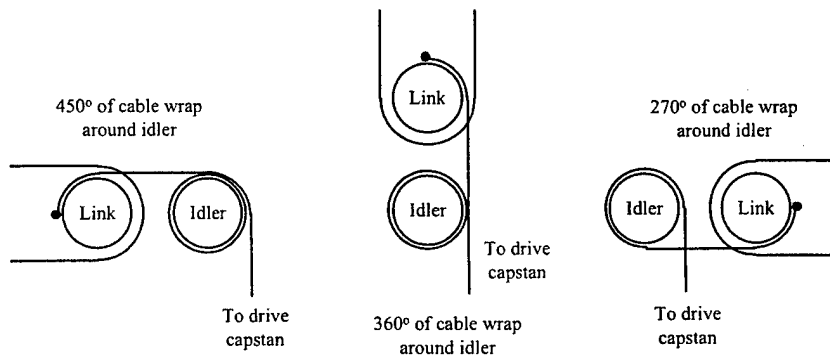


Figure 25: Compliant Element 2 and 3 Cable Termination and Tensioning

## 6.4 Cable-Pulley System

A system of steel, Sava 2024 cables and aluminum pulleys is used to transmit torque from the lower two compliant elements to the two distal joints. Since the cables must always be aligned with the compliant elements and links, idlers must be used on each joint axis to route the cables. To minimize the number of idlers and the complexity of design and assembly, only one pulley is used for each routing stage for each cable. The first stage is on the first joint axis and uses four idlers to route two cables each to the second and third joints. The second stage is on the second joint axis and requires only two idlers to route two cables to the third joint. The two cables that are routed to each joint are wrapped around the idlers and links in opposite directions, so that opposite motor rotations induce finger rotations in opposite directions. Furthermore, since the cables must remain in contact with the idlers for the entire range of motion, the cables must make an “alpha loop” around each idler pulley, as shown in Figure 26. As the previous link rotates, the “alpha loop” ranges from slightly less than one complete wrap to slightly more than one complete wrap, and is exactly one complete wrap when the link is in the middle of its rotation.



**Figure 26: “Alpha Loop” Around Idler Pulley**

Because cables and idlers are used to transmit torque, the joint axes are cross-coupled with the motors. Moving a single joint causes cables to wrap or unwrap around the idlers on that joint axis, causing a torque to be applied to the joints that are serviced by those idlers. Therefore, applying current to a single motor can generate torque on all of the joints. However, this coupling can be represented as a constant transformation matrix that can be determined off-line and accounted for in software, so the added complexity is minimal.

## **6.5 Finger Links**

The three finger links are composed of a “knuckle” at the base of the finger, and two finger “digits” attached to the base. Link 1, the knuckle, was designed with a cylindrical end section for accepting cables from its corresponding compliant element, an axis for idler pulleys to route cables for the two distal links, and an axis for link 2. Links 2 and 3, the two digit links, incorporate a taper design in which the diameter of the links decrease toward the fingertip, since link 2 requires more space for cables and pulleys than link 3. Finally, a detachable fingertip was attached to the end of the third link, so that assorted tips could be used without re-cabling the mechanism.

The design of link 1 is shown in Figure 27. At one end of the link is a short, circular section about which the first drive cable is wrapped and tensioned. At the other end of the link are the idler pulleys for cable routing, which are directly below the axis for link 2. The rounded shape of the lower section is required so that contact is not made with the compliant element as the link rotates through its range of motion. Similarly, much of the sides of the link is cut away to maintain clearance with the other drive cables.

**Figure 27: Link 1, the “knuckle”**

The final two links are tapered cylinder designs and are depicted in Figure 28. Each link is machined as two separate halves, split along the length of the link, so that a pulley can be integrated into the link. The two halves are pressed together to form the complete link. Drive cables wrap and then terminate on the

integral pulley so that pulling the cable rotates the link. A cable terminates on the integral pulley on each side of the link, each wrapped in opposite directions so that both directions of rotation are actuated.

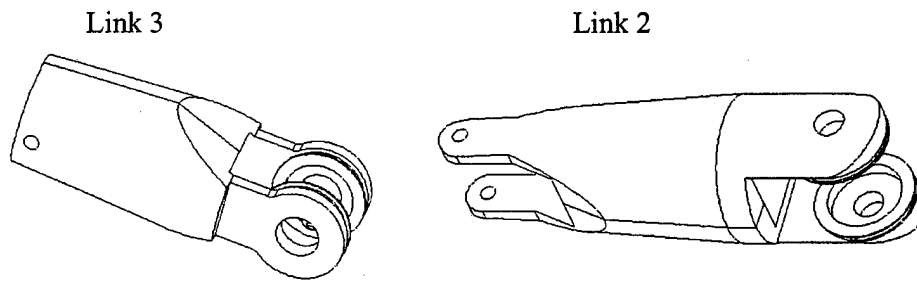


**Figure 28: Link 2 and Link 3, the “digits”**

The fingertip is simply an extension of the final link, with a short steel shaft protruding from the back. This shaft slides into a mating hole in the last finger link and is locked in place with a setscrew. This method of attachment is purposely identical to that on the Salisbury Hand, so that existing fingertips can be used on the new fingers. In this construction, a ball-ended tip was made out of low durometer polyurethane so that it will deform slightly on contact. This allows the tip to support rotational loads about the line of contact, as well as translational loads in the plane of contact, satisfying the “soft contact” model.

## **6.6 Actuation**

The finger joints are actuated by three Maxon RE016,039 DC motors with 84.3:1 gear reductions and 24 volt supply. These motors provide excellent continuous torque (8.8 mNm) and stall torque (17.6 mNm) in an extremely small package (16mm diameter, 40mm long). The gear boxes, also by Maxon, are three-stage, planetary reductions with 73% efficiency and are integrated with the motors at the time of purchase. The gearheads have the same diameter as the motors and extend the total actuator length by 23mm. The peak actuator output with the gearhead is 540 mNm continuous and 1080 mNm stall, although the gearhead is only rated for 300 mNm. However, the compliant element essentially filters impulse loads, as discussed in Chapter 3.2, so larger torques can be applied without damaging the gearhead. In fact, a test apparatus was constructed and extremely large impulse loads were applied to the actuator through the compliant element without damaging the gearhead at all.

The motors are powered by a SensAble Technologies Power Amplifier Box, which contains three Copley Controls Corp. PWM current amplifiers, along with the required control circuitry. The box is connected to the computer with a SensAble Technologies PC Interface Card. The box uses a 12-bit D/A converter to transform a digital current command to an analog signal, which is then input to the Copley amplifiers. The amplifiers were modified from their default configuration to change the peak output current from 12 amps to 1.5 amps, since the motor current at stall is only .5 amps. This change allows 8 times better current

resolution. In the future, the current limit can be changed to .5 amps, which will provide even better resolution and protect the motors from accidental current overload.

## **6.7 Instrumentation**

Two types of sensors were used in the compliant finger: optical encoders and potentiometers. An encoder was mounted to the back of the each motor and was used to measure motor position and velocity. The encoder output was monitored with encoder chips on the SensAble Technologies PC Interface Card. The potentiometers provided torque feedback to the controller. One potentiometer was mounted on each compliant element and measured the spring deflection, which is directly related to torque. A Computer Boards DAS08-AOH 12-bit A/D board was used to read the potentiometer output.

The encoders are Hewlett Packard HEDM series incremental encoders with 500 lines/rev resolution, and come in a snap-on package that measures 1.18" wide, 1.62" tall, and .70" thick. Although the encoders are quite large compared to the motors, they deliver the required resolution in the smallest package currently available. Before using these encoders on the finger, a 1.5k $\Omega$  pull-up resistor should be installed to improve the rise time of the output pulses and prevent the encoder circuitry from missing steps.

The potentiometers are Midori America Corp. CP2U-TX magneto-resistive pots and are described in Chapter 4.2, which discusses the design of the compliant elements.

## **7 FINGER CONTROL AND PERFORMANCE**

The torque control architecture developed for the single-axis compliant actuator test stand was applied to the three-axis finger to study the overall performance of the finger. Three of these controllers were implemented in parallel, along with additional control layers and transformations to account for fingertip trajectory planning, desired joint torque determination, gravity compensation, and coupling between the motors and joints. Several experiments were performed to evaluate the performance of the controller and the effectiveness of nonlinear compliance for fingertip force control.

### **7.1 Three-Axis Controller**

A schematic diagram of the three-axis control system is shown in Figure 29. The basis for this control system is the single axis motor torque controller described in Chapter 5.2. Three single axis controllers were implemented in parallel, one for each of the three actuators on the finger. The gains of the controller were modified from the single axis case, since the inertia of the finger links is much different than the inertia in the single axis test stand. Furthermore, the gains were also different among the three parallel controller branches because of the different inertias seen by each actuator.



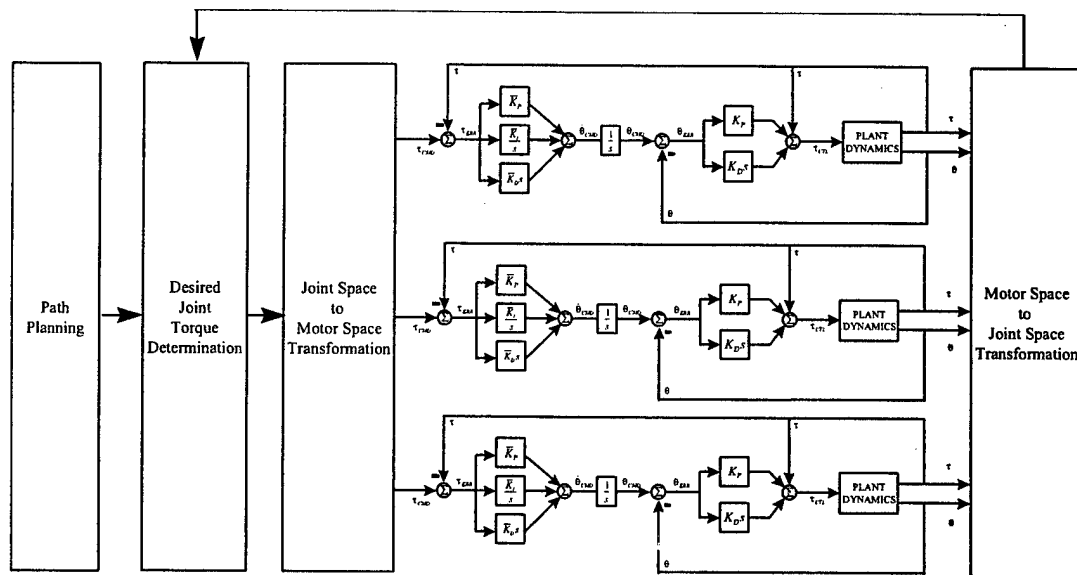


Figure 29: Schematic of Three-Axis Control System

The transformations between joint and motor space at either side of the controller are an artifact of the coupling between the motors and links caused by the cable and pulley transmissions. Tension in a single cable and rotation about a single joint can induce tension and motion about the other joint axes. Therefore, motor motion and torque is not equal to joint motion and torque. And, since the joint variables determine fingertip motion and force, and since only the joint variables can be measured, the transformations are needed. This transformation is simply a function of the radii of the many pulleys used in the transmission. Since the pulley radii are constant, the transformation is also constant and can be determined off line.

The next control layer that was added involves determining the desired or commanded joint torque based on the joint positions and the current torque. Two separate strategies were used to calculate the commanded joint torque, and experiments were performed with each. The first method involves workspace control, where a commanded fingertip force is computed from the fingertip position and velocity errors and PD gains. This is the mathematical equivalent to stretching a “virtual spring and damper” between the desired endpoint and the fingertip. The force in the virtual spring is the commanded fingertip force. This commanded fingertip force can then be related to the commanded joint torques through the transpose of the jacobian matrix ( $\tau = J^T F$ ). The advantage of this technique is that inverse kinematics is not required; however, mathematical singularities are introduced by the jacobian matrix.

The second method involves computing the commanded joint torque by applying PD gains to the joint position and velocity errors. In this case, the commanded joint angles are determined from the commanded finger position through inverse kinematics. The advantage of this method is that no mathematical

singularities are introduced, but more computation is required. A closed-form solution to the inverse kinematics problem was solved using geometry and trigonometric identities, and is shown in Equation 6.

$$\begin{aligned}\theta_1 &= \tan^{-1}\left(-\frac{y}{z}\right) \\ \theta_2 &= \tan^{-1}\left(\frac{x}{z \cos \theta_1 - y \sin \theta_1 - L_1}\right) \pm \cos^{-1}\left(\frac{r^2 + L_2^2 - L_3^2}{2L_2 r}\right) \\ \theta_3 &= \mp \left( \pi - \cos^{-1}\left(\frac{L_2^2 + L_3^2 - r^2}{2L_2 L_3}\right) \right) \\ \text{where } r &= x^2 + (y + L_1 \sin \theta_1)^2 + (z - L_1 \cos \theta_1)^2 \\ \text{and the fingertip position is } &(x, y, z)\end{aligned}$$

#### Equation 6: Inverse Kinematics Equations

The final additional layer involves very basic path planning. In the experiments conducted here, simple mathematical fingertip trajectories were commanded, such as sinusoids and straight lines. However, more complex path planning algorithms could be used without affecting the function of the control system.

Gravity compensation torques were added to the commanded joint torques computed as described above. These torques are calculated from the joint angles, finger kinematics, and link mass properties to be exactly equal and opposite to the joint torques caused by the weight of the links. The equations used to determine the gravity compensation torque are shown in Equation 7.

$$\begin{aligned}\tau_1 &= M_1 g L_{cm1,x} \sin \theta_1 + M_2 g (L_1 + L_{cm2} \cos \theta_2) \sin \theta_1 + M_3 g (L_1 + L_2 \cos \theta_2 + L_{cm3} \cos(\theta_2 + \theta_3)) \sin \theta_1 \\ \tau_2 &= M_2 g L_{cm2} \cos \theta_1 \sin \theta_2 + M_3 g (L_2 + L_{cm3} \cos \theta_3) \cos \theta_1 \sin \theta_2 + M_3 g L_{cm3} \cos \theta_1 \cos \theta_2 \sin \theta_3 \\ \tau_3 &= M_3 g L_{cm3} \cos \theta_1 \sin(\theta_2 + \theta_3)\end{aligned}$$

#### Equation 7: Calculation of Gravity Compensation Torque

### 7.2 Controller Performance

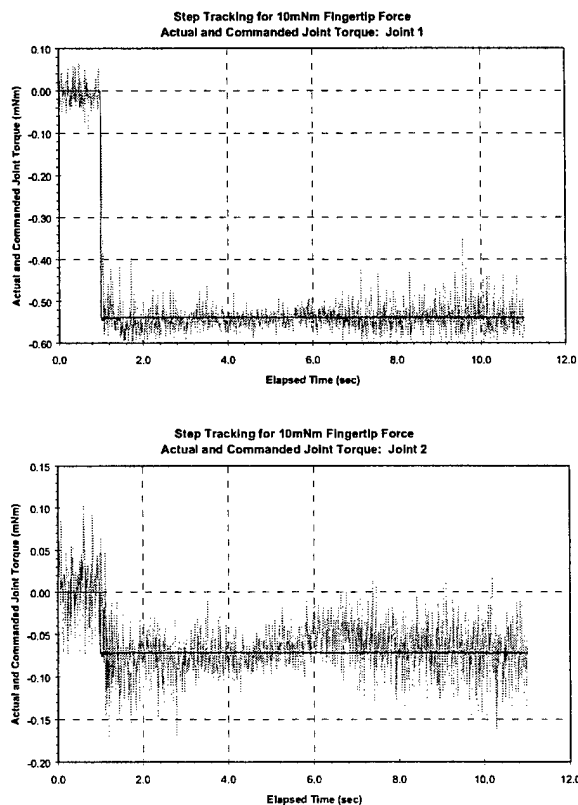
Several experiments were performed to evaluate the effectiveness of the controller described above in various tasks. Unfortunately, the experiments showed that the complete control system, which includes the three motor torque controllers and all additional control layers, cannot stably or accurately control fingertip trajectories or force. *However*, it was shown that the torque control strategy developed in Chapter 5.2 is applicable to more complex systems, and *can* be used for stable and accurate control of actuator output torque.

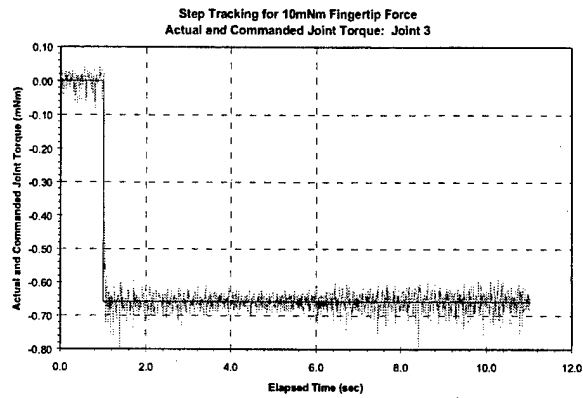
Tests involving trajectory tracking and fingertip force control using this three axis controller were not successful. The algorithms developed above were not capable of stable or accurate fingertip position or

force control. Instability problems arose when the finger was near the upright position due to gravitational forces. In addition, precise trajectory tracking was not realized for reasons that were not determined due to time and scope constraints. Further research is required to develop a controller capable of these tasks.

However, tests showed that the controller can track commanded actuator torques extremely well, despite the effects of actuator coupling, variable inertia, etc. The instabilities encountered in other experiments were caused because the algorithms that compute the commanded joint torques were not suitable. To show this, the following experiments were performed.

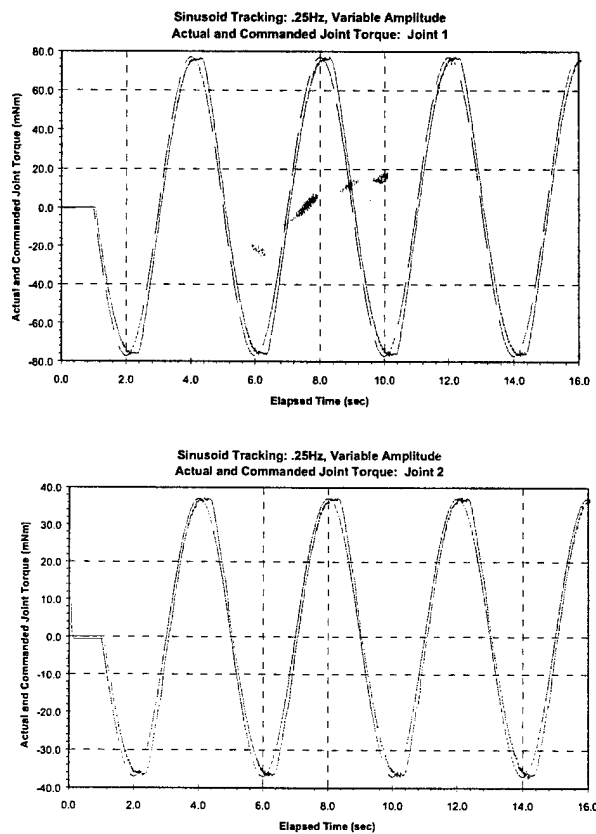
First, the fingertip was locked in place and a fingertip force of 10mNm was commanded. Since the finger was not allowed to move, the outer control layers had no effect and the instabilities were not encountered. Instead, the joint torques that produce the desired fingertip force were computed, and the appropriate motor torques were commanded. Since the desired fingertip force is small, the required joint torques are extremely small (less than 1.0mNm). The three motor torque control loops were able to track these torques as shown in Figure 30.





**Figure 30: Joint Torque Step Tacking w/Fixed Fingertip**

The next experiment was performed with sinusoidally varying commanded joint torques, much larger commanded torque levels that vary among the three joint axes, and also a fixed finger position. The plots in Figure 31 again show extremely accurate joint torque control.



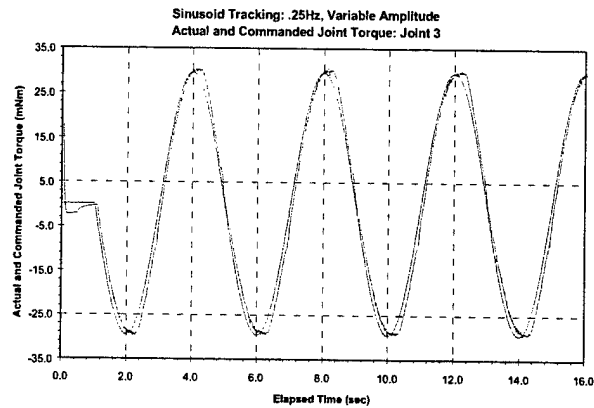
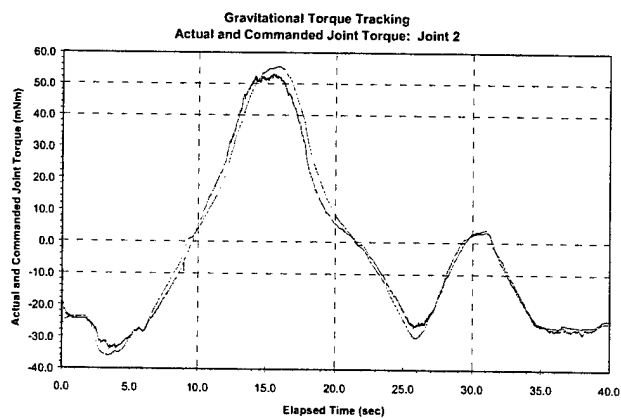
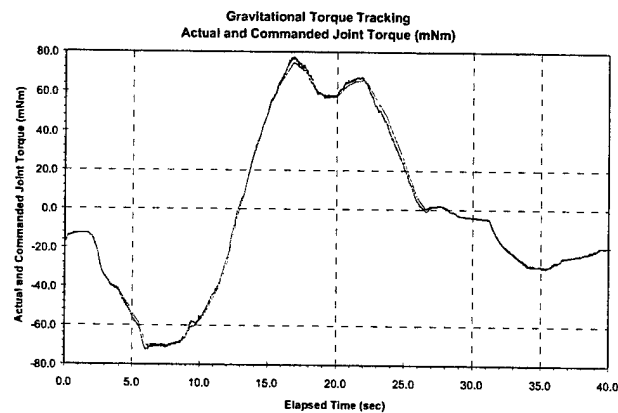


Figure 31: Joint Torque Sinusoid Tracking w/Fixed Fingertip

The final test that was performed involved tracking the commanded gravitational compensation torque while the fingertip was manually moved through the workspace. This test also involved fairly large commanded joint torques (50-90mNm), but it also required tracking of a complex joint torque profile. Again, the test showed that the controller was quite adept at controlling motor and joint torque given a command. The graphs in Figure 32 illustrate this conclusion.



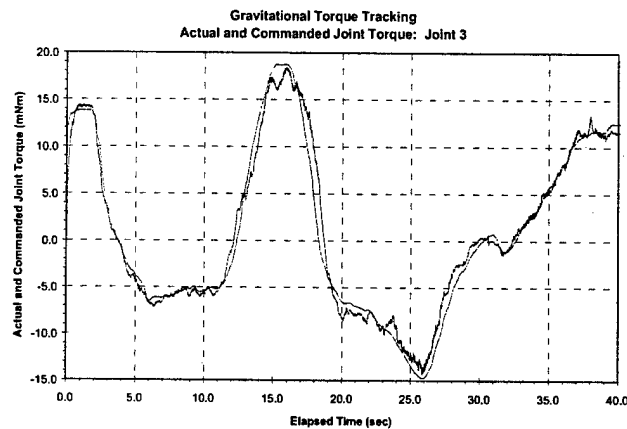
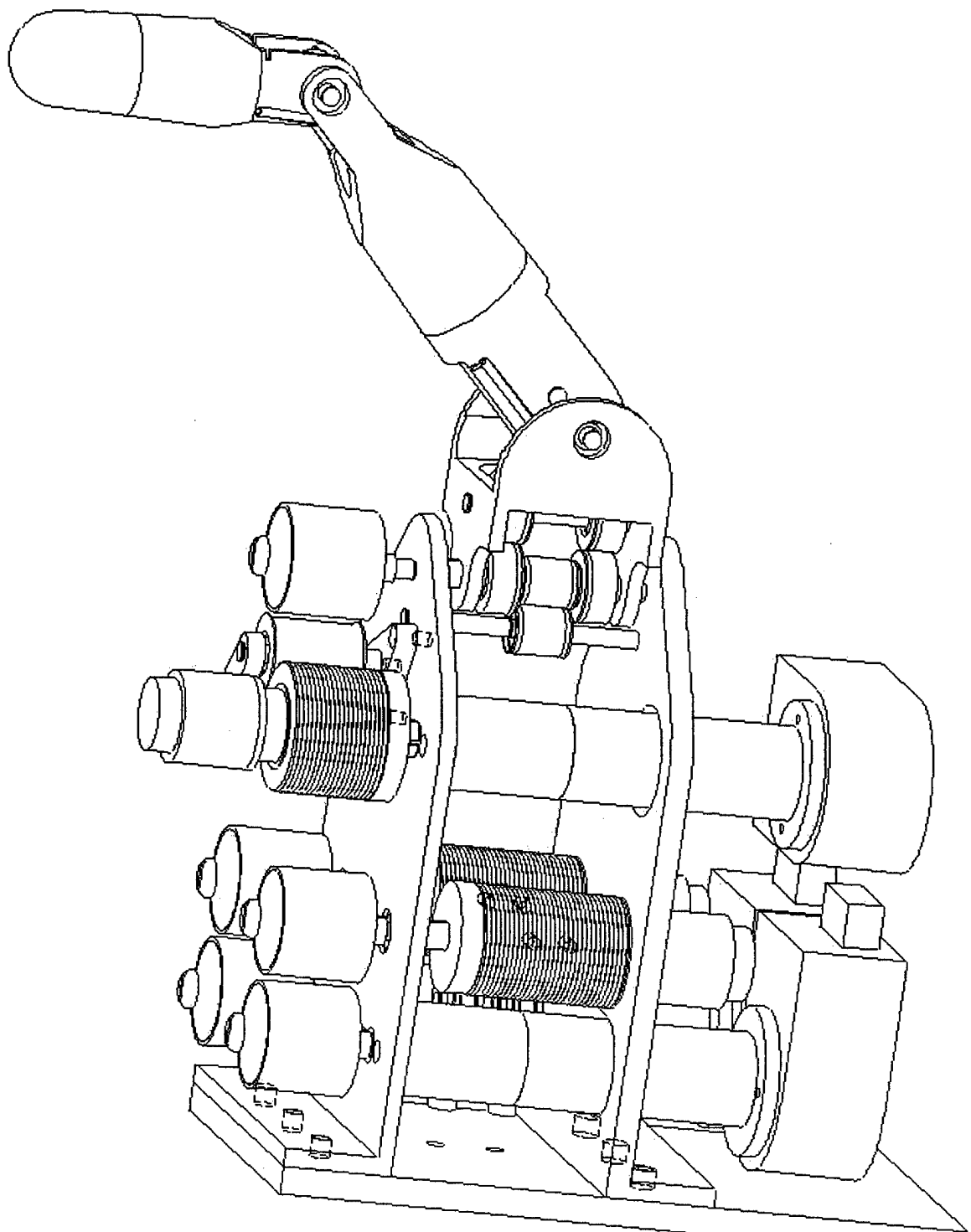


Figure 32: Gravitational Torque Tracking While Finger is Manually Moved

## 8 NEW FINGER DESIGN

After building, controlling, and using the compliant finger, several desirable characteristics of the finger were recognized, and many possible improvements in the mechanical design became apparent. The desirable traits were carried over to the new finger design, which is shown in Figure 33. The redesigned finger maintains the same kinematics and general appearance. There are still three links, and the outer two links are tapered. Also, although the link lengths are different, their proportion remains the same to ensure that isotropic points still exist. Furthermore, the drive mechanism and compliant elements are functionally unchanged.



**Figure 33: New Finger Design**

Despite the many similarities, several changes were implemented in the second generation design to correct drawbacks of the original design. First, the drive assembly was redesigned to make it shorter, narrower, and more compact, while eliminating the flexible couplings that joined the motor output shafts to the drive shafts. Furthermore, the cable-pulley system that transmitted power from the motors to the finger joints was redesigned to minimize friction generated by cable rubbing and to implement a simpler and more effective method of cable tensioning. Next, the weight and aspect ratios of the finger links were decreased because it was determined that lighter finger links can increase the torque resolution of the controller, and that longer, narrower fingers are better suited for dexterous manipulation. Finally, individual components throughout the system were redesigned to simplify machining and minimize manufacturing costs.

Appendix A presents all the hardware and machined parts, including machine drawings, that compose the new finger design.

### **8.1 The Drive Assembly**

One of the main drawbacks of the original design was that the drive assembly was quite large relative to the size of the actual finger links (see Figure 20). In fact, the fully-extended finger was only 5.5" long and 1.25" in diameter at its widest point, while the drive mechanism was 3.5" inches tall, 3.0" inches wide, and 7.5" inches long with the three motor/encoder pairs protruding over 4.5" inches behind the finger. The large relative width limits the proximity at which multiple fingers can be placed; that is, the sides of the drive mechanism will interfere if the fingers are moved too close together. Furthermore, the length and the protruding motors cause a configuration of multiple fingers to occupy an extremely large space, making it difficult to mount a multi-fingered hand onto a robot arm or another platform.

Also, the flexible couplings used in the original drive assembly to attach the drive shafts to the motor output shafts were unreliable, expensive, and added about 1" to the overall length of the drive assembly. These clamp-style couplings, purchased from Helical Products Corporation, would slip if not clamped extremely tightly; however, the tiny M2.0 clamp screws were easily stripped or even broken, making it difficult to achieve the required grip.

In the new design, the size of the drive assembly was reduced in three ways: (1) placing motors on a separate axis from their corresponding compliant elements, (2) eliminating the flexible couplings, and (3) moving the motors closer together. Figure 34 shows front and side views of the lower drive assembly of the new design. Comparison with Figure 20 shows the reduction in size.



**Figure 34: Front and Side Views of Lower Actuator in New Design**

First, the two lower motors were moved to a separate axis from the compliant elements that they drive, which allows the motors to be placed directly beneath the finger links and drastically decreases the length of the drive assembly and the amount by which the motor/encoder pairs protrude behind the finger. The major constraint on this part of the drive assembly design is the position of the compliant elements, which must be directly beneath the first finger link for cabling purposes. In the previous design, the motors were directly attached to the shaft running through the compliant elements, so they were forced to extend behind the finger. In the new design, the motors are beneath the finger on a separate axis and power the compliant elements through an additional cable drive, which consists of tangent capstans on both the motor and compliant element axes and a steel cable that runs between them. In addition, the Helical Products flexible couplings were eliminated because the cable capstan can be attached directly to the motor output shaft, making it unnecessary to mount a long drive shaft to the motor.

Although this modification shortens the overall length of the drive assembly from about 9" to 5", the addition of more axes and cable drives increases the complexity and overall height of the assembly. But, the cable mechanism connecting the motors to the compliant element axes is quite simple and efficient (two tangent capstans and a cable) so the added complexity is small. Furthermore, the height of the assembly is virtually inconsequential since it does not affect the performance of the finger or the geometry of a multi-fingered hand; therefore, this height increase is acceptable.

## 8.2 Cable/Pulley System

Two additional drawbacks of the original finger stemmed from the design of the cable and pulley system that provides torque to the two pitch axes of rotation. Cable rubbing added friction to the system, and an ineffective cable tensioning mechanism left slack in some of the drive cables. Several design changes were implemented to correct for these problems.

### 8.2.1 Cable rubbing

The first problem is friction generated by the steel cables rubbing against themselves as they pass over the idler pulleys. As discussed in Chapter 6.4, in the original design, the cable must execute at least one complete loop around the idlers in order to maintain contact for the entire range of motion. This “alpha loop”, shown in Figure 26, is a consequence of the original design, which used only one pulley for each cable and routing stage. The complete loop causes the cable to rub against itself as the finger is rotated, thereby adding friction to the system. Since this friction occurs after the compliant element, it can not be eliminated by feedback control, unlike the gearhead friction. Therefore, this is a significant source of friction and could compromise torque control accuracy and resolution.

The problem was solved in the new version by doubling the number of idler pulleys so that two pulleys are used for each cable and routing stage. Doubling the number of idlers eliminates the need for looping the cable around the pulley so the cable no longer rubs against itself, as shown in Figure 35. Furthermore, the additional pulleys were added without significantly affecting the overall size of any components, although the assembly and cabling complexity was slightly increased.

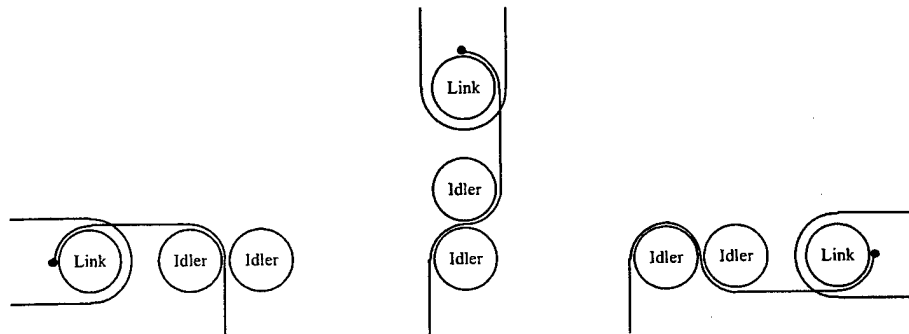


**Figure 35: Cable Routing Over Double Idler Pulleys**

Although this design eliminates a major source of friction, it introduces a new problem involving the range of motion of the joints. The full range of motion can only be achieved if the spacing between the two pulleys is maintained within extremely tight tolerances. The reason for this requirement is that the cable must be in contact with both pulleys throughout the entire range of motion, and this condition will not be met if the spacing isn't perfect. Instead, the cable will lose contact with the first pulley before the full

motion is reached, as shown in Figure 36. Equation 8, derived using basic geometry, relates the range of motion to the space between the pulleys:

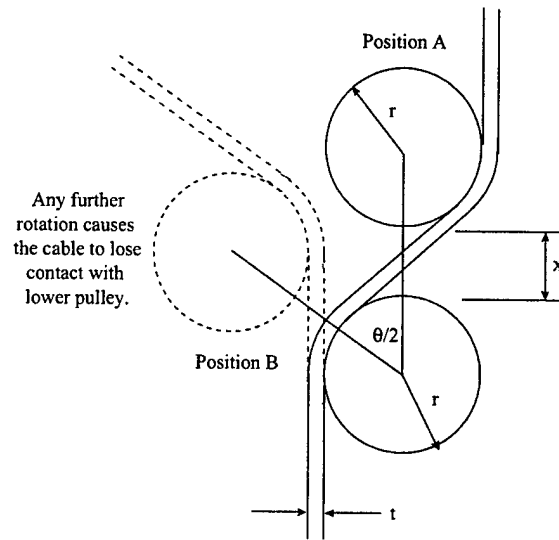


**Figure 36: Cable Loses Contact With First Pulley**

$$\theta = 2 \sin^{-1} \left( \frac{2r + t}{2r + x} \right), \text{ where the variables are defined in Figure 36}$$

#### **Equation 8: Relation Between Range-of-Motion and Pulley Spacing**

It was determined that the tolerance on the spacing of the two pulleys that can be reasonably manufactured on conventional machine tools is about  $\begin{smallmatrix} +.002 \\ -.000 \end{smallmatrix}$ . This results in a range of motion of  $\pm 84^\circ$ , which is slightly lower than in the original design, but does not significantly affect the overall workspace of the fingertip.

### **8.2.2 Cable Tensioning**

The second problem is that the cable tensioning system used on the lower two motors in the original design is ineffective. In the old system, tensioning was accomplished by terminating the cables on the head of a screw that threads into the side of the compliant element. However, the cable wraps around the compliant element several times before terminating. These wraps create tremendous friction between the cable and compliant element; therefore, tension caused by turning the screw is not effectively transmitted to the section of cable between the compliant element and the finger link. Instead, the part of the cable that needs to be tensioned remains slack, and the short section between the screw and the compliant element becomes extremely tight.

Several design changes were made to implement a much more effective cable tensioning mechanism. First, only one cable was used per link instead of two, since the failure of the original design shows that friction alone is enough to prevent cable slippage and the additional cable isn't necessary. This change removes

many design constraints since fewer tensioning mechanisms are required in the same available space. In addition, the tensioning mechanism was redesigned to pull directly on the section of cable that requires tensioning. In this new design, the cable path is almost the same as before, except that now the cable wraps around an additional idler immediately after leaving the compliant element (see Figure 37). Lowering the idler, which is done by turning a screw, pulls directly on the section of cable between the capstan and finger link, thereby tensioning the cable. Furthermore, the amount of cable that can be pulled in this design is twice the travel of the tensioning screw; therefore, about 1.5" of cable slack can be removed compared to only about .4" in the original design.

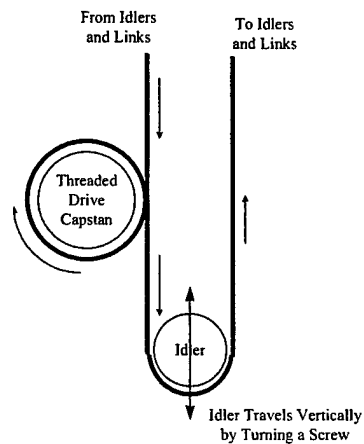


**Figure 37: Cable Tensioning in the New Finger Design**

Another benefit of this tensioning system is that the screws and cable crimp terminations that protruded from the sides of the compliant elements in the old design are eliminated in the new design. Therefore, the motor/encoder pairs can be moved closer together to minimize the width of the drive assembly. But, since the encoders are so large relative to the motors, their size governs the minimum distance between motors, and hence the overall assembly width.

### **8.3 Finger Links**

In the new design, the weight of the finger links was decreased to improve contact sensing and absolute resolution of torque sensing and control. Lighter links cause less weight-induced deflection of the compliant element, allowing better resolution for contact-induced deflections as discussed in Chapter 5.3.2. The weight of the links was reduced by changing from a two-piece to a one-piece design, decreasing the wall thickness of the finger, and decreasing the width of the finger. The old and new versions of the second finger link are shown in Figure 38 to illustrate these changes. The change from two-piece to one-piece design also requires the termination of the drive cables on the link itself instead of on the final pulley, since this pulley cannot be integrated into the link as with the two piece version. However, the machining of the

one-piece design is much simpler and cheaper, since it requires fewer parts, simpler cuts, and lower tolerances.

Although the design is different, the new finger links will share several aesthetic traits with their predecessors, including the tapered outer wall. To reduce weight even further, the thickness of this outer wall was made uniform and reduced to .100" by also tapering the inner hole running through the length of the finger using an off-the-shelf tapered end mill. In the previous design, the inner hole was not tapered, so the wall thickness was small at one end (.120") and very large at the other (.190"). Although the wall in the new design is still quite thick, this thickness is necessary to house a pair of ball bearings at one end of the link. Finally, the fingers were made narrower to reduce weight further still. The total weight reduction in the three finger links about 35%.

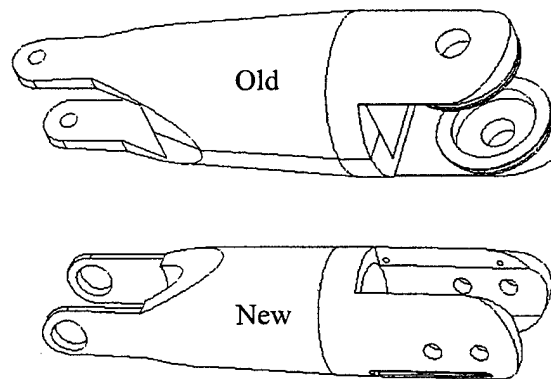


**Figure 38: Old and New Versions of Link 2**

The width reduction of the fingers serves a second purpose in addition to lowering the weight. It has been suggested that longer, narrower fingers are better suited for dexterous manipulation because the finger surfaces are less likely to interfere with the motion and positioning of the fingertips or the manipulated object. Therefore, the better aspect ratio should help to facilitate dexterous grasping.

#### **8.4 Simplified Machining**

Since one of the main goals of this project was to create an inexpensive finger, many components were redesigned to minimize machining costs. For example, the finger links discussed in Chapter 8.3 were changed to a simpler, one-piece design rather than two pieces that are pressed together. This change greatly simplifies the machining and reduces the required tolerances. In addition, since it's cheaper to make several copies of the same part rather than several slightly different parts, the number of unique parts was lowered and the number of copies of many parts was increased. Finally, the method by which components are

clamped to a shaft was changed from a custom mechanism that clamps down onto a flat in the shaft, to an off-the-shelf hub-style clamp that does not require a flat on the shaft. These changes should combine to reduce the machining costs by about 20%, from \$2500 to around \$2000 per finger.

## 9 SUMMARY

In this work, a modular, compliant robot finger was developed that has a large dynamic range, a constant percentage force resolution, and is intrinsically force controllable, inexpensive, and compact. In addition, a basic control structure for fingertip force control was devised. These modular fingers can be used as the basis for a re-configurable multi-fingered hand to be used for grasping and grasp gait experiments on objects with a wide range of sizes and shapes. It is hoped that further research with this hand will lead to the development of even more capable, compact, and inexpensive hands that will eventually achieve success outside the research environment.

The finger was designed with three joints and three degrees of freedom. The kinematics are similar to that of a human finger; namely, nearly intersecting roll and pitch axes at the base, and an additional pitch axis on the distal link. The joints were actuated by three DC motors that were separated from the links to reduce the mass and inertia of the finger. The actuators were located beneath the finger, and a system of pulleys and steel cables was used to transmit torque to the joints.

Traditionally, high performance systems have been designed to be as stiff as possible; however, this finger was intentionally designed with intrinsic mechanical compliance as a means of improving force control performance. The compliance was implemented through the use of exponentially stiffening springs located between the actuators and finger joints. Force control through this compliance is performed by controlling the deflection of the spring; therefore, compliance transforms the force control problem into one of position control, which improves force controllability and simplifies control. Furthermore, accurate position control can be achieved with small, cheap, gear-reduced motors, so adding compliance to the system also reduces actuator costs.

The exponentially stiffening nature of the springs used in the compliant elements provides a constant percentage resolution of exerted and sensed torque and leads to enormous dynamic range and excellent contact sensing ability, performance characteristics also found in human fingers. The percentage resolution, which is the percent change in force that can be exerted or sensed, remains constant because torque is controlled by producing fixed-resolution deflections of the spring, but the torque per unit deflection increases with the torque level due to the stiffening nature of the spring. Therefore, at low torque levels, the spring is flexible and a unit deflection produces a very small change in output torque, yielding a fine absolute torque resolution. At high torque levels, the spring is stiff, so the same unit change in spring

deflection produces a much higher change in torque, yielding a coarse absolute resolution. Although the absolute resolution changes, the percent resolution remains constant, so both extremely small and very large output forces are possible and dynamic range is drastically improved. Furthermore, since fine force resolution is available at low forces, extremely small contact forces can be detected, thereby improving contact sensing ability.

The control structure used to achieve these performance improvements consisted of a high gain, high bandwidth inner motor position control loop and a lower bandwidth outer torque control loop. The outer loop applied PID gains to the torque error resulting in a commanded motor position to correct the torque error. The inner loop tracks this commanded position with a fast, stable PD controller. This structure takes advantage of the stiff, collocated motor/encoder pair to create a high bandwidth inner loop. The outer loop contains the flexibility of the compliant element, and therefore much lower gains and narrower bandwidth are achievable.

A single-axis test stand was constructed to quantify the performance improvements that exponential compliance provides. This test stand consisted of a single, collocated motor/encoder pair connected to a compliant element containing the spring mechanism and a potentiometer to measure spring deflection. Experiments with this system show that the percent resolution in torque was approximately 5%, and is exactly equal to the resolution of the potentiometer ( $.25^\circ$ ) as expected. This resolution corresponds to a dynamic range of over 1000, a factor of 30 increase over the motor alone. The bandwidth of this system was about 10 Hz, which is lower than what could be achieved without compliance. However, this decreased bandwidth should not affect the performance of the finger, since grasping and manipulation do not require rapid, high bandwidth movements.

Three of these torque control blocks were combined to form the basis for the finger control algorithm. Additional control layers were added to account for path planning, desired fingertip force calculation, and joint torque determination. However, a precise, high performance fingertip position and force control algorithm that integrates all of the required controller components was not realized. But, it was shown that the basic torque control structure used successfully on the single-axis system can also be used in the multiple-axis case, despite the cross-axis coupling and changing load torque and inertia. Additional research is required to achieve fingertip force control performance equivalent to that achieved in controlling an isolated torque on the single-axis test stand.

## References

- Ali, M.S., Kyriakopoulos, K.J., Stephanou, H.E. "The Kinematics of the Anthrobot-2 Dextrous Hand", Proceedings of the IEEE International Conference on Robotics and Automation, 1993.
- Balas, M.J. "Active Control of Flexible Systems", Proceedings of the 1977 Symposium on Dynamics and Control of Large Flexible Spacecraft, Blacksburg, VA, 1977.
- Brooks, R.A., Stein, L.A. "Building Brains for Bodies", Autonomous Robots, (1:1), 1994.
- Brooks, T.L. "Telerobotic Response Requirements", Proceedings of the IEEE International Conference on Systems, Man, and Cybernetics, Los Angeles, 1990.
- Cannon, R.H., Rosenthal, D.E. "Experiments in the Control of Flexible Structures with Non-Collocated Sensors and Actuators", Journal of Guidance and Control, vol. 7, no. 5, 1984.
- Childress, D.S. "Artificial Hand Mechanisms", Mechanisms Conference and International Symposium on Gearing and Transmission, San Francisco, CA, 1972.
- Clark, F.J., Horch, K.W. "Kinesthesia", vol. I of Handbook of Perception and Human Performance - Sensory Processes and Perception, Wiley & Sons, New York, 1986.
- Crossley, F.R.E., Umholtz, F.G. "Design for a Three Fingered Hand", Mechanism and Machine Theory, Vol. 12, 1977.
- Eppinger, S., Seering, W. "Three Dynamic Problems in Robot Force Control", IEEE International Conference on Robotics and Automation, 1989.
- Fearing, R. "Simplified Grasping and Manipulation with Dextrous Robot Hands", IEEE Journal of Robotics and Automation, vol. 2 no. 4, 1986.
- Hanafusa, H. and Asada, H. "Stable Prehension by a Robot Hand with Elastic Fingers", Proceedings of the 7<sup>th</sup> ISIR, Tokyo, Oct. 1977.
- Hogan, N. "Impedance Control: An Approach to Manipulation: Part I - Theory, Part II - Implementation, Part III - Applications", Journal of Dynamic Systems, Measurement, and Control, 107:1-24, 1985.
- Hogan, N. "Co-Activation of Antagonist Muscles: Predictions and Observations", Proceedings of the Annual International Conference of the IEEE Engineering in Medicine and Biology Society, New Orleans, LA, 1988.
- Hogan, N., Colgate, E. "Stability Problems in Contact Tasks", Robotics Review, MIT Press, 1989.
- Hunter, I.W., Hollerbach, J.M., Ballantyne, J. "A Comparative Analysis of Actuator Technologies for Robotics", Robotics Review Vol. 2, MIT Press, 1991.
- Jacobsen, S.C., et al. "Development of the Utah Artificial Arm", IEEE Transactions on Biomedical Engineering, Vol. BME-29, No. 4, Apr. 1982.
- Jacobsen, S.C., Wood, J., Bigger, K., Iverson, E. "The Utah/MIT Hand: Work in Progress", International Journal of Robotics Research, 4(3):21-50, 1984.



- Jau, B.M. "Man-Equivalent Tele Presence Through a 4-Fingered Human-Like Hand System", Proceedings of the IEEE International Conference on Robotics and Automation, 1992.
- Jones, L.A. "Matching Forces: Constant Errors and Differential Thresholds", Perception, vol. 18, 1989.
- Leveroni, S., Shah, V., Salisbury, J.K. "Toward Dexterous Gaits and Hands", Proceedings of the 5<sup>th</sup> International Symposium on Experimental Robotics, Barcelona, 1997.
- Mason, M.T., Salisbury, J.K. Robot Hands and the Mechanics of Manipulation, MIT Press, Cambridge, MA, 1985.
- Massie, T.H., Salisbury, J.K. "The Phantom Haptic Interface: A Device for Probing Virtual Objects", ASME Dynamic Systems and Control, Chicago, 1994.
- Morita, T., Sugano, S. "Development of One-DOF Robot Arm Equipped with Mechanical Impedance Adjuster", IEEE-RSJ International Conference on Intelligent Robots and Systems, Pittsburgh, 1995.
- Morrell, J., Salisbury, J.K. "Parallel Coupled Actuators for High Performance Force Control: A Micro-Macro Concept", IEEE-RSJ International Conference on Intelligent Robots and Systems, Pittsburgh, 1995.
- Morrell, J., Salisbury, J.K. "In Pursuit of Dynamic Range: Using Parallel Coupled Actuators to Overcome Hardware Limitations", Proceedings of the 4<sup>th</sup> International Symposium on Experimental Robotics, 1995.
- Murray, R.M., Li, Z., Sastry S.S. A Mathematical Introduction to Robotic Manipulation, CRC Press, 1994.
- Okada, T. "Computer Control of a Multijointed Finger System for Precise Object Handling", IEEE Transactions on Systems, Man, and Cybernetics, SMC-12(3):289-299, 1982.
- Pang, X.D., Tan, H.Z., Durlach, N.I. "Manual Discrimination of Force Using Active Finger Motion", Perception and Psychophysics, vol. 49, no. 6, 1991.
- Pratt, G.A., Williamson, M.M., Dillworth, P., et al. "Stiffness Isn't Everything", Proceedings of the 4<sup>th</sup> International Symposium on Experimental Robotics, Stanford, CA, 1995.
- Pratt, G.A., Williamson, M.M. "Series Elastic Actuators", IEEE-RSJ International Conference on Intelligent Robots and Systems, Pittsburgh, 1995.
- Readman, M.C. Flexible Joint Robots, CRC Press, 1994.
- Salisbury, J.K., Craig, J. "Articulated Hands: Force Control and Kinematic Issues", International Journal of Robotics Research, 1982.
- Salisbury, J.K. "Design and Control of an Articulated Hand", Proceedings of the International Symposium on Design and Synthesis, Tokyo, July 1984.
- Salisbury, J.K., Eberman, B., Levin, M., Townsend, W. "The Design and Control of an Experimental Whole-Arm Manipulator", Proceedings of the 4<sup>th</sup> International Symposium on Robotics Research, 1989.
- Sharon, A., Hogan, N., Hardt, D. "The Macro/Micro Manipulator: An Improved Architecture for Robot Control", Robotics and Computer Integrated Manufacturing, 10(3), 1993.
- Skinner, F. "Designing a Multiple Prehension Manipulator", Journal of Mechanical Engineering, 97(9):30-37, 1975.
- Slotine, J.J., Li, W. Applied Nonlinear Control, Prentice Hall, 1990.

Srinivasan, M., Chen, J. "Human Performance in Controlling Normal Forces of Contact with Rigid Objects", ASME Dynamic Systems and Control: Advances in Robotics, Mechatronics, and Haptic Interfaces, DSC-49, 1993.

Sugano, S., Tsuto, S., Kato, I. "Force Control of the Robot Finger Joint Equipped with Mechanical Compliance Adjuster", IEEE-RSJ International Conference on Intelligent Robots and Systems, Raleigh, NC, 1992.

Tan, H.Z., Pang, X.D., Durlach, N.I. "Manual Resolution of Length, Force, and Compliance", Advances in Robotics, vol. 42, 1992.

Tan, H.Z., Srinivasan, M., Eberman, B., Cheng, B. "Human Factors for the Design of Force-Reflecting Haptic Interfaces", ASME Dynamic Systems and Control, DSC-Vol. 55-1, 1994.

Tasch, U. "A Two-DOF Manipulator with Adjustable Compliance Capabilities and Comparison with the Human Finger", Journal of Robotic Systems, 13(1), 1996.

Townsend, W.T. "The Effect of Transmission Design on the Performance of Force-Controlled Manipulators", Ph.D. Thesis, MIT Dept. of Mechanical Engineering, 1988.

Whitney, D.E., "Historical Perspective and State of the Art in Robot Force Control", International Journal of Robotics Research, vol. 6, no. 1, 1987.

## Appendix A: New Finger Components

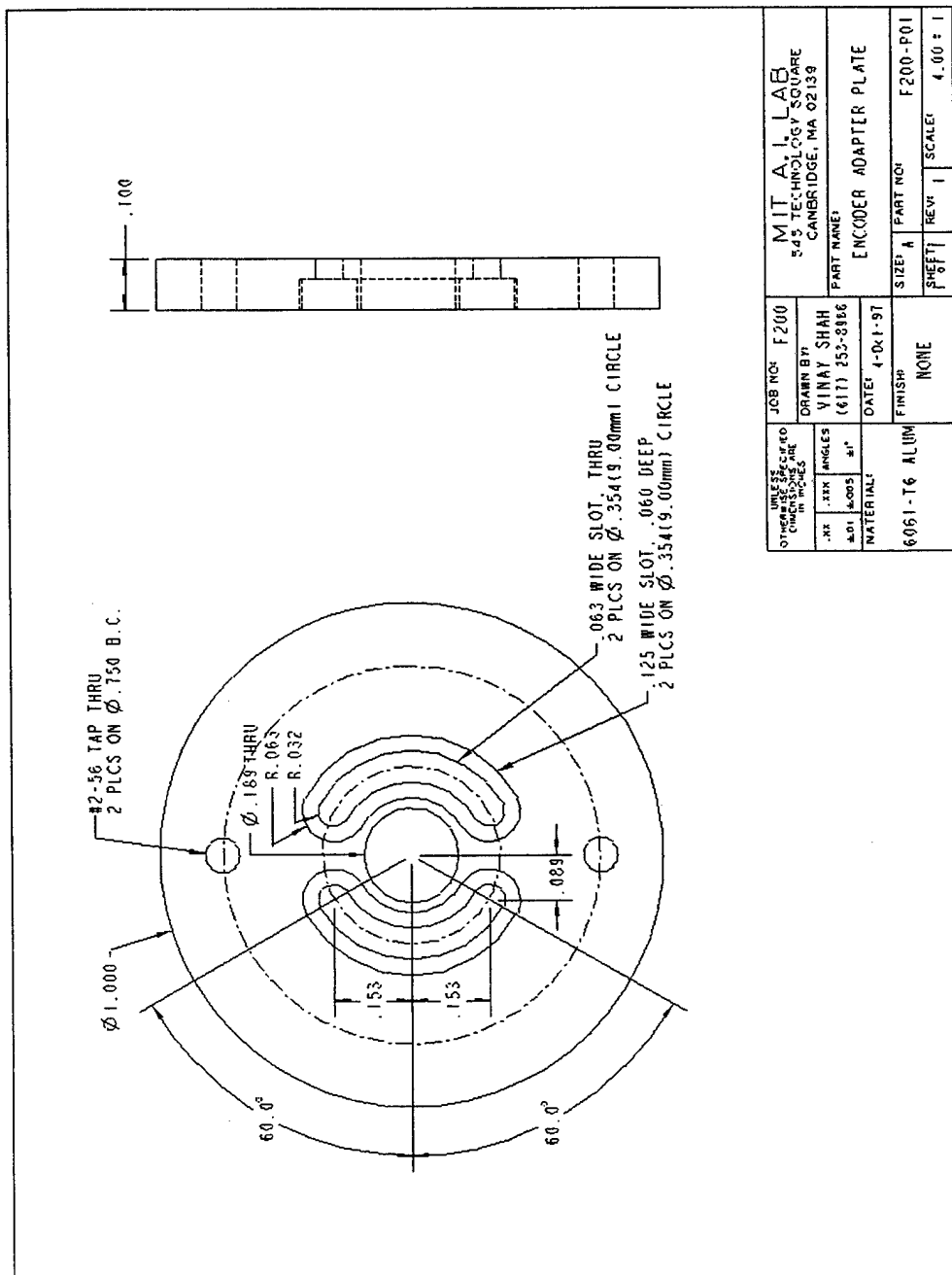
### Bill of Materials - Machined Parts

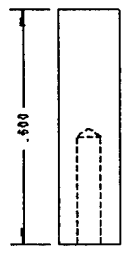
PART NUMBER	PART NAME	QUANTITY
F200-P01	ENCODER ADAPTER PLATE	3
F200-P02	ENCODER ADAPTER SHAFT	3
F200-P03	MOTOR 1 IDLER SUPPORT	1
F200-P04	MOTOR 1 IDLER SHAFT	1
F200-P05	POT FACE ADAPTER	3
F200-P06	POT SHAFT ADAPTER	3
F200-P07	FRONT PLATE	1
F200-P08	BACK PLATE	1
F200-P09	BASE	1
F200-P10	TENSIONER PLATE	3
F200-P11	TENSIONER PULLEY SUPPORT	2
F200-P12	TENSIONER SCREW	5
F200-P13	DRIVE CAPSTAN	5
F200-P14	LARGE COMPLIANT JOINT	1
F200-P15	LARGE COMPLIANT CAPSTAN	1
F200-P16	SMALL COMPLIANT JOINT	2
F200-P17	SMALL COMPLIANT CAPSTAN	2
F200-P18	LINK 1	1
F200-P19	LINK 2	1
F200-P20	LINK 3	1
F200-P21	.330 PULLEY	4
F200-P22	.490 PULLEY	4
F200-P23	LINK 2 PULLEY	2
F200-P24	LINK 3 PULLEY	2
F200-P25	MOTOR 1 IDLER PULLEY	1
F200-P26	TENSIONER PULLEY	2
F200-P27	BASE IDLER SHAFT	1
F200-P28	BOTTOM MOTOR SHAFT	2
F200-P29	LINK 1 LOWER SHAFT	1
F200-P30	LINK 2 LOWER SHAFT	2
F200-P31	LINK 2 UPPER SHAFT	1
F200-P32	LINK 3 SHAFT	1
F200-P33	TOP MOTOR SHAFT	1
F200-P34	TENSIONER SHAFT	2
F200-P35	FINGERTIP SHAFT	1
F200-P36	FINGERTIP	1
F200-P37	LINK 1 UPPER/INNER SPACER	1
F200-P38	LINK 1 UPPER/OUTER SPACER	4
F200-P39	LINK 2 LOWER SPACER	2
F200-P40	LINK 3 SPACER	1
F200-P41	MOTOR 1 IDLER SPACER	1

PAGES 67 & 68  
ARE  
MISSING  
IN  
ORIGINAL  
DOCUMENT

**Bill of Materials - Hardware**

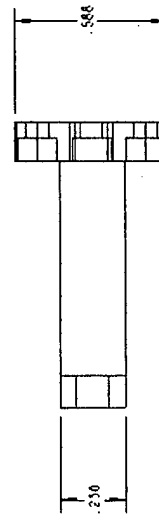
CATEGORY	PART DESCRIPTION	QUANTITY
MOTORS	MAXON RE016-039 DC MOTOR	3
ENCODERS	HEWLETT PACKARD HEDM-5500 500LPR	3
POTENTIOMETERS	MIDORI AMERICA CP2U-TX	3
BEARINGS	1/8ID, 1/4OD, SHIELDED, FLANGED BALL BEARINGS	24
	1/8ID, 1/4OD, SHIELDED, UNFLANGED BALL BEARINGS	2
	1/8ID, 1/4OD, UNSHIELDED, FLANGED BALL BEARINGS	2
	3/16ID, 3/8OD, SHIELDED, FLANGED BALL BEARINGS	1
	1/2ID, 3/4OD SHIELDED, X-THIN BALL BEARINGS	2
CABLE	SAVA 2024 UNCOATED STEEL CABLE	~4FT
	SAVA BALL-END CABLE TERMINATIONS	10
CLAMPS	.188ID, .156THICK SPLIT HUB CLAMP	8
	.250ID, .156THICK SPLIT HUB CLAMP	1
SCREWS	2-56 X 1/8 SOCKET HEAD CAP SCREW	3
	2-56 X 1/4 SOCKET HEAD CAP SCREW	6
	2-56 X 1/8 SET SCREW	6
	4-40 X 1 SOCKET HEAD CAP SCREW	2
	4-40 X 3/16 SET SCREW	1
	6-32 X 3/16 SOCKET HEAD CAP SCREW	6
RETAINING RINGS	RETAINING RING FOR 1/8 SHAFT	25
	RETAINING RING FOR 3/16 SHAFT	1
RUBBER BALLS	3/16 DIAMETER N-BUNA RUBBER BALLS	18
MISCELLANEOUS	EPOXY	1 TUBE





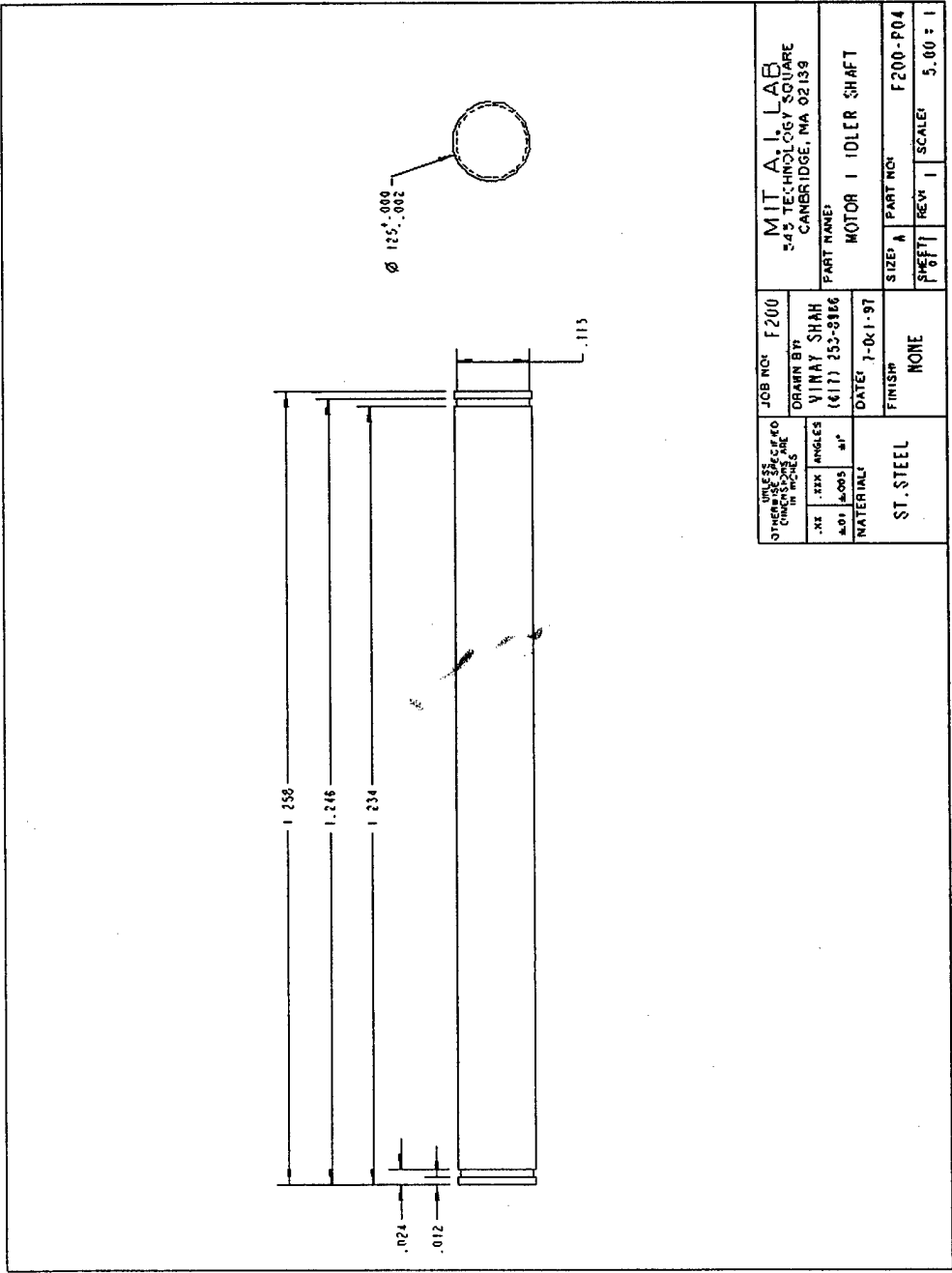
$\varnothing .157 (14.00mm)_{-0.002}^{+0.000}$   
 $\varnothing .059 (1.50mm)_{-0.000}^{+0.002}$   
 $\pm 275 \text{ MIN}$

UNLESS OTHERWISE SPECIFIED, DIMENSIONS ARE IN INCHES		JOB NO: F200		MIT A.I. LAB 245 TECHNOLOGY SQUARE CAMBRIDGE, MA 02139	
DATE	1-01-97	DRAWN BY	VINAY SHAH (617) 253-8866	PART NAME: ENCODER ADAPTER SHAFT	
DATE	1-01-97	FINISH	NONE	SIZE: A	PART NO: F200-P02
MATERIAL	ST. STEEL			SHEET 1	REV 1
				SCALE	3.00 : 1

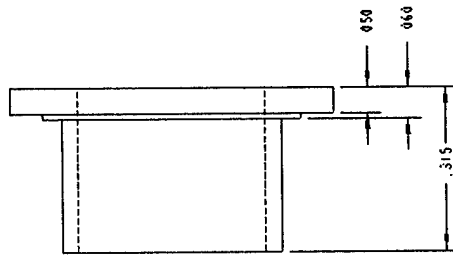
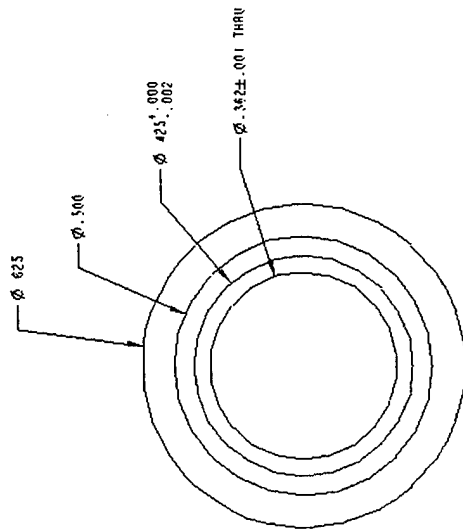


UNITS SPECIFIED OTHER THAN INCHES OR ANGLES ARE IN INCHES	JOB NO. F200		MIT A. I. LAB 545 TECHNOLOGY SQUARE CAMBRIDGE, MA 02139	
	DRAWN BY VINAY SHAH (417) 253-8986		PART NAME: MOTOR I OLIER SUPPORT	
	DATE: 7-01-97		SIZE: A PART NO: F200-P03	
FINISH: NONE		SHEET 1		SCALE: 2.00 = 1

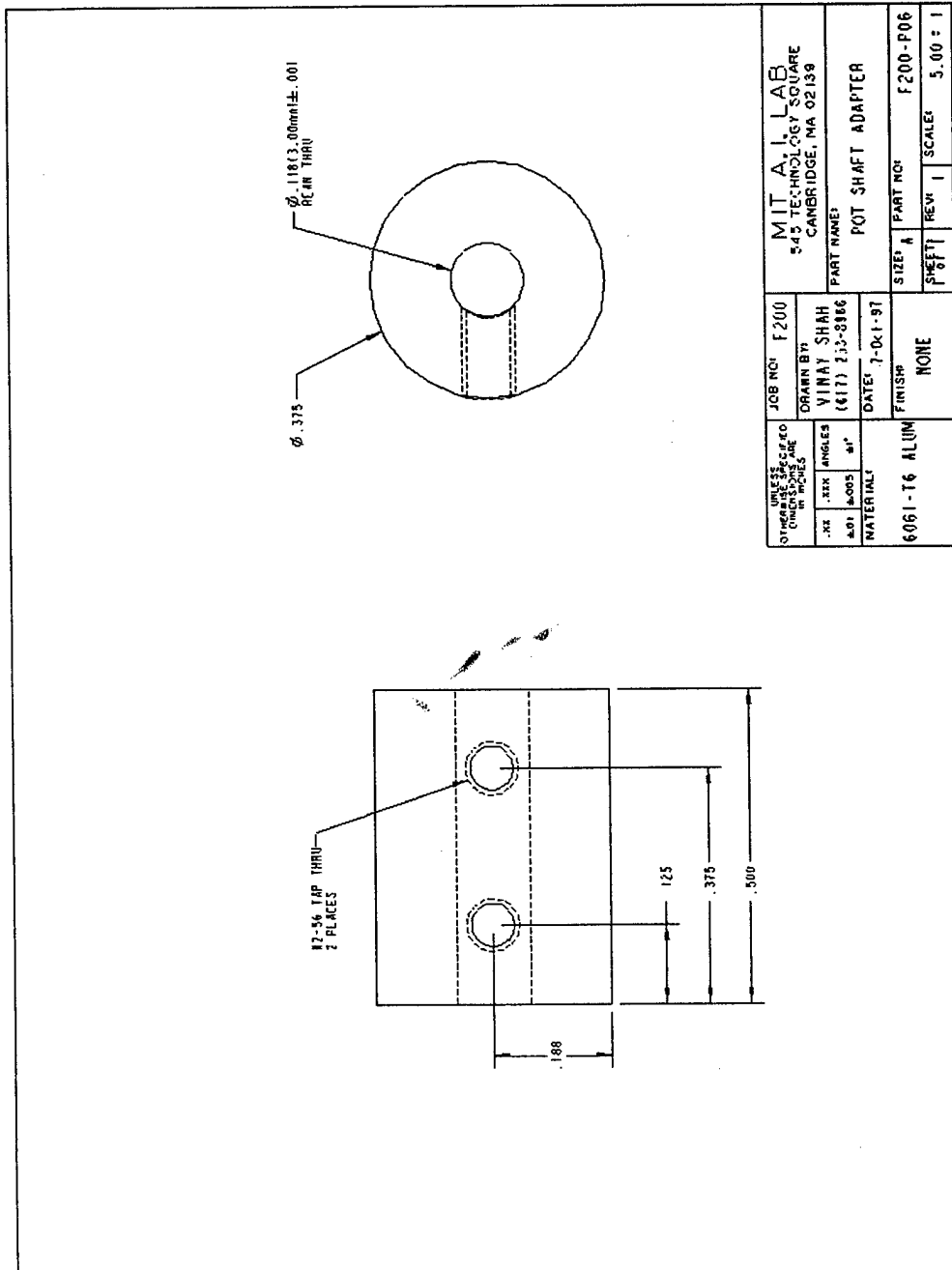




OTHER VIEWS, CROSS SECTIONS, AND DIMENSIONS ARE IN INCHES		JOB NO.	F200
DRAWN BY		VINAY SHAH	
DATE		7-01-97	
FINISH		NONE	
MATERIAL		ST. STEEL	
SIZE		F200-F04	
SHEET		5.00 ± 1	
REV		1	
SCALE		5.00 ± 1	

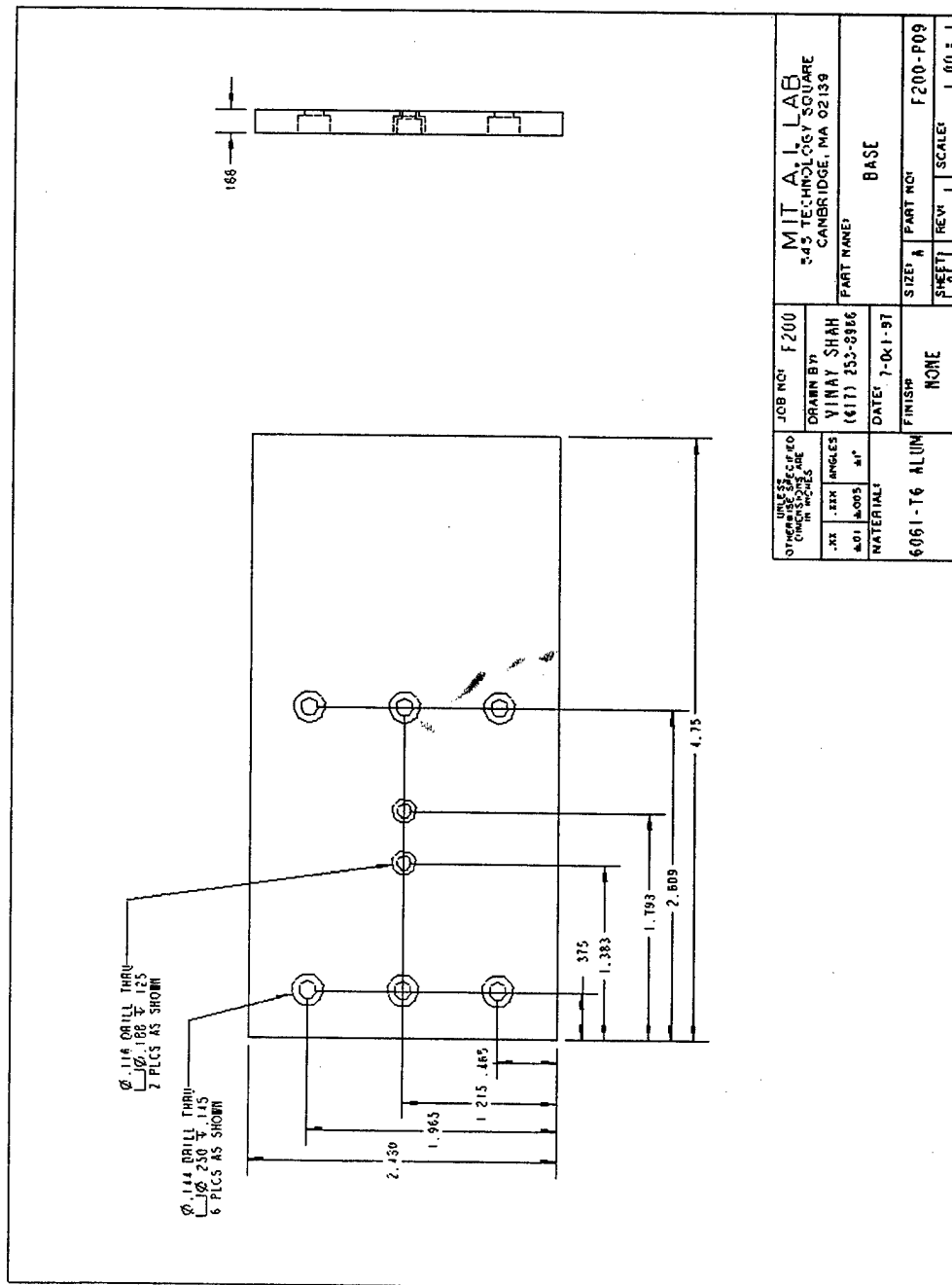


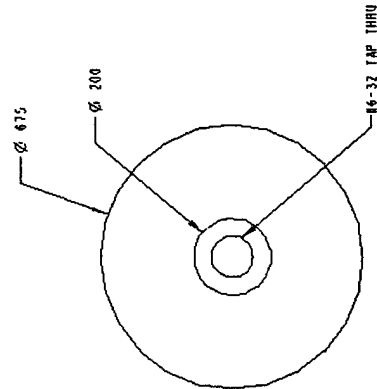
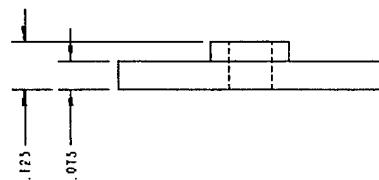
UNLESS SPECIFIED TO OTHERWIS, ALL DIMENSIONS ARE TO BE HUNDRETHS OF AN INCH	JOB NO: F200		MIT A. I. LAB 545 TECHNOLOGY SQUARE CAMBRIDGE, MA 02139	
	DRAWN BY: VINAY SHAH (617) 253-5966	PART NAME: POT FACE ADAPTER		
.XX .XX ANGLES .01 .005 .01	DATE: 7-01-97	SIZE: A	PART NO: F200-P05	
MATERIAL: 6061-T6 ALUM	FINISH: NONE	SHEET 1	REV: 1	SCALE: 4.00 : 1



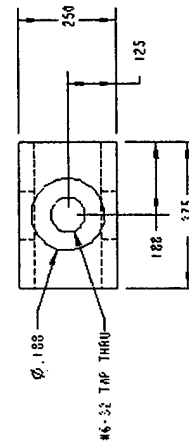
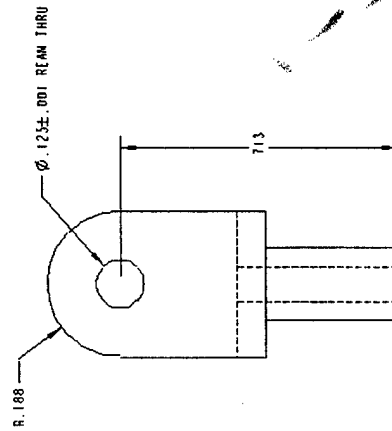
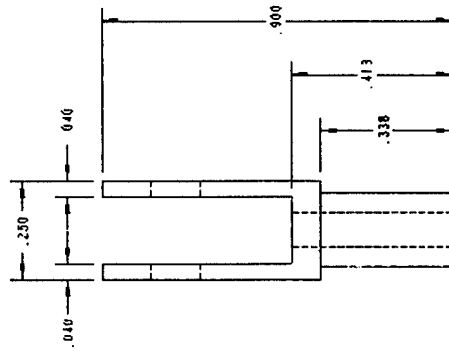






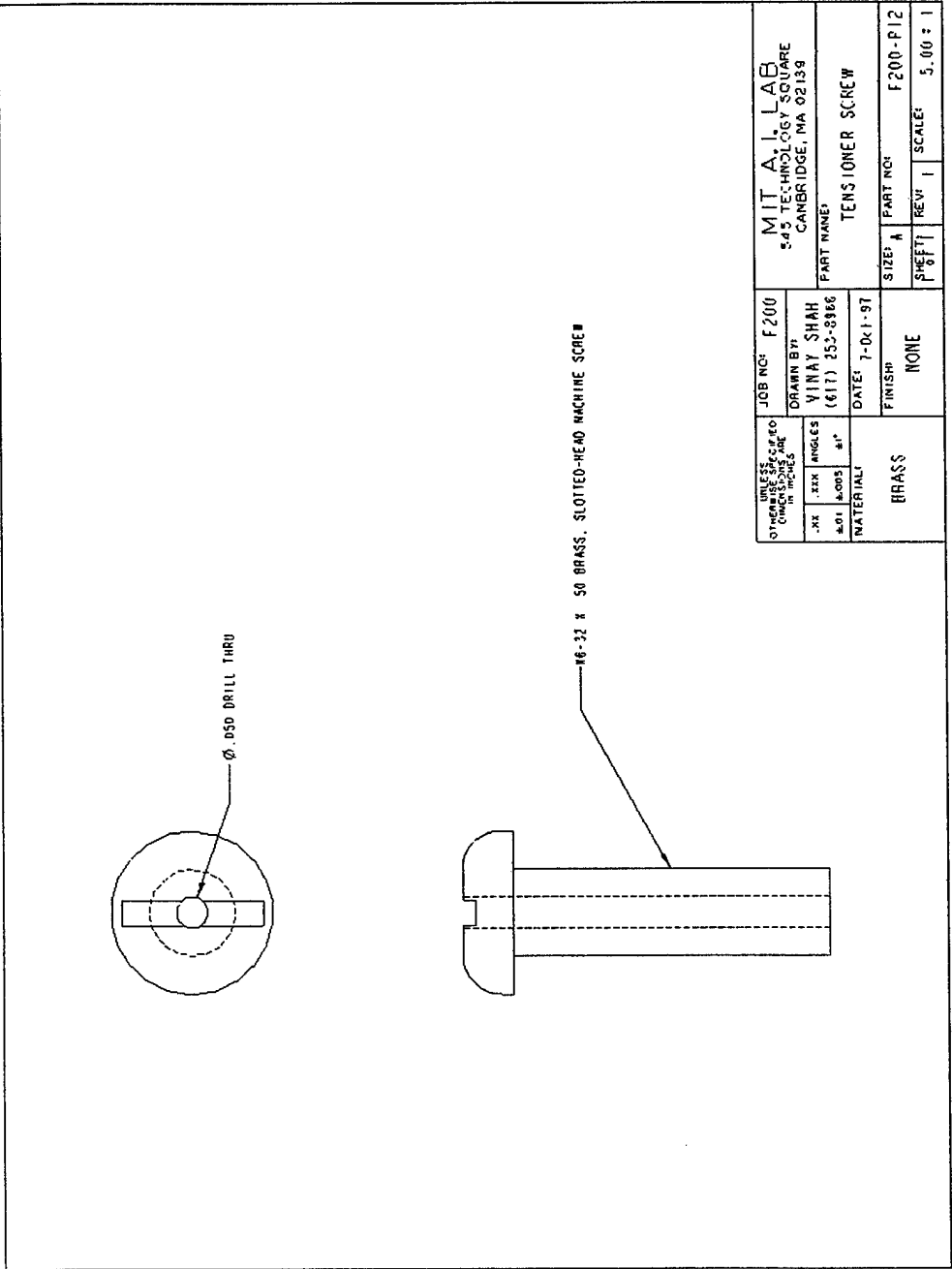


UNLESS OTHERWISE SPECIFIED, DIMENSIONS ARE IN INCHES	JOB NO: F200	MIT A.I. LAB 245 TECHNOLOGY SQUARE CAMBRIDGE, MA 02139	
	DRAWN BY: VINAY SHAH (617) 253-2986	PART NAME: TENSIONER PLATE	
.XX .XX ANGLES 4.01 ±.005 91°	DATE: 7-01-97	SIZE: A	PART NO: F200-P10
MATERIAL: 6061-T6 ALUM	FINISH: NONE	SHEET: 1	SCALE: 3.00 : 1

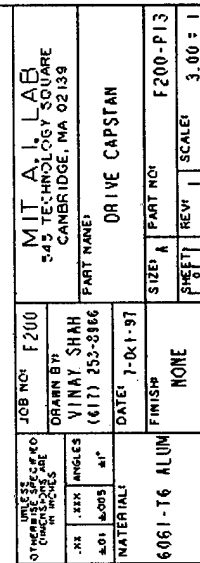


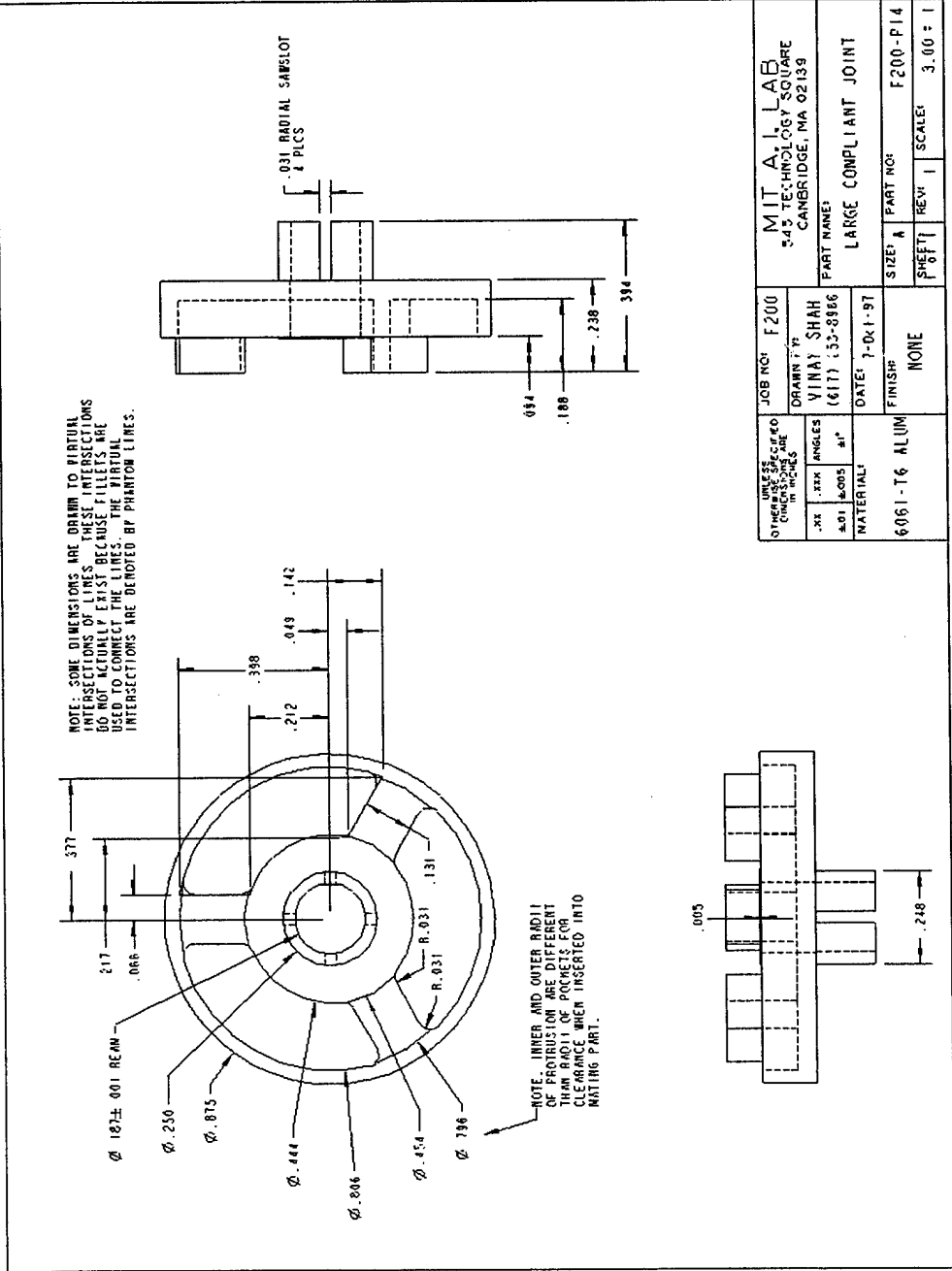
UNLESS OTHERWISE SPECIFIED, DIMENSIONS ARE IN INCHES		JOB NO.	F200	MIT A.I. LAB 545 TECHNOLOGY SQUARE CAMBRIDGE, MA 02139	
DRAWN BY	VINAY SHAH	PART NAME	TENSIONER PULLEY SUPPORT	SIZE	A
DATE	7-01-91	FINISH	NONE	SHEET	1
MATERIAL	6061-T6 ALUM	SCALE	3.00 ± .1	REV	1





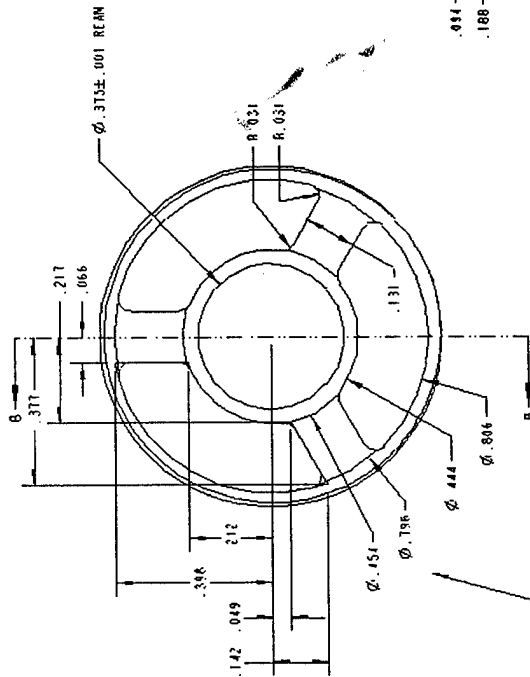
UNLESS OTHERWISE SPECIFIED, DIMENSIONS ARE IN INCHES			JOB NO: F200		MIT A.I. LAB 545 TECHNOLOGY SQUARE CAMBRIDGE, MA 02139			
.XX		ANGLES	DRAWN BY: VINAY SHAH		PART NAME:			
±.01		±.005	(617) 253-8966		TENSIONER SCREW			
MATERIAL:			DATE: 7-01-97		SIZE: A		PART NO: F200-P12	
BRASS			FINISH:		NONE		SHEET 1	
					REV: I		SCALE: 5.00 ± 1	





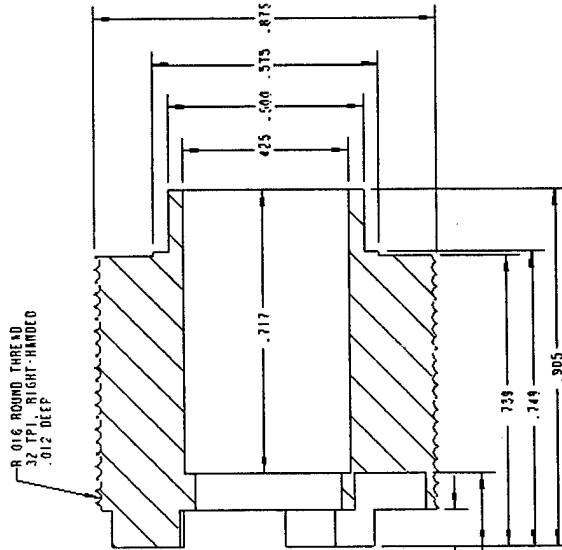
UNLESS OTHERWISE SPECIFIED, ALL DIMENSIONS ARE IN INCHES		JOB NO: F200	MIT A.I. LAB 245 TECHNOLOGY SQUARE CAMBRIDGE, MA 02139	
XX	XX	ANGLES	DRAWN BY: VINAY SHAH	PART NAME: LARGE COMPLIANT JOINT
XX	XX	ANGLES	(617) 332-8986	
XX	XX	ANGLES	DATE: 7-01-97	
MATERIAL: 6061-T6 ALUM		FINISH: NONE	SIZE: A	PART NO: F200-P14
			SHEET: 1	REV: 1
			SCALE: 3.00 = 1	

NOTE: SOME DIMENSIONS ARE DRAWN TO VIRTUAL INTERSECTIONS OF LINES. THESE INTERSECTIONS DO NOT ACTUALLY EXIST BECAUSE FILLETS ARE USED TO CONNECT THE LINES. THE VIRTUAL INTERSECTIONS ARE DENOTED BY PHANTOM LINES.



NOTE: INNER AND OUTER RADIi OF PROTRUSION ARE DIFFERENT THAN RADIi OF POCKETS FOR CLEARANCE WHEN INSERTED INTO MATING PART.

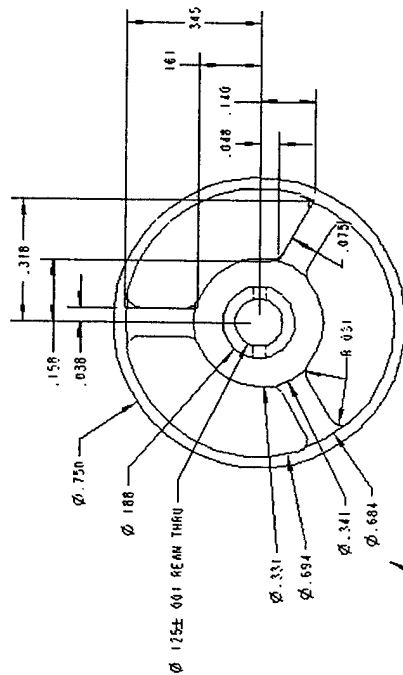
SECTION B-B



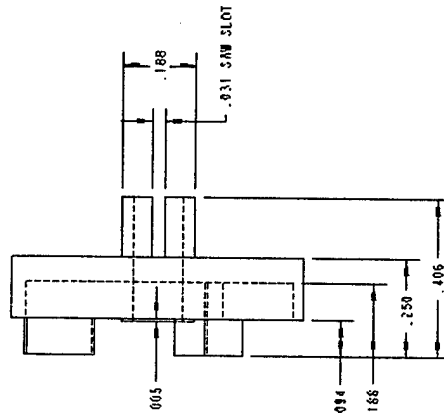
JOB NO: F200 DRAWN BY: VINAY SHAH (617) 253-8986 DATE: 1-04-97		MIT A.I. LAB 245 TECHNOLOGY SQUARE CAMBRIDGE, MA 02139	
PART NAME: LARGE COMPLIANT CAPSTAN	SIZE: A SHEET: 1	PART NO: F200-P15	REV: 1 SCALE: 3.00 : 1
FINISH: NONE	MATERIAL: 6061-T6 ALUM		

NOTE: HIDDEN LINES HAVE BEEN REMOVED FOR CLARITY

NOTE: SOME DIMENSIONS ARE DRAWN TO VIRTUAL INTERSECTIONS OF LINES. THESE INTERSECTIONS DO NOT ACTUALLY EXIST BECAUSE FILLETS ARE USED TO CORRECT THE LINES. THE VIRTUAL INTERSECTIONS ARE DENOTED BY PHANTOM LINES.

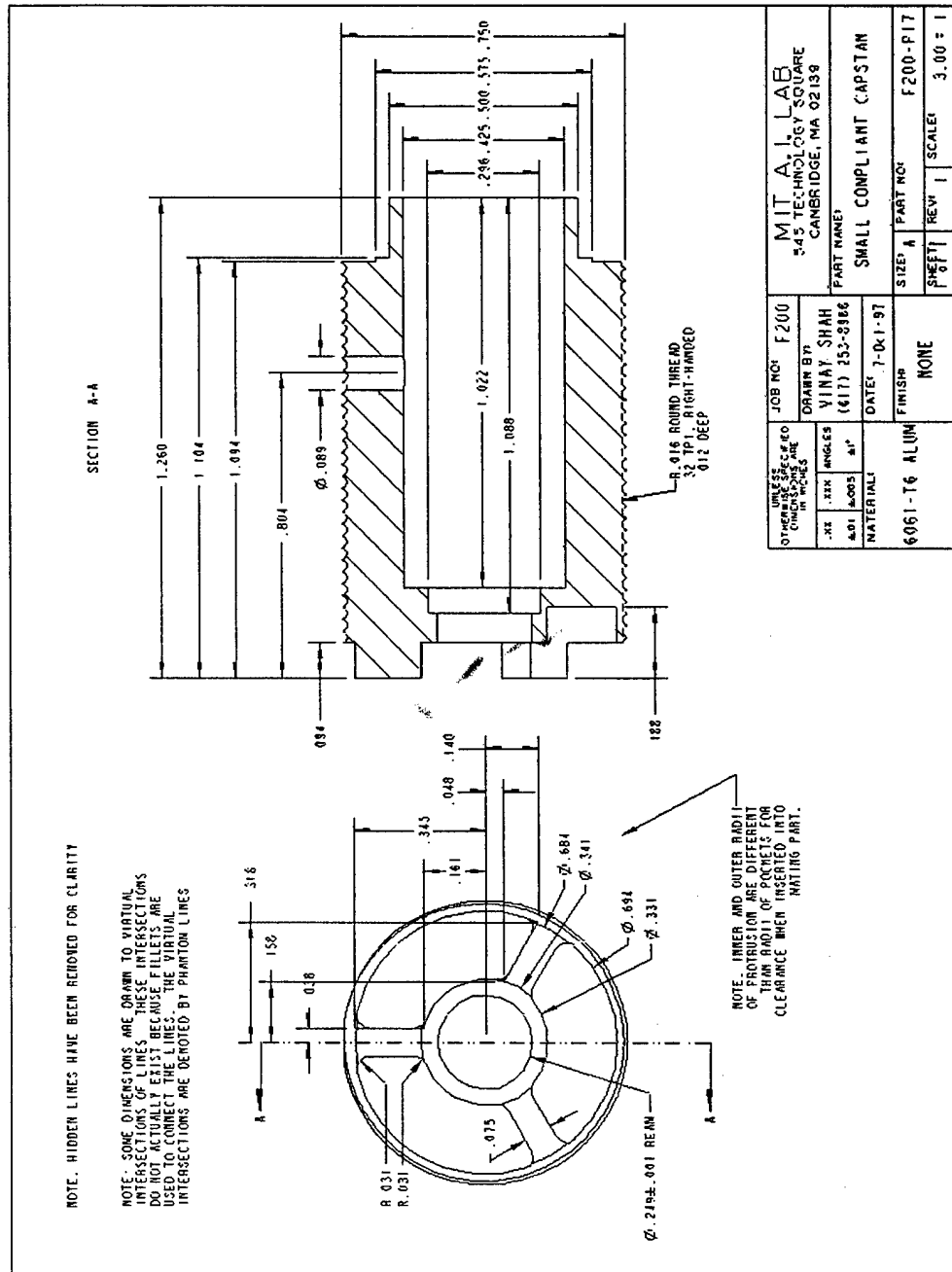


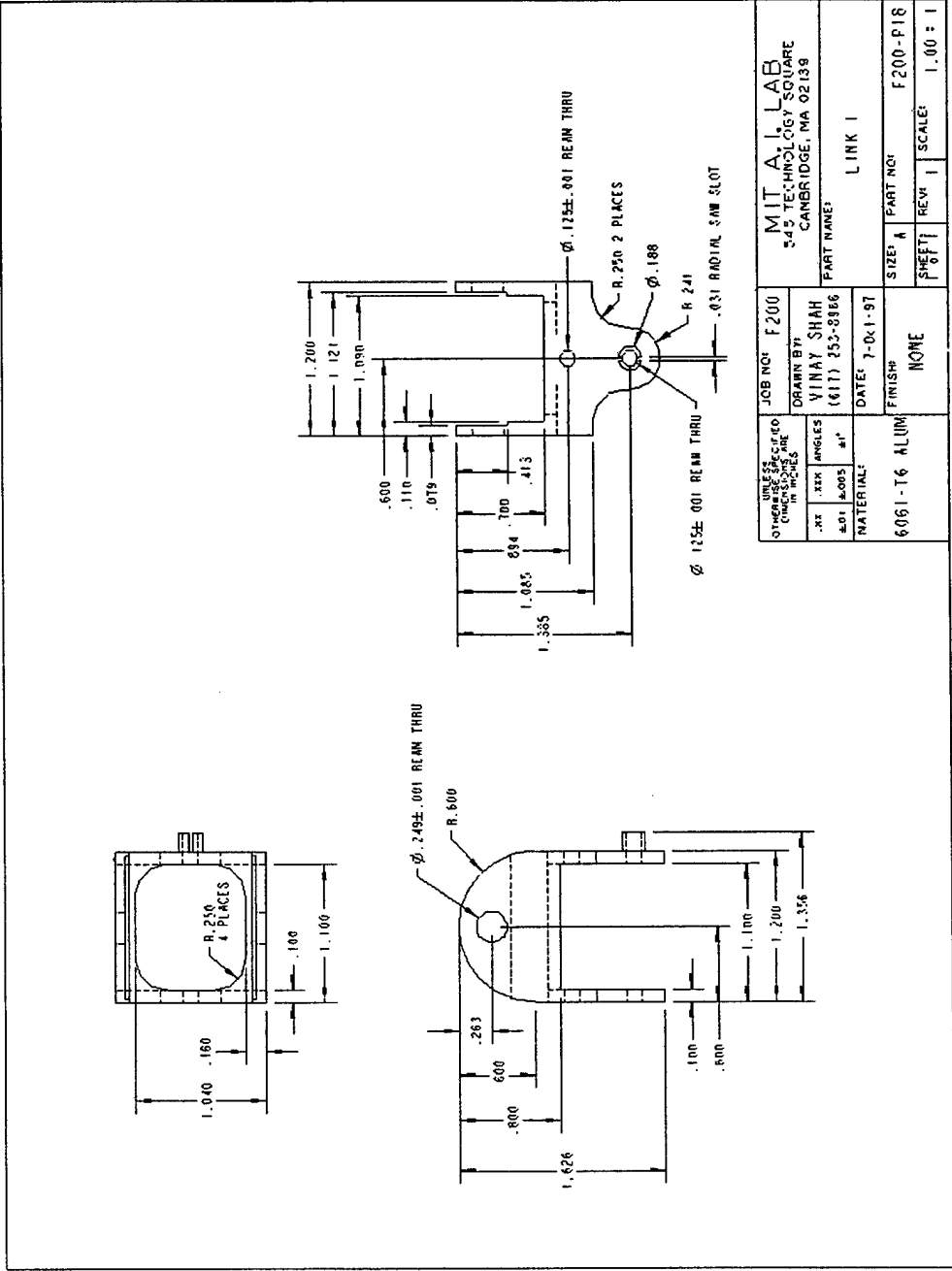
NOTE: INNER AND OUTER RADIUS OF PROTRUSION ARE DIFFERENT THAN RADIUS OF POCKETS FOR CLEARANCE WHEN INSERTED INTO MATING PART.

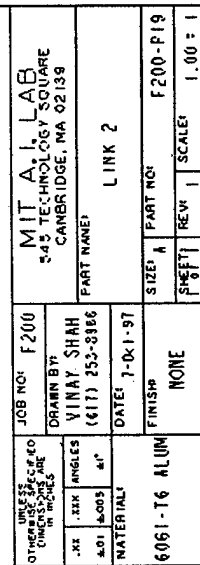


UNLESS SPECIFIED OTHERWISE DIMENSIONS ARE IN INCHES		JOB NO: F200	MIT AL LAB 545 TECHNOLOGY SQUARE CAMBRIDGE, MA 02139	
.XX	XX	ANGLES	DRAWN BY: VINAY SHAH (617) 253-8386	PART NAME: SMALL COMPLIANT JOINT
Δ.01	Δ.005	Δ"	DATE: 7-01-97	SIZE: A
MATERIAL: 6061-T6 ALUM		FINISH: NONE	PART NO: F200-P16	SCALE: 3.00 ± 1
			SHEET: 1	REV: 1

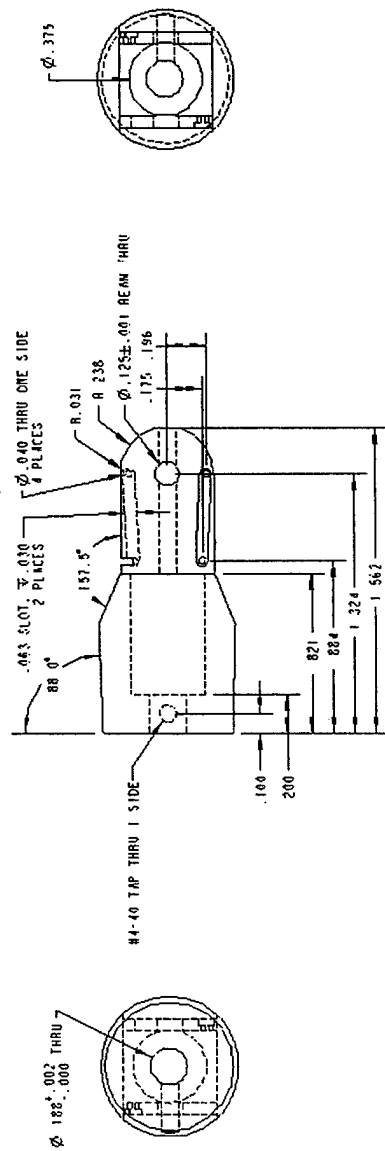
SCALE 3.000





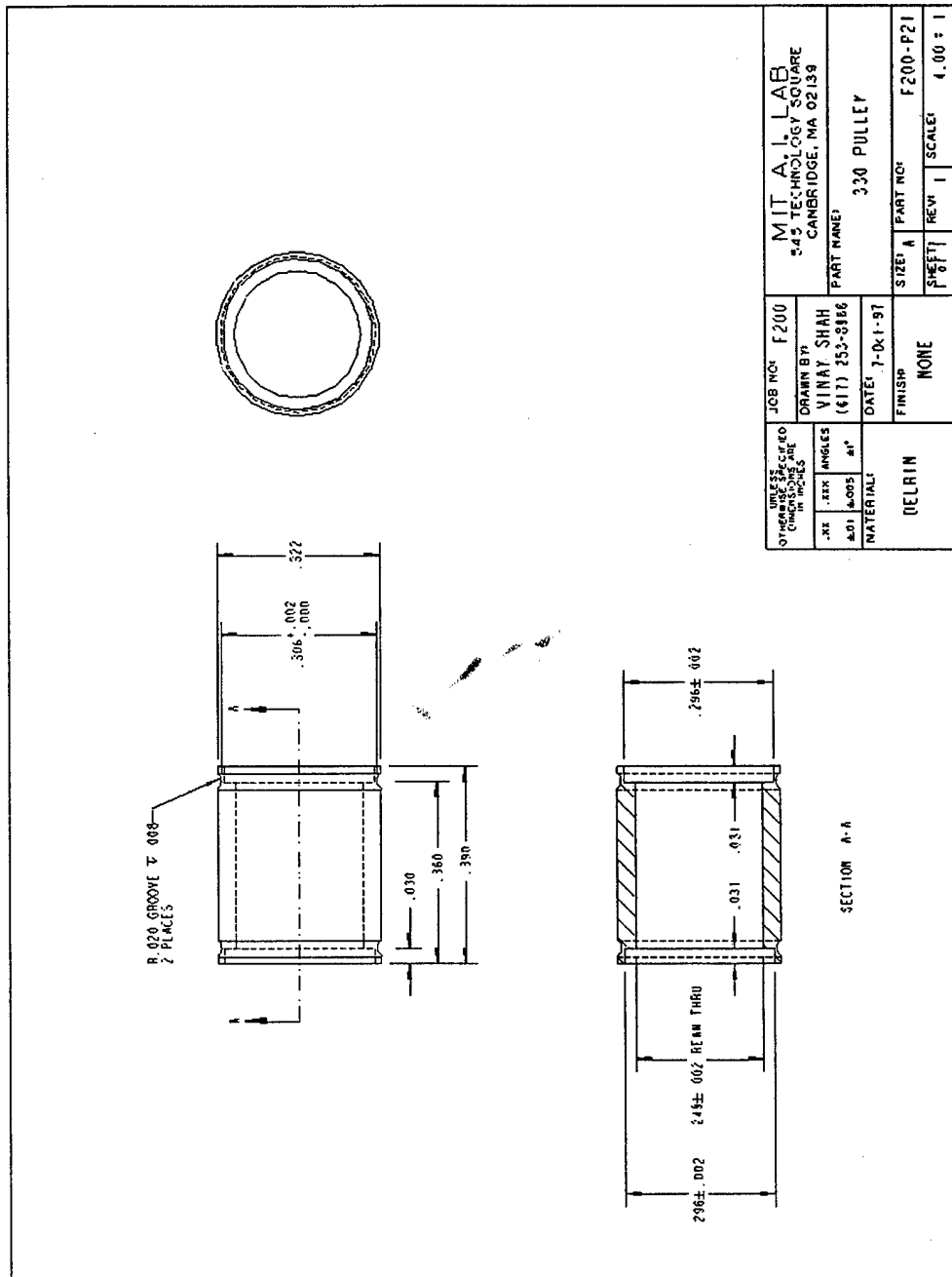


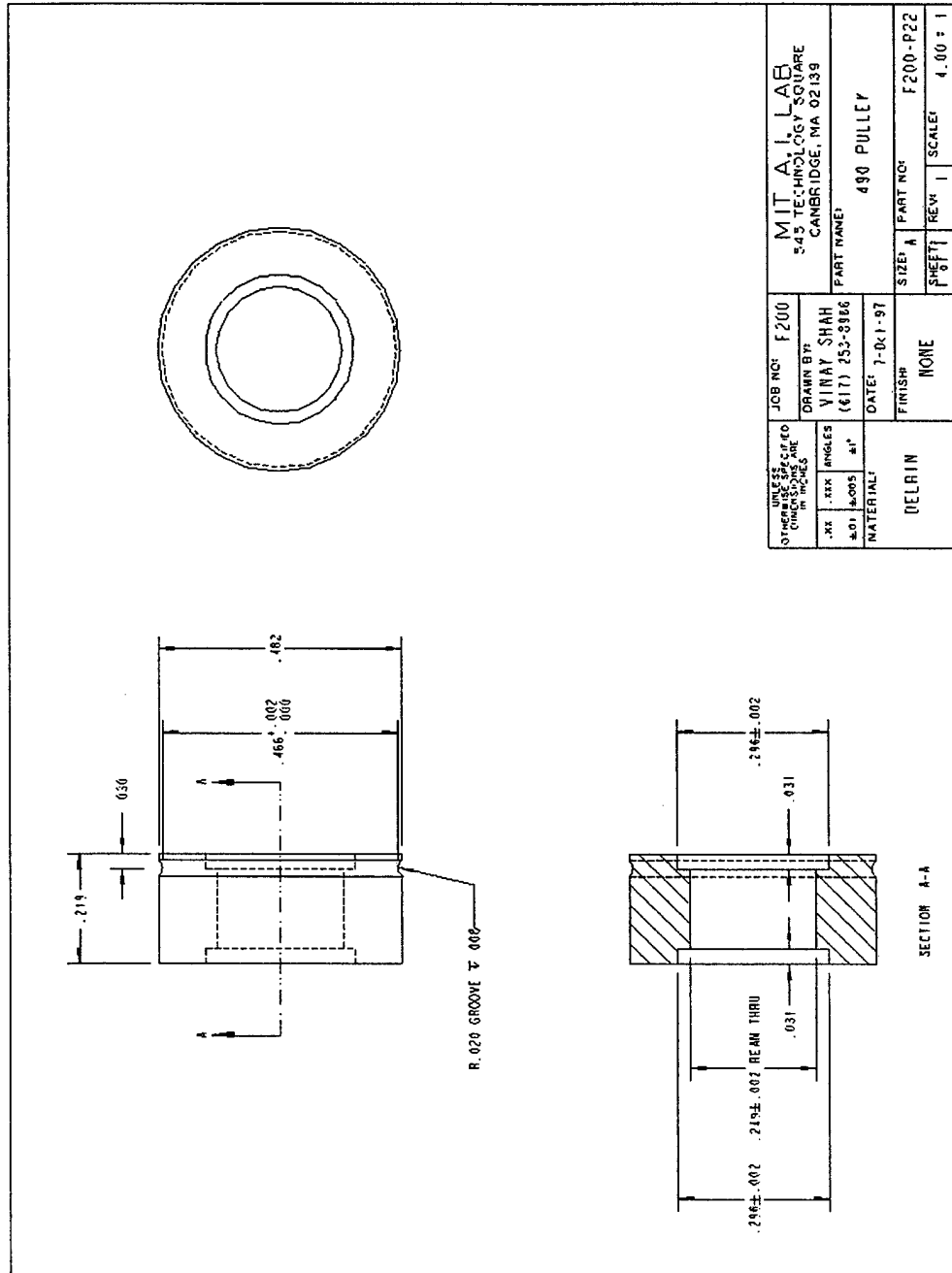




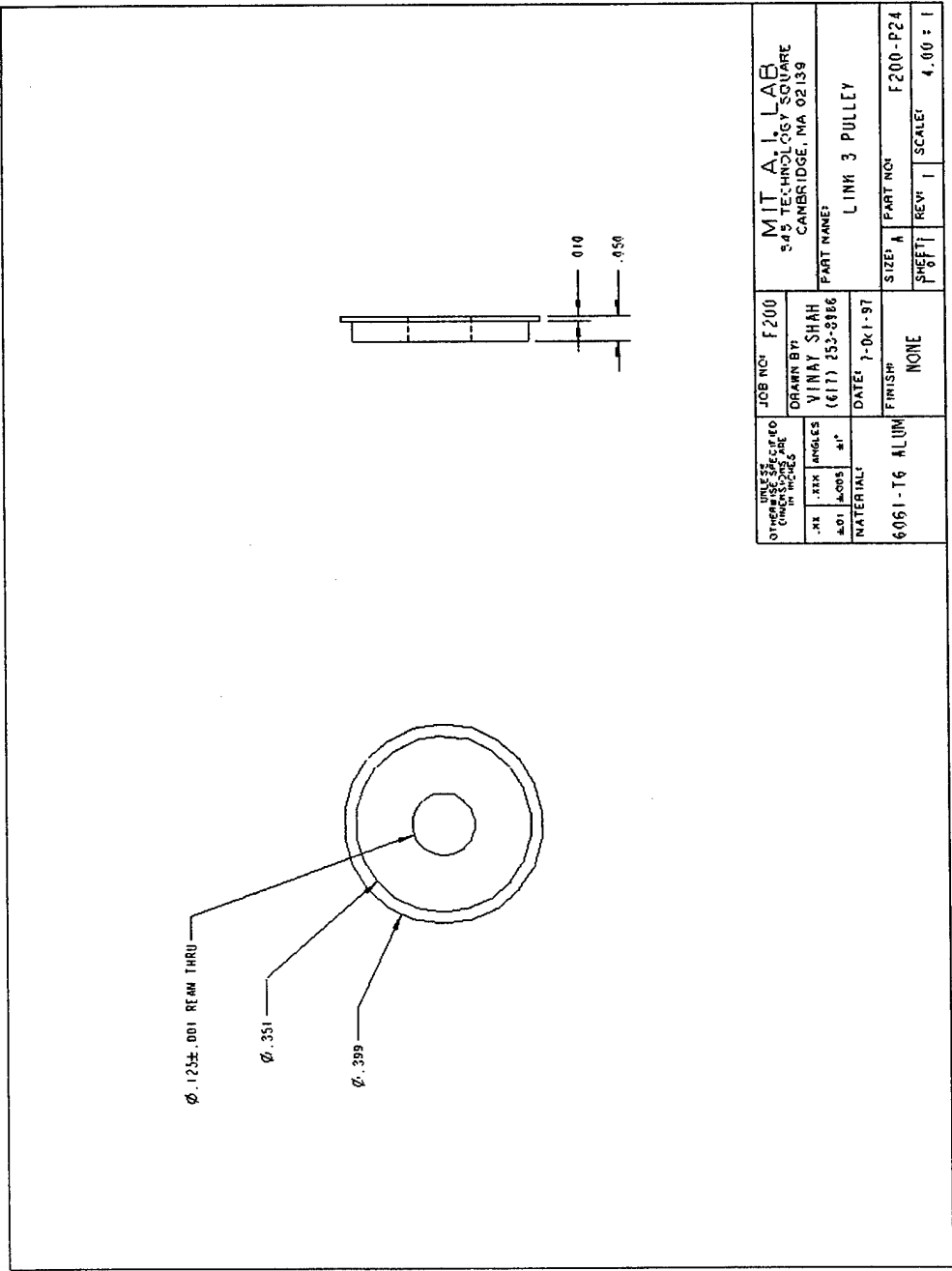
6061-T6 ALUM FINISH NONE DATE: 7-01-97 MATERIAL:	JOB NO: F200 DRAWN BY: VINAY SHAH (617) 253-8866	MIT A.I. LAB 545 TECHNOLOGY SQUARE CAMBRIDGE, MA 02139 PART NAME: LINK 3
SIZE: A SHEET 1	PART NO: REV: 1	F200-P20 SCALE: 1.50 : 1

SECRET

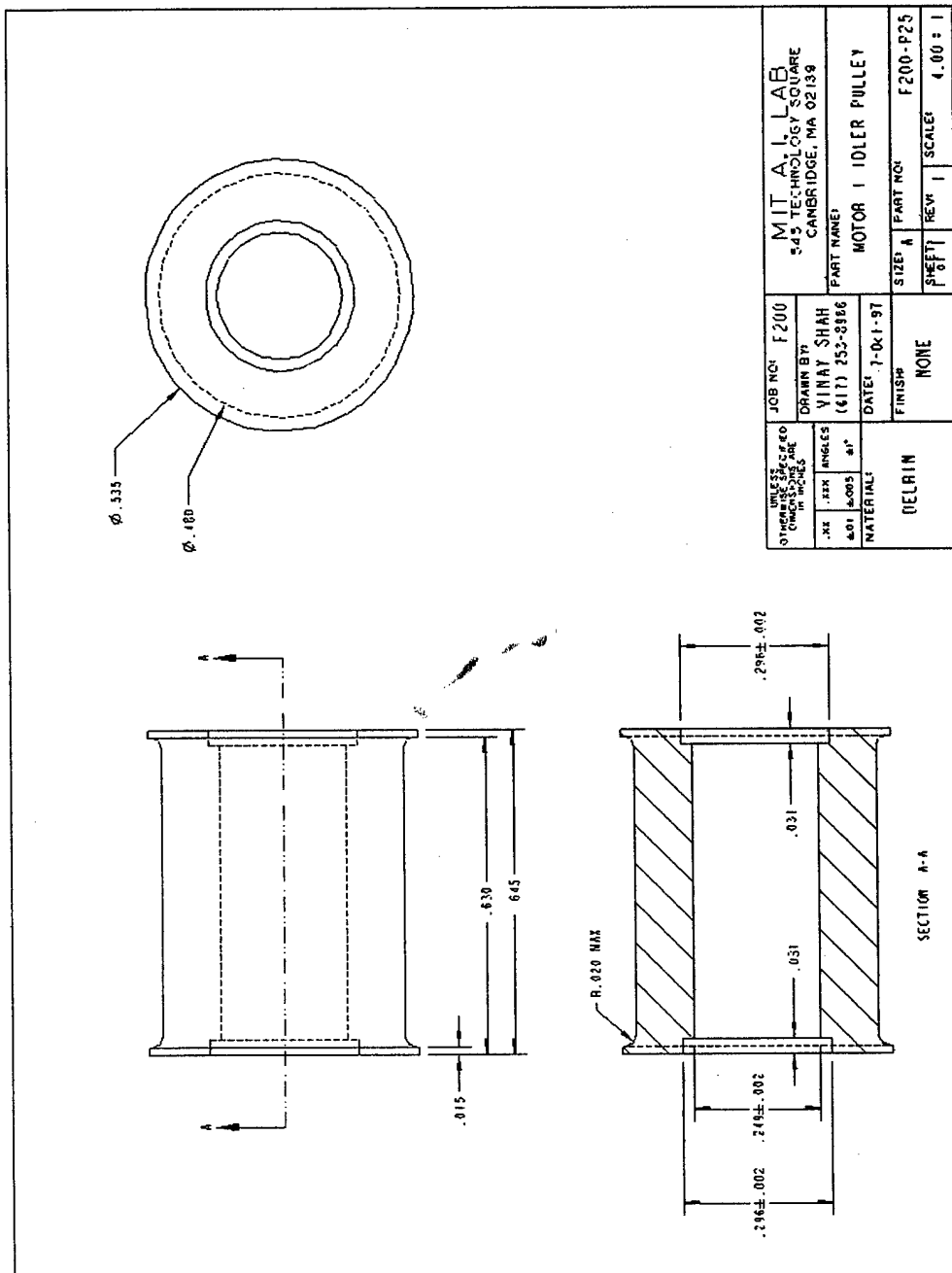


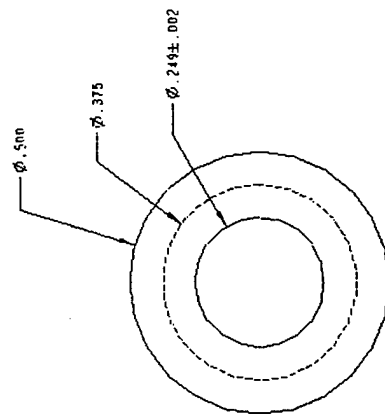
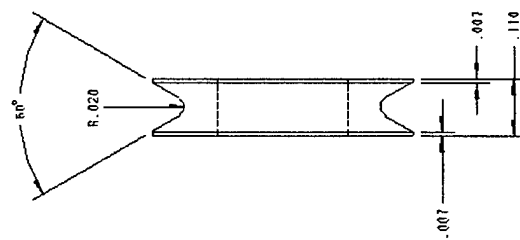




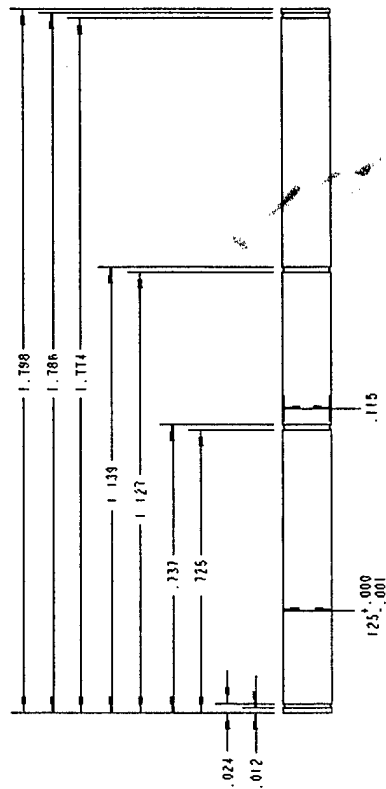


UNITS DIMENSIONS ARE IN INCHES			JOB NO.	F200	MIT A.I. LAB 345 TECHNOLOGY SQUARE CAMBRIDGE, MA 02139		
.XX	.XX	ANGLES	DRAWN BY:	VINAY SHAH	PART NAME:		
.01	.005	±"	(611) 253-8986	DATE:	LINK 3 PULLEY		
MATERIAL:			1-01-97	FINISH:	SIZE: A	PART NO:	F200-P24
6061-T6 ALUM			NONE		SHEET	REV: 1	SCALE: 4.00 = 1



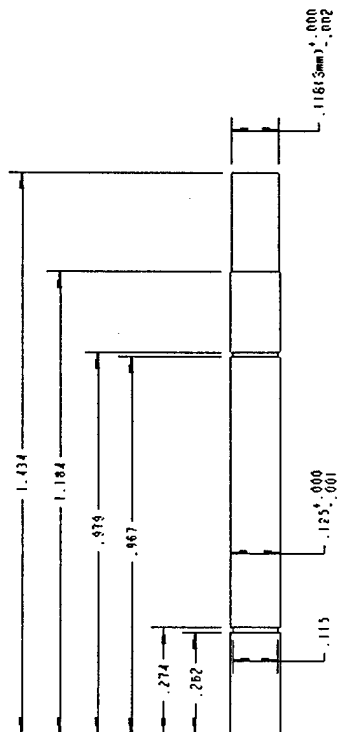


UNLESS SPECIFIED DIMENSIONS ARE IN INCHES		JOB NO: F200	MIT A. L. LAB 545 TECHNOLOGY SQUARE CAMBRIDGE, MA 02139	
XX	ANGLES	DRAWN BY: VINAY SHAH (617) 253-8986	PART NAME: TENSIONER PULLEY	
XX	±"	DATE: 7-01-97	SIZE: A	PART NO: F200-P26
MATERIAL: UELRIN		FINISH: NONE	SHEET: 1	SCALE: 4.00 = 1

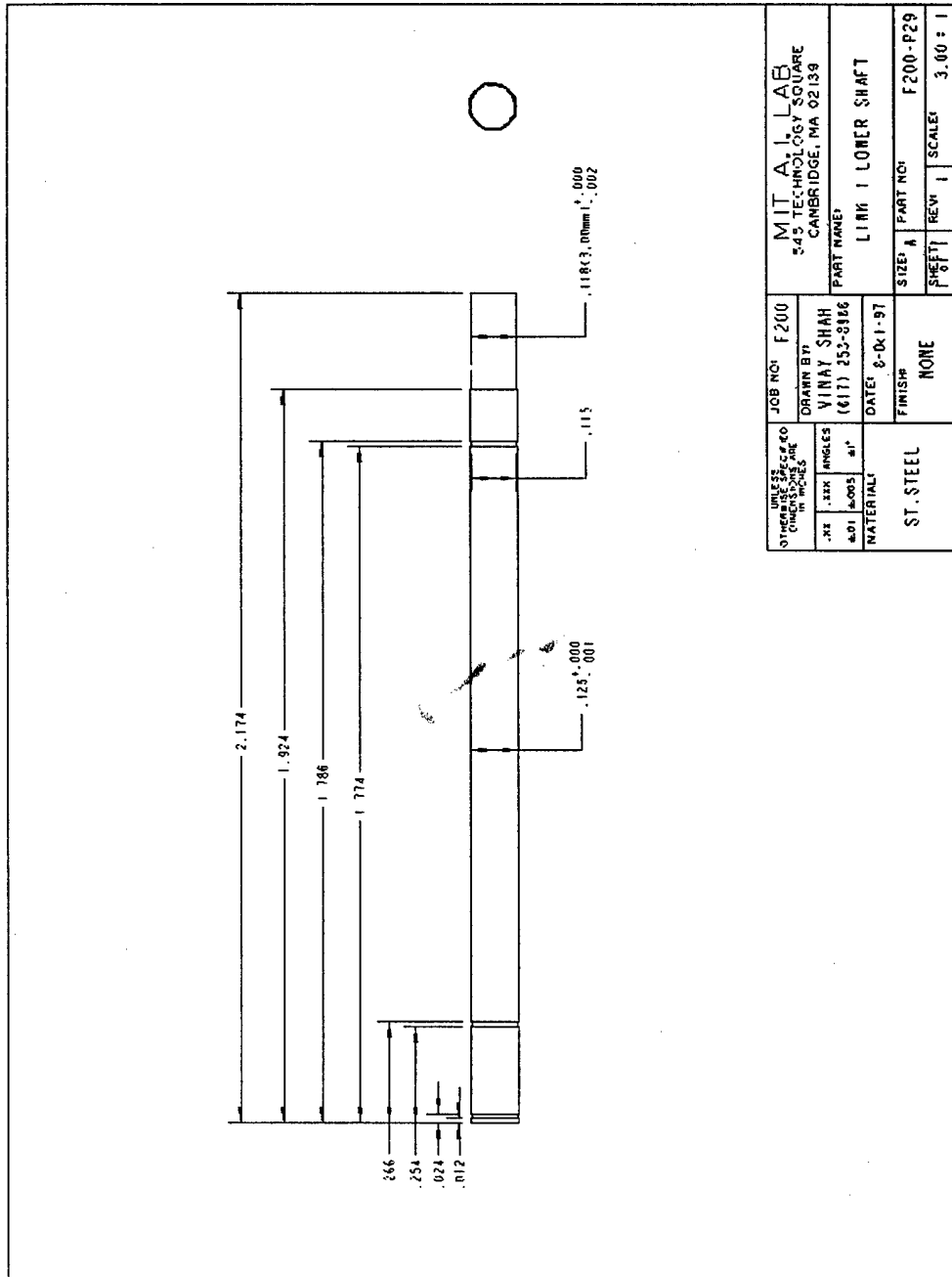


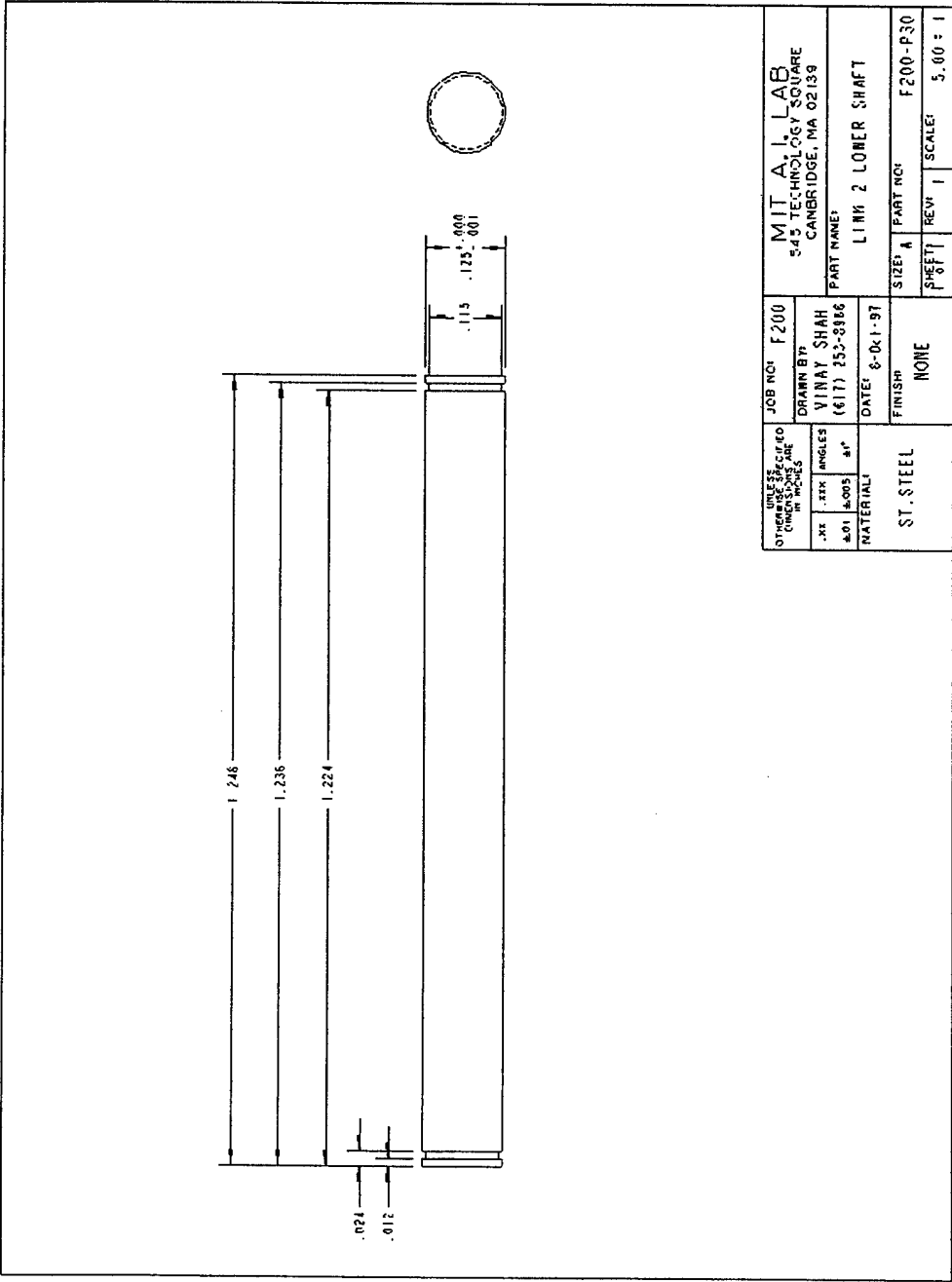
UNLESS OTHERWISE SPECIFIED, DIMENSIONS ARE IN INCHES		JOB NO: F200		MIT A.I. LAB 345 TECHNOLOGY SQUARE CAMBRIDGE, MA 02139	
DRAWN BY: VINAY SHAH (617) 253-3986		DATE: 7-01-97		PART NAME: BASE IDLER SHAFT	
MATERIAL: ST. STEEL		FINISH: NONE		SIZE: A PART NO: F200-P27	
.X1 .2X1 ANGLES 4X1 4X.005 4X1		125.000		SHEET 1	
.024 .012		.115		REV: 1 SCALE: 3.00 = 1	

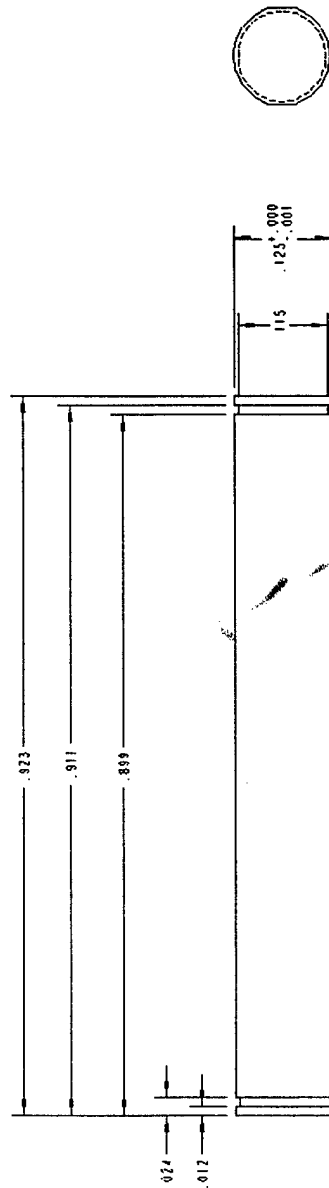




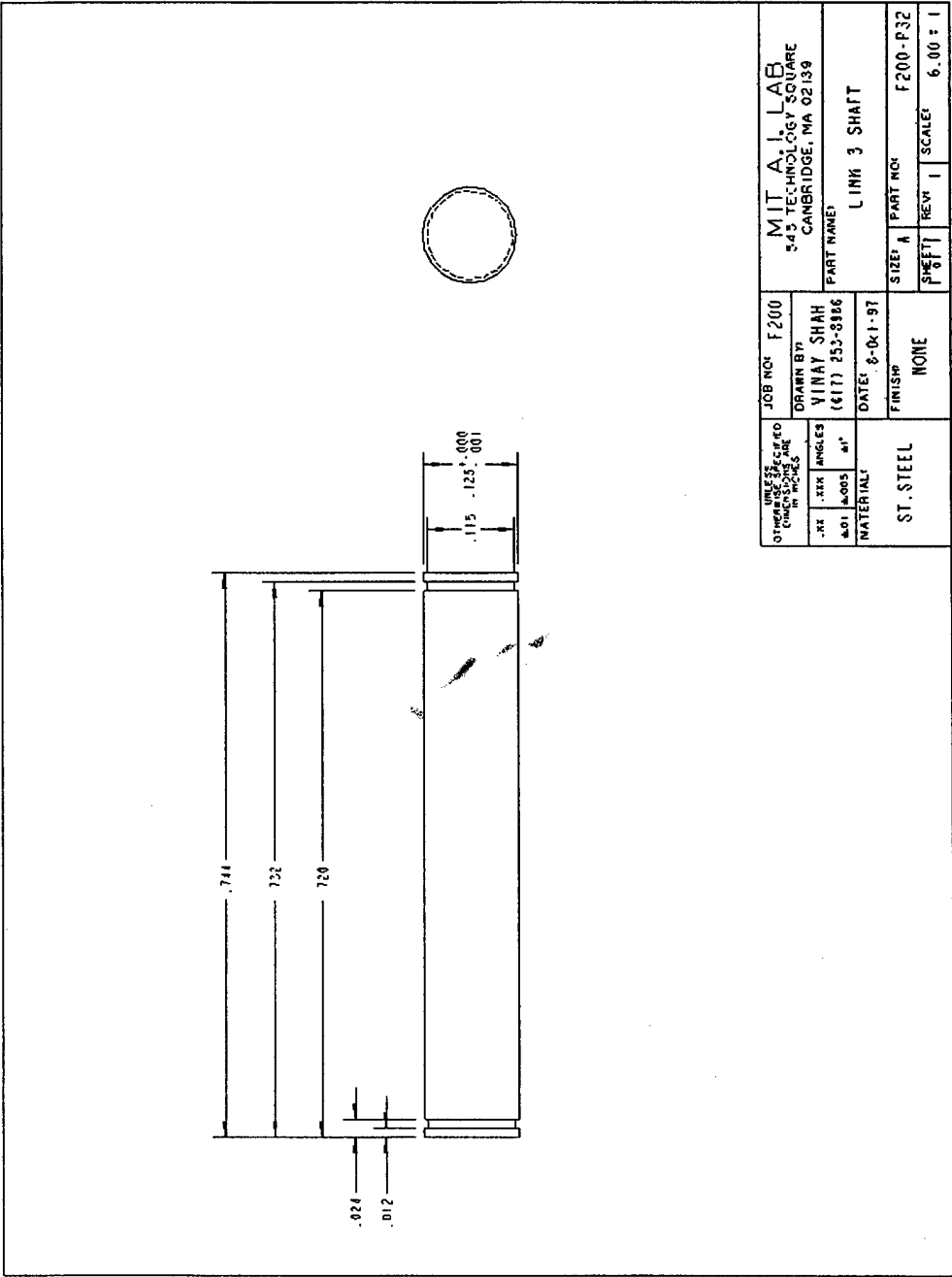
UNLESS OTHERWISE SPECIFIED DIMENSIONS ARE IN INCHES		JOB NO: F200	MIT ALLIANCE 543 TECHNOLOGY SQUARE CAMBRIDGE, MA 02139	
.XX ±.01		ANGLES ±1°	DRAWN BY: VINAY SHAH (617) 253-8986	PART NAME: BOTTOM DRIVE SHAFT
MATERIAL: ST. STEEL		DATE: 8-01-97	SIZE: A	PART NO: F200-P28
		FINISH: NONE	SHEET 1	SCALE: 3.00 = 1

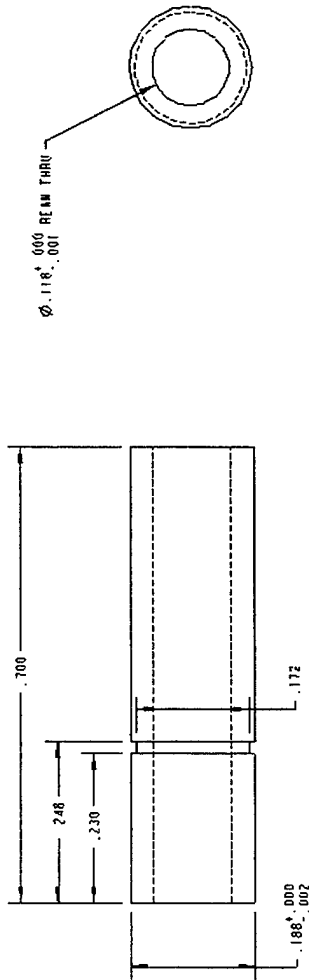




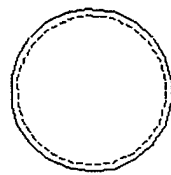
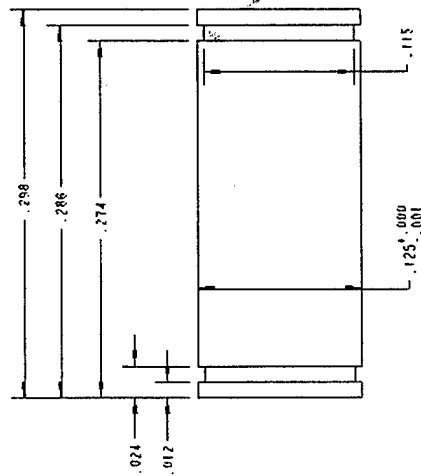


UNLESS OTHERWISE SPECIFIED, DIMENSIONS ARE IN INCHES		JOB NO.	F200	MIT A.I. LAB 345 TECHNOLOGY SQUARE CAMBRIDGE, MA 02139	
.XK .12X ANGLES A.01 A.005 4"		DRAWN BY	VINAY SHAH (617) 353-8386	PART NAME	
NATERIAL		DATE	8-01-97	LINK 2 UPPER SHAFT	
ST. STEEL		FINISH	NONE	SIZE	A
				PART NO.	F200-P31
				SHEET	1
				SCALE	6.00 : 1

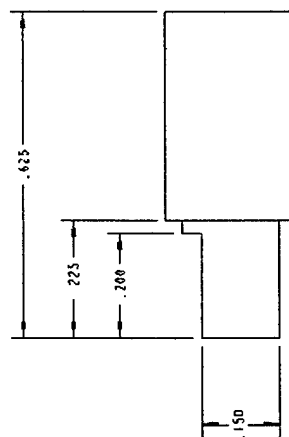
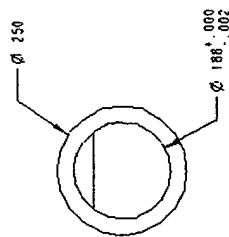




UNLESS OTHERWISE SPECIFIED, DIMENSIONS ARE IN INCHES		JOB NO: F200	MIT A.I. LAB 245 TECHNOLOGY SQUARE CAMBRIDGE, MA 02139	
DRAWN BY: VINAY SHAH (617) 253-8386		PART NAME: TOP MOTOR SHAFT		
DATE: 8-01-97		SIZE: A	PART NO: F200-P33	
FINISH: NONE		SHEET: 1	REV: 1	SCALE: 5.00 = 1
MATERIAL: ST. STEEL				

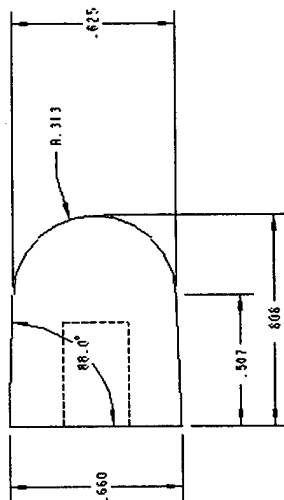
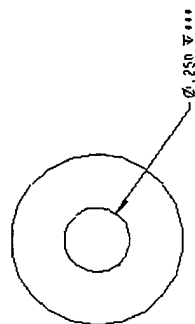


UNLESS OTHERWISE SPECIFIED, DIMENSIONS ARE IN INCHES		JOB NO: F200		MIT A.I. LAB 245 TECHNOLOGY SQUARE CAMBRIDGE, MA 02139	
DRAWN BY: VINAY SHAH (417) 253-8986		DATE: 8-01-97		PART NAME: TENSIONER SHAFT	
MATERIAL: ST. STEEL		FINISH: NONE		SIZE: A F200-P34	
.XX ANGLES 4:01 4:00S 41°		SHEET 1		REV: 1 SCALE: 10.00 : 1	

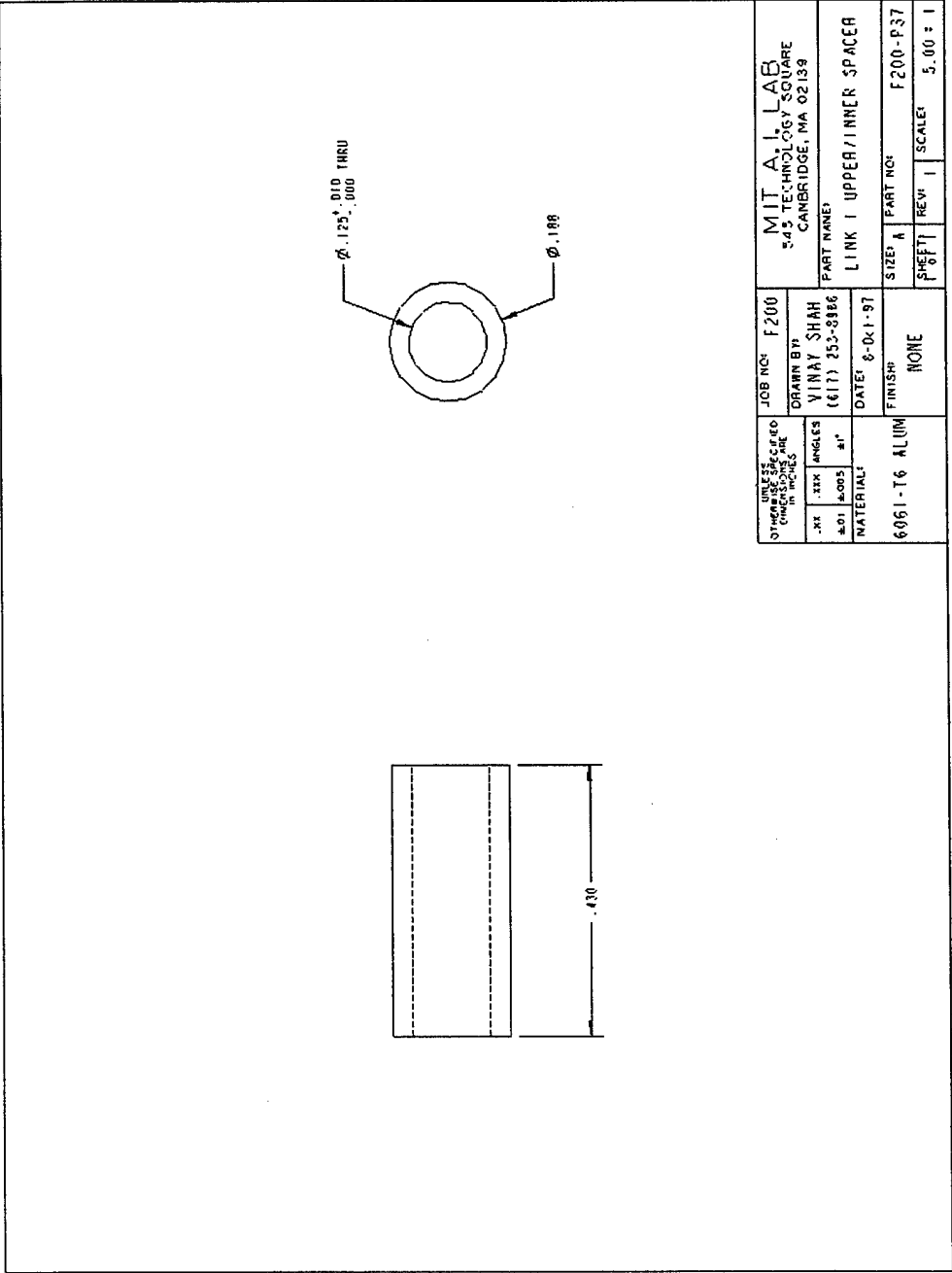


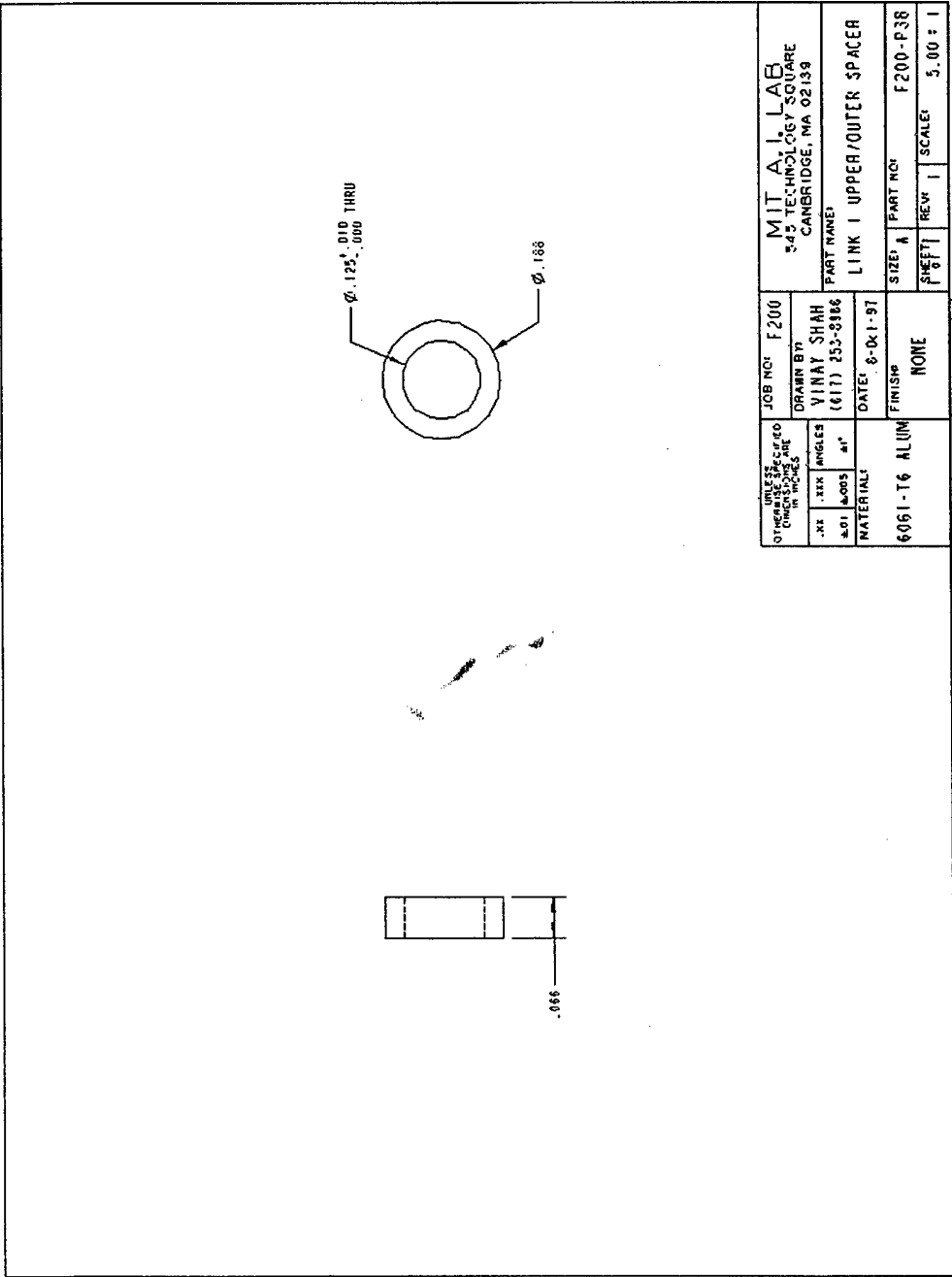
UNLESS OTHERWISE SPECIFIED, DIMENSIONS ARE IN INCHES		JOB NO: F200	MIT A.I. LAB 245 TECHNOLOGY SQUARE CAMBRIDGE, MA 02139	
.XX	.XX	DRAWN BY: VINAY SHAH	PART NAME: FINGERTIP SHAFT	
.01	.005	(617) 353-0886	SIZE: A	
MATERIAL: ST. STEEL		DATE: 8-01-97	SHEET: 1	
FINISH: NONE		PART NO: F200-P35		
		SCALE: 4.00 : 1		

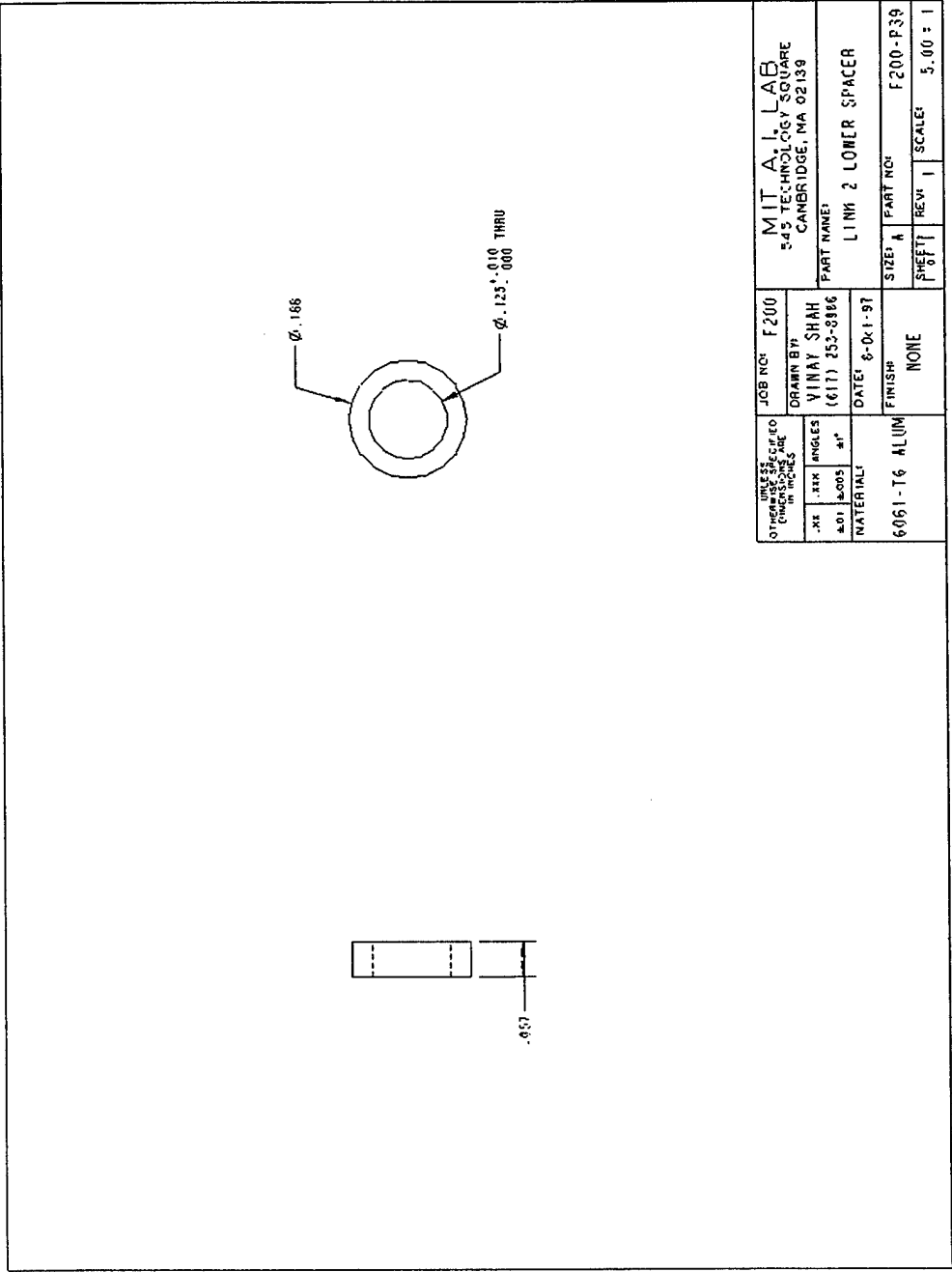




ALL DIMENSIONS UNLESS SPECIFIED IN INCHES		JOB NO: F200	MIT A.I. LAB 345 TECHNOLOGY SQUARE CAMBRIDGE, MA 02139	
DRAWN BY: VINAY SHAH (617) 253-8986		PART NAME: FINGERTIP		
DATE: 8-01-97		SIZE: A	PART NO: F200-P36	
MATERIAL: 40 DURO POLYURETHANE		FINISH: NONE	SHEET: 1	SCALE: 2.00 = 1

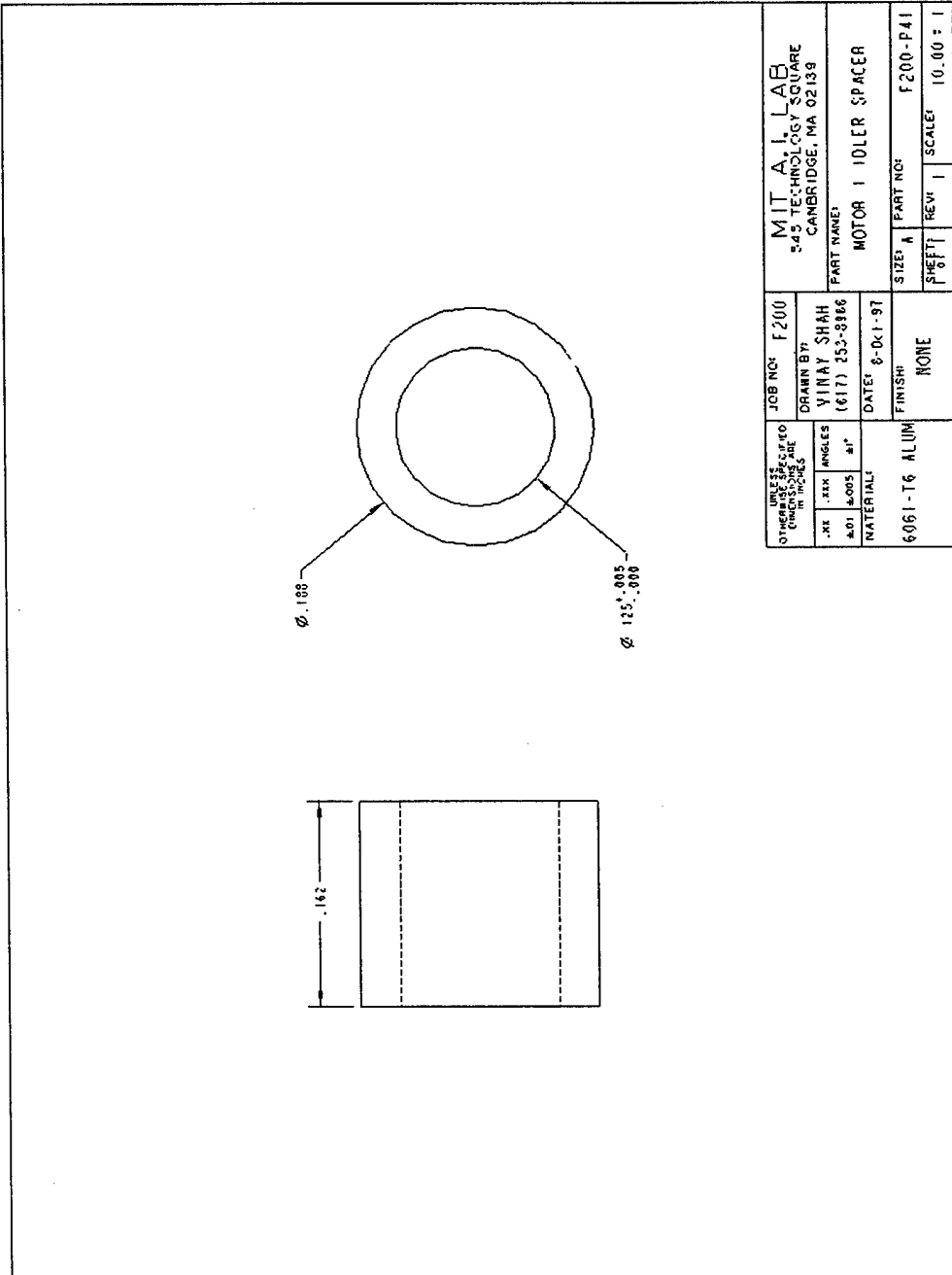






OTHER UNLESS OTHERWISE SPECIFIED, DIMENSIONS ARE IN INCHES	JOB NO: F200		MIT A.I. LAB 545 TECHNOLOGY SQUARE CAMBRIDGE, MA 02139	
	DRN BY: VINAY SHAH (617) 253-3886	PART NAME: LINK 2 LOWER SPACER		
.XX .XIX ANGLES ±.01 ±.005 ±°	DATE: 8-04-97	SIZE: A	PART NO: F200-P39	
MATERIAL: 6061-T6 ALUM	FINISH: NONE	SHEET: 1	REV: 1	SCALE: 5.00 : 1





UNLESS OTHERWISE SPECIFIED, DIMENSIONS ARE IN INCHES		JOB NO: F200	MIT A.I. LAB 245 TECHNOLOGY SQUARE CAMBRIDGE, MA 02139	
DRAWN BY: VINAY SHAH (617) 253-8986		PART NAME: MOTOR 1 IDLER SPACER		
MATERIAL: 6061-T6 ALUM		DATE: 8-01-97	SIZE: A	PART NO: F200-P41
		FINISH: NONE	SHEET: 1	SCALE: 10.00 = 1
			REV: 1	